

**NASA
Technical
Paper
3188**

April 1992

**Static Performance of a
Cruciform Nozzle With
Multiaxis Thrust-Vectoring
and Reverse-Thrust
Capabilities**

David J. Wing
and Scott C. Asbury

(NASA-TP-3188) STATIC PERFORMANCE OF A
CRUCIFORM NOZZLE WITH MULTIAxis
THRUST-VECTORING AND REVERSE-THRUST
CAPABILITIES (NASA) 62 p

CSCL 01A

41/02

N72-23095

Unclass
008478+



**NASA
Technical
Paper
3188**

1992

**Static Performance of a
Cruciform Nozzle With
Multiaxis Thrust-Vectoring
and Reverse-Thrust
Capabilities**

David J. Wing
and Scott C. Asbury
*Langley Research Center
Hampton, Virginia*



National Aeronautics and
Space Administration
Office of Management
Scientific and Technical
Information Program

Summary

A multiaxis thrust-vectoring nozzle designed to have equal flow-turning capability in pitch and yaw was conceived and experimentally tested for internal static performance at Langley Research Center. The cruciform-shaped, convergent-divergent nozzle turned the flow for thrust vectoring by deflecting the divergent surfaces of the nozzle, called flaps. Methods for eliminating physical interference between pitch and yaw flaps at the larger multiaxis deflection angles were studied. These methods included restricting the pitch flaps from the path of the yaw flaps and shifting the flow path at the throat off the nozzle centerline to permit larger pitch-flap deflections without interfering with the operation of the yaw flaps. Two flap widths were tested at both dry and afterburning power settings. Vertical- and reverse-thrust configurations at dry power were also tested.

Despite the complex internal geometry, this cruciform nozzle had only slightly lower unvectored thrust efficiency than existing axisymmetric and nonaxisymmetric nozzle designs. Thrust losses in single-axis thrust vectoring were primarily the result of complex flow interactions between shearing flows within the nozzle. Splitting the flow, a consequence of the cruciform cross section, caused these interactions. Thrust losses in multiaxis thrust vectoring were primarily the result of turning supersonic flow. More equal pitch and yaw thrust-vector angles were achieved by the nozzle with narrow divergent flaps than by the nozzle with wide divergent flaps. However, the narrow-flap nozzle had thrust losses 1 to 2 percent higher than those of the wide-flap nozzle. The shifted-throat nozzle design had larger thrust-vector angles at the nozzle pressure ratio of peak resultant thrust efficiency than the restricted-flap nozzle design but had 1.5- to 2.0-percent-lower peak thrust performance. The vertical- and reverse-thrust configurations had performance similar to that of existing nozzles of similar design.

Introduction

Military aviation history has shown that fighter aircraft with better maneuver performance have an advantage over their opponents in close-in air-to-air engagements. Maximizing this maneuverability includes maintaining attitude control into and beyond the angle-of-attack range of aerodynamic control surface effectiveness. The elevators and rudders of conventionally configured aircraft (control surfaces aft of the wing) lose effectiveness at high angles of attack, generally before the wing stalls; this effect occurs because the elevators and rudders are located in

the separated wake of the wing. Although the wing may still be producing sufficient lift, asymmetrical flow situations and ineffective aerodynamic control surfaces cause the aircraft attitude to diverge.

A supplemental source of attitude control can be achieved through deflection of the engine thrust to produce the necessary forces and moments to maintain or augment aircraft control. The primary advantage of this technique, known as thrust vectoring, is that it is independent of angle of attack, within the limits of inlet capability. When the thrust is deflected in the vertical or horizontal planes, the normal- and side-force components produce the necessary pitch and yaw moments that are usually supplied by the tail surfaces.

The concept of deflecting the engine thrust to produce useful forces may be extended to include deflecting the thrust vertically downward to supplement or replace the wing lift for such applications as short and vertical takeoffs and landings. This extension of the concept assumes proper balance can be maintained through reaction control jets. In addition, deflecting the thrust forward produces reverse thrust that can be used in flight or upon landing. Other applications and benefits of thrust-vectoring technology can be found in references 1 to 12. The applications cited in these references document the need to develop extremely versatile nozzles.

Various nozzle concepts for thrust vectoring have been investigated over the past 12 years at Langley Research Center (refs. 13 to 24). In particular, both axisymmetric and two-dimensional (2-D) nozzles have been studied. These studies emphasized 2-D nozzles because their geometry accommodates a larger variety of devices in the development of vectored thrust. These devices include internal divergent flaps, external vanes, and plugs. Early research was limited to single-plane vectoring in the pitch direction (refs. 16 to 19). More recent experiments added yaw capability to pitch-vectoring nozzles to obtain multiaxis vectoring (refs. 20 to 24). Results show that, in some cases, performance in one of the vectoring directions is compromised by the devices needed to provide vectoring in the other direction. For instance, physical interference between pitch and yaw flaps can limit the range of available multiaxis vector angles. Also, combining pitch and yaw vectoring with dissimilar vectoring methods or in an asymmetrical fashion may favor one direction over the other.

A multiaxis thrust-vectoring nozzle concept designed to reduce this compromise has been investigated experimentally to evaluate its internal

performance and to assess its potential. The unique geometry associated with this nozzle allows for a new approach to achieve large-angle multiaxis thrust vectoring without physical interference of the divergent flaps. The nozzle is a nonaxisymmetric, convergent-divergent design with symmetry about the vertical and horizontal axes. Thrust is vectored through the deflection of the nozzle divergent flaps (either top and bottom or side flaps) about a hinge line near the throat plane, the location of minimum cross-sectional flow area in the nozzle. Corner pieces between adjacent pitch and yaw vector flaps contain exhaust flow at the nozzle corners. The resulting geometry is a nozzle with a cruciform cross section at the nozzle exit. To turn the flow in the pitch direction, the top and bottom flaps are rotated in the same direction through the same angle; a similar movement of the side flaps provides yaw vectoring. The design includes two additional capabilities to meet possible performance needs of future fighter aircraft. First, the nozzle can operate in a vertical-thrust mode for short and vertical takeoffs and landings, and second, the nozzle can operate in a thrust-reversing capacity.

This cruciform nozzle, so named for its distinctive cross-sectional shape at the nozzle exit, was tested for internal performance in the static test facilities of the Langley 16-Foot Transonic Tunnel. The nozzle was tested unvectored, vectored in one and two directions, and configured in vertical- and reverse-thrust modes at nozzle pressure ratios up to 8. Divergent flap width, nozzle expansion ratio, and nozzle power setting were varied as test parameters. In addition, several methods of achieving increased multiaxis vectoring capability at large divergent flap angles in dry power operation were examined.

Symbols

All forces and moments (with the exception of resultant thrust) are referred to the model centerline (body axis). The model (balance) moment reference center was located at model station (Sta.) 29.39. Reference 25 contains a discussion of the data reduction procedure and definitions of the force and moment terms and the propulsion relationships.

A	linear nozzle dimension measured from nozzle centerline to convergent flap surface at nozzle connection station (Sta. 42.24) (fig. 6(a) and table 2), in.
A_e	cross-sectional area at nozzle exit plane, in ²
A_t	cross-sectional area at nozzle throat plane, in ²

B	linear nozzle dimension measured from nozzle connection station (Sta. 42.24) to corner convergent point (fig. 6(a) and table 2), in.
C	flap width (fig. 6(a) and table 2), in.
D	linear nozzle dimension on vertical-thrust and thrust-reverser configurations measured from flap closure point to aft surface of model flap (fig. 6(c) and table 2), in.
E	longitudinal length of cutout on transition section used for vertical-thrust configurations (fig. 6(e) and table 2), in.
F_a	measured axial thrust, lbf
F_i	ideal isentropic thrust, $w_p \sqrt{\frac{R_j T_{t,j}}{g^2} \frac{2\gamma}{\gamma-1} \left[1 - \left(\frac{p_a}{p_{t,j}} \right)^{(\gamma-1)/\gamma} \right]}, \text{ lbf}$
F_n	normal force measured by balance, lbf
F_r	resultant thrust, $\sqrt{F_a^2 + F_n^2 + F_s^2}, \text{ lbf}$
F_s	side force measured by balance, lbf
G	longitudinal length of cutout on transition section used for thrust-reverser configurations (fig. 6(e) and table 2), in.
g	acceleration of gravity, 32.174 ft/sec ²
L	reference length, 1.0 in.
M_y	pitching moment measured by balance, in-lbf
M_z	yawing moment measured by balance, in-lbf
NPR	nozzle pressure ratio, $p_{t,j}/p_a$
NPR_d	design nozzle pressure ratio (NPR for fully expanded flow at nozzle exit)
p_a	atmospheric pressure, psi
$p_{t,j}$	average jet total pressure, psi
R_j	gas constant (for $\gamma = 1.3997$), 1716 ft ² /sec ² -°R
$T_{t,j}$	jet total temperature, °R
w_i	ideal isentropic weight-flow rate (for $\text{NPR} > 1.89$), $A_t p_{t,j} \left(\frac{2}{\gamma+1} \right)^{\frac{\gamma+1}{2(\gamma-1)}} \sqrt{\frac{\gamma g^2}{T_{t,j} R_j}}, \text{ lbf/sec}$

w_p	measured weight-flow rate, lbf/sec
x	longitudinal thrust-reverser dimension measured from downstream port corner without port extension to aft surface of corner piece (fig. 6(d) and table 2), in.
y	linear thrust-reverser dimension measured from nozzle centerline to center of internal radius (fig. 6(d) and table 2), in.
y_b	linear nozzle dimension measured from nozzle centerline to center of bottom-flap throat radius (fig. 6(a) and table 2), in.
y_l	linear nozzle dimension measured from nozzle centerline to center of left-flap throat radius (fig. 6(a) and table 2), in.
y_r	linear nozzle dimension measured from nozzle centerline to center of right-flap throat radius (fig. 6(a) and table 2), in.
y_t	linear nozzle dimension measured from nozzle centerline to center of top-flap throat radius (fig. 6(a) and table 2), in.
z	linear vertical-thrust configuration dimension measured from nozzle centerline to downstream port corner (fig. 6(c) and table 2), in.
z_b	linear nozzle dimension from nozzle centerline to trailing edge of bottom flap (fig. 6(a) and table 2), in.
z_l	linear nozzle dimension from nozzle centerline to trailing edge of left flap (fig. 6(a) and table 2), in.
z_r	linear nozzle dimension from nozzle centerline to trailing edge of right flap (fig. 6(a) and table 2), in.
z_t	linear nozzle dimension from nozzle centerline to trailing edge of top flap (fig. 6(a) and table 2), in.
γ	ratio of specific heats, 1.3997 for air
δ_p	pitch thrust-vector angle, measured from centerline, positive deflection downward, $\tan^{-1} \frac{F_n}{F_a}$, deg

$\delta_{v,p}$	geometric vector angle in pitch plane, measured from centerline, positive deflection downward, deg
$\delta_{v,y}$	geometric vector angle in yaw plane, measured from centerline, positive deflection to left looking upstream, deg
δ_y	yaw thrust-vector angle, measured from centerline, positive deflection to left looking upstream, $\tan^{-1} \frac{F_s}{F_a}$, deg

Abbreviations:

A/B	afterburning power
C-D	convergent-divergent
SERN	single-expansion-ramp nozzle
Sta.	model station, in.
2-D	two-dimensional

Test Facility

The test was conducted in two phases in the static test facilities of the Langley 16-Foot Transonic Tunnel. The dry power nozzles were tested in the model preparation area, a facility normally used for model setup and calibration before entrance into the wind tunnel. However, because the model preparation area has a high-pressure air supply and a data acquisition system, it can be used to test the internal performance of nozzles at wind-off conditions. The air system uses the same supply of clean, dry air used in the wind tunnel propulsion simulations; the system includes the same valving, filters, and heat exchanger to provide an air supply at a constant total temperature of about 530°R. The model was mounted on a sting-strut support system in a soundproof room with an air exhaust duct opposite the jet. The control room is adjacent to the test area, and a window between the rooms allows for model observation during testing.

The afterburning power nozzles were tested in the static test stand of the 16-Foot Transonic Tunnel. The static test stand is separate from the wind tunnel and thus has its own air supply system, valving, filters, and heat exchanger. The model was attached to a dolly-mounted strut support system, and the air exhausted into a vented room. Reference 26 provides details of both facilities.

Propulsion Simulation System

Figure 1(a) shows the propulsion simulation system with a typical cruciform nozzle configuration

installed and figure 1(b) shows the internal details of the test hardware. High-pressure, constant-temperature air is supplied to the propulsion simulation system so that the forces and moments produced by the nozzle can be measured accurately. As shown in figure 1(b), air is supplied through six lines in the support strut to an annular high-pressure plenum. The air flows radially out of the high-pressure plenum through eight equally spaced sonic nozzles into a low-pressure plenum. This flow transfer design (perpendicular to the nozzle axis) minimizes the force on the balance caused by axial momentum transfer of the flow across the force balance. Flexible bellows act as seals between the metric (supported by the force balance) and nonmetric portions of the model and minimize forces caused by pressurization. The air then passes through a choke plate for flow straightening, through an instrumentation section, through a circular-to-octagonal transition section, and into the nozzle; the air then exhausts to atmospheric pressure. The instrumentation section includes an iron-constantan thermocouple for total temperature measurements and a rake of nine pitot probes for total pressure measurements.

Nozzle Design

The cruciform nozzle is a fully variable, non-axisymmetric, convergent-divergent nozzle designed to turn the flow in both pitch and yaw directions through the deflection of divergent flaps into or away from the flow. Figure 2 is a close-up of a typical model, and figures 3 and 4 show external and internal views of the various configurations tested. Interchangeable blocks are used to simulate deflectable divergent flaps in the model. The goal of the design is to accomplish multiaxis thrust vectoring while minimizing the physical interference between the pitch and yaw flaps. Each of the four divergent flaps moves in a channel and has a pivot point near the throat plane. (See fig. 3(c).) The channel sidewalls extend to the nozzle exit plane to provide flow containment. The nozzle is designed to operate in both dry and afterburning (A/B) power modes. Operation in A/B mode requires that the throat be widened to accommodate the lower density flow that results from the higher exhaust gas temperatures associated with afterburning.

In the A/B power mode, the pitch (top and bottom) and yaw (side) flaps do not physically interfere with each other at normal vectoring angles. In the dry power mode, the flaps do not interfere at low multi-axis vectoring angles; the flaps do, however, interfere with each other at higher angles (i.e., angles usually greater than 10° , but actual size depends on the

specific geometry). The pitch and yaw flaps are free from physical interference until an inward-deflected flap moves into the path of an adjacent flap. Two concepts for eliminating this physical interference at higher multi-axis vectoring angles have been investigated and are subsequently described.

The nozzle is also designed to have the multifunctional capabilities of providing vertical thrust for short and vertical takeoffs and landings and reverse thrust for aircraft deceleration. In the vertical-thrust mode, the divergent flaps move together to close the exit. The convergent bottom flap pivots open about a hinge point at the throat and thus creates a ventral port. (See fig. 5(a).) The designed turning angle in the vertical-thrust mode is 90° . In the thrust-reverser mode, the divergent flaps close in the same way. However, the reverser is deployed by the left and right convergent flaps that pivot open about the hinge point at the throat. (See fig. 5(b).) The designed turning angle in reverse mode is 120° . The total port areas of both the vertical-thrust and the thrust-reverser configuration are scheduled to maintain a sufficient air flow through the engine.

A model of the nozzle was built with interchangeable blocks used to represent flaps for each vectoring configuration. The nominal throat area was 4 in^2 in dry power mode and 8 in^2 in A/B power mode. Port areas of 4 in^2 were used in both vertical-thrust and thrust-reverser configurations. Model dimensions and configuration specifications are presented in tables 1 and 2 and in figure 6. The model was tested both with narrow flaps and with wide flaps to investigate the effect of flap width on nozzle performance and thrust-vectoring capability. The cross-sectional flow areas for the two configurations with different flap width were kept as nearly equal as possible. All yaw flaps were arbitrarily chosen to have unrestricted freedom of movement; any restrictions of movement necessary to eliminate flap interference were applied to the pitch flaps. The nozzle was otherwise symmetrical, so the pitch- and yaw-vectoring results were interchangeable if desired. The model was built so that pitch vectoring deflected the flow down to give a positive force (up) and yaw vectoring deflected the flow to the right to give a negative force (left) looking upstream. The nominal geometric flap angle in thrust vectoring was 20° for both pitch and yaw. The L-shaped corner pieces (fig. 2) that formed the flap channels were designed for static (no external flow) tests only; actual flight nozzle hardware would have smoothly faired external surfaces and little or no base area.

As mentioned previously, two concepts for extending the multi-axis vectoring angles beyond the

physical constraint in dry power operation were examined. A configuration called restricted flap (figs. 3(d) and 4(d)) allowed the trailing edge of the upper pitch flap to move to the edge of the yaw flap channel but restricted the trailing edge from moving farther. Thus, unrestricted yaw flap movement is allowed. The bottom flap was then rotated through the full 20° angle. Another configuration called shifted throat (figs. 3(d) and 4(d)) moved the top and bottom convergent flaps so that the throat plane shifted upward. This movement allowed the top pitch flap to rotate closer to 20° before being restricted by the yaw channel. Shifting the flow passage to allow greater vectoring angles represents a new approach to handle the problem of flap interference. The restricted-flap and shifted-throat configurations were each tested at two exit-to-throat area ratios and at two flap widths.

The vertical-thrust and thrust-reverser configurations were tested with and without port length extensions to assess their effect on nozzle performance. A port extension of 1.500 in. was tested on the vertical-thrust configurations, and port extensions of 0.750 and 1.500 in. were tested on the reverse-thrust configurations. (See figs. 5(a), 5(b), 6(c), and 6(d).)

Instrumentation

The weight-flow rate of air to the nozzle was calculated from pressure and temperature measurements in a calibrated venturi system upstream of the high-pressure plenum. The air supply in the model preparation area was connected to the same multiple critical venturi as that used for the 16-Foot Transonic Tunnel. The air supply in the static test stand passed through a separate pair of critical venturis. All pressures in this test were measured by individual pressure transducers. Forces and moments were measured by a six-component strain-gauge balance located on the nozzle centerline.

Data Corrections and Presentation

Each data point is the average steady-state value computed from 50 frames of data taken at a rate of 10 frames per second. All data were taken in ascending order of the average jet total pressure $p_{t,j}$. The data obtained from this test are given in table 3. Most of the data presented are plotted as a function of nozzle pressure ratio (NPR), the ratio of jet total pressure to atmospheric pressure. The NPR range of 2 to 8 corresponds typically to the operational NPR for flight Mach numbers from 0.2 to 1.3.

The strain-gauge balance measurements, from which the actual nozzle thrust components are subsequently obtained, are initially corrected for balance

interactions. Although the bellows arrangement is designed to eliminate pressure and momentum interactions with the balance, small bellows tares on the six balance components still exist. These tares result from a small pressure difference between the ends of the bellows, which occurs when internal velocities are high, and from small differences in the spring constants of the forward and aft bellows, which occur when the bellows are pressurized. These bellows tares are determined from tests of standard axisymmetric calibration nozzles with known performance over a range of expected internal pressures and longitudinal and lateral forces and moments. The balance data are then corrected in a manner similar to that discussed in reference 16 to obtain thrust along the body axis F_a , normal force F_n , and side force F_s . The resultant thrust ratio F_r/F_i , axial thrust ratio F_a/F_i , normal-force ratio F_n/F_i , and resultant pitch and yaw thrust-vector angles δ_p and δ_y are then determined from these corrected balance data. References 25 and 26 contain a more detailed discussion of this data reduction process.

The discharge coefficient w_p/w_i is the ratio of measured weight-flow rate from upstream venturi measurements to ideal weight-flow rate, which is calculated from total pressure and temperature measurements and the geometric nozzle throat area. This discharge coefficient is a measure of the nozzle efficiency in passing weight flow. The ideal weight-flow calculation is sensitive to the throat area of the nozzle used in the calculation; thus, a small discrepancy between measured and actual throat area can significantly change the discharge coefficient level. Since the throat areas of the cruciform nozzle are difficult to measure, nominal values are used in the calculations and are listed in table 1.

The basic performance parameters presented in this report are resultant thrust ratio F_r/F_i , axial thrust ratio F_a/F_i , discharge coefficient w_p/w_i , and resultant pitch and yaw thrust-vector angles δ_p and δ_y . The normal-force ratio F_n/F_i is used to compare single and multiaxis thrust-vectoring capability. Although pitching-moment and yawing-moment ratios $M_y/F_i L$ and $M_z/F_i L$ were measured and recorded in table 3, they are not discussed because this report emphasizes forces. Rolling-moment data are not included because they are not relevant to this nozzle design.

Discussion of Results

Basic Data

The basic data for each configuration of this investigation are presented in figures 7 to 10 for

the dry power configurations and in figure 11 for the afterburning power configurations with nominal divergent flap deflections of 20° . In general, many of the basic data show trends that are consistent with previous studies (refs. 13 to 15). One trend is the occurrence of peak values of F_r/F_i (for the unvectorized nozzle) at slightly higher values of NPR than that of the NPR_d listed in table 1. The NPR_d is the design NPR and is calculated from the nozzle area ratio (A_e/A_t , ratio of nozzle exit plane area to nozzle throat plane area) with the assumption that the nozzle expands isentropically (ref. 27). Thrust losses at nozzle pressure ratios below and above NPR_d are associated with nozzle overexpansion and underexpansion.

The deflection of divergent flaps for thrust vectoring generally results in a decrease in resultant thrust ratio. In some cases, particularly at larger area ratios ($A_e/A_t = 1.5$ and 1.4), two local maximums occur in F_r/F_i with the deflection of the divergent flaps; one occurs at high NPR and one occurs at low NPR. (See figs. 8 and 10.) The same behavior is present in the axial thrust ratio. In addition, some performance curves (F_a/F_i and F_r/F_i) have multiple distinct local peaks with the deflection of flaps. Two possible explanations exist for this behavior. First, at low NPR's, internal exhaust flow separation probably occurs in the divergent channel. The large-area-ratio configurations are the most susceptible to separation. As shown by the data in reference 28, internal flow separation can cause discontinuities in the thrust ratio curves. Second, when the divergent flaps are deflected for thrust vectoring, the flaps have unequal lengths referenced to the flow centerline. Therefore, near the nozzle exit, part of the exhaust flow is bounded by a solid surface and part is unbounded. In this case, the nozzle geometry is similar to that of a single-expansion-ramp nozzle (SERN) designed to allow partially unbounded expansion. As shown in reference 23, these nozzles either have discontinuities in their thrust ratio performance curves or have two distinct performance peaks.

The discharge coefficient is relatively constant with NPR's above the choked flow condition ($NPR > 1.89$). The deflection of divergent flaps for thrust vectoring generally results in a decrease in discharge coefficient. This decrease is most likely a result of a decrease in effective nozzle throat area. The throats of two-dimensional convergent-divergent (2-D C-D) nozzles with divergent flap thrust vectoring have been shown to pivot and translate onto the divergent flaps and decrease in area (ref. 19). The same phenomenon is believed to occur here. In some

cases of multiaxis thrust vectoring, the decrease in discharge coefficient is nearly 11 percent.

In general, the resultant pitch and yaw thrust-vector angles show a dependency on NPR. The trend in pure pitch vectoring is an increase in pitch thrust-vector angle with increasing values of NPR in the low-NPR range, probably as the low-energy separated exhaust flow begins to reattach on the divergent flap. The resultant pitch thrust-vector angle generally reaches a maximum value and then decreases as NPR increases. The resultant thrust-vector angles in multiaxis thrust vectoring generally show effective thrust vectoring (little adverse flow separation and therefore large angles) at low NPR's.

The thrust-vector angles in single-axis and multi-axis thrust vectoring are less than the nominal flap deflection angle of 20° . This apparent deficiency in thrust vectoring is caused by the divergent channel geometry of the cruciform nozzle. Sketches of cross sections at the exit planes of the narrow- and wide-flap configurations are shown in figure 12. The deflection of the pitch flaps divides the exhaust flow into a center region that is deflected and side regions that are not. The resultant thrust vector equals the sum of these components and thus has an angle smaller than the flap deflection angle because of the undeflected exhaust regions. A more realistic thrust-vector angle for comparison than 20° is an area-weighted flap deflection angle. The percentages of the area at the exit plane enclosed between opposing divergent flaps are 65 and 75 percent for the narrow- and wide-flap configurations. Therefore, 13° and 15° are more appropriate angles by which to judge thrust-vectoring capability for the narrow- and wide-flap configurations. (These angles are 65 and 75 percent of 20° .) As shown in the basic data (figs. 7 to 10), thrust-vector angles of these magnitudes are reached and occasionally exceeded, which demonstrates that the flaps are turning the flow effectively. A similar argument concerning exhaust flow splitting and regional contribution applies in multi-axis thrust vectoring as well.

In the afterburning configuration, the percentages of enclosed area at the exit planes are 57 and 63 percent for the narrow- and wide-flap configurations. Therefore, the equivalent thrust-vector angles for comparison are 11.4° and 12.6° . As shown in figure 11, these angles are achieved only in multi-axis thrust vectoring, with the exception that the angle for the wide-flap configuration at $A_e/A_t = 1.2$ also surpasses 12.6° in single-axis thrust vectoring. An obvious drawback to the cruciform design is that large flap deflections are necessary to produce the desired thrust-vector angle.

Summary Data

Since applications of the cruciform nozzle would normally be with it operating at peak thrust efficiency, the data are summarized and the configurations are compared at peak resultant thrust ratio. In figure 13, the data are arranged by power setting, flap width, and area ratio. The bars in the bar chart are composed of data from the unvectored, pitch-vectoring, and multiaxis-vectoring configurations of the basic pitch, restricted-flap, and shifted-throat concepts.

Peak resultant thrust ratios of 2-D C-D nozzles typically range from 0.985 to 0.995 (refs. 19 and 24). The peak resultant thrust ratios measured for the unvectored cruciform nozzle range from 0.981 to 0.990; this performance is up to 1.4 percent lower than that of typical 2-D C-D nozzles. The slightly lower performance of the cruciform nozzle may be a result of additional surface friction losses because of a larger internal surface area. A decrease in peak resultant thrust ratio occurs with the addition of pitch thrust vectoring and again with the addition of yaw thrust vectoring. The decreases in peak resultant thrust ratio for the pitch-vectoring cruciform nozzles are larger than the decreases for pitch-vectoring 2-D C-D nozzles that deflect internal divergent flaps for thrust vectoring. These decreases are probably a result of internal flow interactions and shear losses in the complex flow field of the cruciform nozzle. As previously discussed, deflecting the divergent flaps creates a region of deflected flow and regions of undeflected flow; shear losses between these flows contribute to the overall decrease in thrust efficiency of the nozzle. Adding yaw vectoring to pitch vectoring results in an additional decrease in peak resultant thrust ratio; this decrease is generally greater than that of pure pitch vectoring. These losses are partially attributable to adverse interactions in the complex internal flow field of the cruciform nozzle.

Another probable contributor to the large losses in multiaxis thrust vectoring is localized supersonic flow turning, an inefficient process because of the oblique shocks that are formed in the divergent channel. Studies of internal pitch thrust-vectoring 2-D C-D nozzles have shown that flow turning is almost entirely subsonic because the throat is inclined toward the direction of flow turning. The same phenomenon probably occurs in the single-axis thrust-vectoring configuration of the cruciform nozzle; that is, the throat in pitch vectoring is inclined so that most of the exhaust flow passing through the throat is already turned in the pitch plane and can expand without further changes in direction. In multiaxis thrust vectoring, the throat of the cruciform nozzle

is inclined in both the pitch and the yaw plane, so exhaust flow passing through the throat moves in a direction roughly 45° from both the vertical and the horizontal plane or along the bisector of the pitch and yaw channels. However, because nearly all flow exits the nozzle through the pitch and yaw channels, the flow must be redirected after passing through the throat to follow the walls of the channels. In other words, the channel sidewalls are turning supersonic flow, and this action is shown in the thrust performance as a significant decrease in F_r/F_i . Since the throat of the pitch-vectoring nozzle turns most of the exhaust flow in the correct direction for expansion, supersonic readjustments are seldom necessary, and most of the losses are from shear.

A comparison of the data in figure 13 shows that the restricted-flap configurations have up to 2 percent higher peak resultant thrust ratios in both single-axis and multiaxis thrust vectoring than the shifted-throat configurations. The larger thrust losses for the shifted-throat configurations may be related to throat inclination. When the throat is shifted, the exhaust flow first turns in the opposite direction of vectoring upstream of the throat and then turns back through a greater angle in the direction of thrust vectoring. A throat plane that is inclined to the oncoming flow may still be relatively orthogonal to the nozzle axis. Additional flow turning in the supersonic region is necessary for the flow to expand down the pitch channel and thus results in supersonic turning losses.

The effect of area ratio A_e/A_t on the peak resultant thrust ratio is generally small. Increasing the flap width increases the peak resultant thrust ratios, particularly in single-axis thrust vectoring. As the flap width is increased, the geometry approaches that of a 2-D C-D nozzle, and therefore the performance is expected to also approach that of a 2-D C-D nozzle. In general, the peak resultant thrust ratios of the wide-flap nozzle are 1 to 2 percent higher than those of the narrow-flap nozzle. Previous research on pitch-vectoring 2-D C-D nozzles has shown that thrust vectoring can be accomplished with almost no losses in thrust (ref. 19).

The peak resultant thrust ratios of the nozzle in the afterburning mode are generally similar to those of the dry power mode. The most significant difference is that the benefit of having wider flaps shown for the dry power mode is not present during vectoring operation. In the afterburning mode, the wide-flap configuration does not approximate the geometry of a 2-D C-D nozzle any more than does the narrow-flap configuration. The thrust vectoring

losses associated with the cruciform geometry are therefore still dominant.

A comparison of the effects of various thrust-vectoring configurations on the pitch thrust-vector angles of the pitch-vectoring nozzle is shown in figure 14. The most significant effects occur at low range of NPR's. Here the shifted-throat configuration provides the most pitch vectoring for the narrow-flap nozzle, and the basic pitch configuration provides the most pitch vectoring for the wide-flap nozzle. In both situations the angle of the inward-deflected pitch flap with respect to the oncoming flow is larger than that for any other configuration of the same flap width. This large flap deflection reduces the adverse flow separation from the opposite flap at low NPR's. Above a certain NPR, pitch vector angles of the various pitch-vectoring configurations differ by less than 1° . The peak resultant thrust ratios occur in this region of NPR's.

The effect on the nozzle normal-force ratio F_n/F_i of adding yaw thrust vectoring to pitch thrust vectoring is presented in figure 15 and figure 16 for the dry power and afterburning power modes. As shown in figure 15, the coupling between pitch and yaw deflections on the dry power nozzle is dependent on geometry and NPR. For example, the narrow-flap configuration at $A_e/A_t = 1.3$ has a small decrease in normal-force ratio caused by the addition of yaw vectoring to pitch vectoring over a large NPR range. The wide-flap configuration at $A_e/A_t = 1.2$, however, has a large decrease in normal-force ratio. The effect of adding yaw vectoring to the pitch-vectoring afterburning configurations, shown in figure 16, is to increase the normal-force ratio across the NPR range. The exception is the wide-flap configuration at $A_e/A_t = 1.2$.

The yaw thrust-vector angles produced in multi-axis thrust vectoring by the restricted-flap and shifted-throat configurations are presented in figure 17. The method of thrust vectoring has little effect on the yaw thrust-vector angles produced by the nozzle.

The multi-axis thrust-vectoring capability of the cruciform nozzle is summarized in figure 18. The thrust-vector angles are presented for the condition of peak resultant thrust ratio; as previously discussed, this condition represents a realistic operational configuration. The conditions of equal pitch and yaw thrust-vector angles, shown as 45° lines through the plots, represent the goal of the cruciform nozzle design to provide equal levels of thrust vectoring in pitch and yaw.

In dry power operation, equal thrust-vector angles are not achieved because of the asymmetry required to allow multi-axis thrust vectoring. With the exception of the narrow-flap configuration at $A_e/A_t = 1.3$, the ability of the shifted-throat configuration to produce equal pitch and yaw thrust-vector angles is equal to or greater than that of the restricted-flap configuration. Equal pitch and yaw thrust-vector angles are produced by the afterburning configurations of the cruciform nozzle because of nozzle symmetry. The divergent flaps of the afterburning configurations do not physically interfere and therefore do not need modifications.

Figure 18(a) shows that the shifted-throat configuration generally provides larger pitch thrust-vector angles than those of the restricted-flap configurations and that the benefits are greater for the wide-flap nozzle. Shifting the throat also generally produces a larger yaw thrust-vector angle. More equal thrust-vector angles are achieved by the narrow-flap nozzle. Increasing the area ratio A_e/A_t increases the magnitude of both the pitch and the yaw thrust-vector angle. Moreover, increasing the flap width decreases the pitch thrust-vector angle. In afterburning operation (fig. 18(b)), increasing the flap width increases both the pitch and the yaw thrust-vector angle.

Vertical-Thrust Mode

The thrust performance, discharge coefficient, and resultant thrust-vector angles for the nozzle in the vertical-thrust mode (fig. 5(a)) are shown in figure 19. The length-to-width ratios for the port openings associated with the narrow- and wide-flap configurations are about 2.6 and 1.5. Both have the same physical port area of 4 in^2 .

As shown in figure 19(a), the resultant thrust ratios for both nozzles are high, considering that the internal geometry is not specifically designed to turn the flow smoothly in the vertical-thrust mode. The resultant thrust ratio of the narrow-flap configuration varies from 0.964 at $\text{NPR} = 3.0$ to 0.955 at $\text{NPR} = 6.6$. The wide-flap resultant thrust ratio varies from 0.974 at $\text{NPR} = 2.5$ to 0.960 at $\text{NPR} = 5.5$. Thrust performance for a similar 90° flow-turning nozzle with a rectangular port and a sharp upstream port corner was measured by Re and Mason (ref. 29). The resultant thrust ratios ranging from 0.980 at $\text{NPR} = 3$ to 0.950 at $\text{NPR} = 7$ that were obtained for that nozzle are comparable to those of the current nozzle.

The discharge coefficient in the vertical-thrust mode shows a dependence on NPR that is not present in the cruise configuration. The narrow-flap nozzle

discharge coefficient is 0.826 at $\text{NPR} = 2.0$ and increases to 0.865 at $\text{NPR} = 6.6$. The wide-flap nozzle discharge coefficient is 0.796 at $\text{NPR} = 2.0$ and increases to 0.848 at $\text{NPR} = 6.0$. This variation of discharge coefficient is the result of changes in the effective exit area of the port. The variance of discharge coefficient with NPR suggests that the flow pattern in the nozzle does not stabilize until the discharge coefficient levels out at about $\text{NPR} = 3.5$. The nozzle tested by Re and Mason achieved discharge coefficients from 0.750 at $\text{NPR} = 2$ to 0.840 at $\text{NPR} = 7$ (ref. 29); these coefficients are slightly lower than the values measured for the current nozzle.

The low discharge coefficients of the vertical-thrust nozzles suggest that the effective port area for the flow is smaller than the actual port area used in the ideal weight-flow calculation (4 in^2). A flow separation region probably exists on the upstream wall of the port at the sharp corner (fig. 5(a)) and thus reduces the effective port area and consequently the weight flow through the nozzle. Re and Mason concluded that a corner radius on the upstream port corner increases discharge coefficient by 5 to 10 percent (ref. 29). The asymptotic behavior of discharge coefficient with increasing NPR supports the theory of a separated region, since a separation region would diminish in size at higher pressure ratios because of the added energy in the flow. As shown in figure 19(a), the wide-flap nozzle has a 2-percent-lower discharge coefficient than the narrow-flap nozzle. If the regions of separated flow in the two ports extend the same distance from the upstream wall, the wide-flap configuration loses more effective port area than does the narrow-flap configuration. This difference results in a lower discharge coefficient.

The resultant thrust-vector angle also shows a dependence on the port width and NPR . The wide-flap nozzle deflects the thrust up to 87° , about 2° more than does the narrow-flap nozzle. Possible reasons for better thrust deflection of the wide-flap configuration are that the wide-flap nozzle has more surface area on the external expansion surface to turn the flow and that the longer port length of the narrow-flap configuration probably allows more mass flow to escape the port before being turned. Despite the increase in thrust-vector angle with NPR , neither nozzle is capable of completely deflecting the thrust 90° (vertical).

In figure 19(b), the performance data are presented for the same configurations as those presented in figure 19(a) with a 1.500-in. port length extension installed (fig. 5(a)). The resultant thrust ratios and discharge coefficients are not significantly affected by the presence of the port extension. The resultant thrust-vector angle, however, is greatly increased.

The port extension increases the thrust-vector angle beyond the geometric angle of 90° , particularly at high NPR 's. At $\text{NPR} = 6$, the narrow-flap nozzle deflects the thrust 92° and the wide-flap nozzle deflects the thrust 97° . This overdeflection is possible because the flow outside of the port is physically bounded on only one side, similar to the flow for the SERN geometry.

Thrust-Reverser Mode

In thrust-reverser mode, the nozzle exit is closed off by the divergent flaps, and the side (right and left) convergent flaps are pivoted open as though hinged at the throat to permit thrust reversing. To investigate the possible necessity of a longer port length, two port length extensions to the downstream walls were tested (fig. 5(b)): a short port length extension of 0.750 in. and a long port length extension of 1.500 in.

The effects of the thrust-reverser port length on axial thrust ratio and discharge coefficient are shown in figure 20. Large negative values of F_a/F_i represent desirable results for thrust reversers. In general, the target level of F_a/F_i is equal to the cosine of the port angle, in this case -0.5 ($\cos 120^\circ$). The axial thrust ratios show that virtually no net axial thrust (i.e., reverse thrust) is produced without the port extensions installed. Each port causes the thrust to deflect about 90° , which cancels (or spoils) the thrust of the opposite port. The configurations with the port extensions do produce reverse thrust, and this result indicates the existence of a minimum required port length extension for reversing the thrust.

The wide-flap reverser produces significantly more reverse thrust than does the narrow-flap reverser. Similar to the vertical-thrust mode, the longer port of the narrow-flap configuration probably allows more mass flow to escape the port before being turned. In fact, the wide-flap reverser with the long port extension installed produces more reverse thrust than expected, as shown by comparison of the maximum F_a/F_i (-0.62) with the target of -0.5 . This behavior has occurred in previous thrust-reverser tests (refs. 29 and 30). The low axial thrust ratio at low NPR is partially caused by the sharp upstream port corner. Re and Mason (ref. 29) concluded that increasing the corner radius raises the thrust efficiency at low NPR 's because the larger radius allows a smoother transition of the flow through the port; thus, separation at the corner is reduced.

Discharge coefficient is significantly affected by the addition of the port extensions. The discharge coefficient decreases about 10 percent when the short port length extension is installed, but only an additional decrease of 0 to 1 percent occurs when the long

port length extension is installed. The reduction in discharge coefficient is probably attributable to flow separation from the sharp upstream corners of the ports, as previously discussed for the vertical-thrust nozzle.

The narrow-flap reverser has a higher discharge coefficient than the wide-flap reverser. Discharge coefficient stabilization, or leveling out, was not completed in the NPR range tested, probably also because of the sharp upstream corner. In reference 29, Re and Mason also concluded that increasing the upstream port corner radius reduces the NPR of stabilization and significantly increases the discharge coefficient level. A rounded corner on the current reverser would probably greatly improve the performance.

Conclusions

A multiaxis thrust-vectoring nozzle with vertical-thrust and thrust-reverser capabilities was designed and tested in the static test facilities of the Langley 16-Foot Transonic Tunnel. The objective of the cruciform nozzle design was to reduce the physical interference between multiaxis thrust-vectoring flaps and to achieve high levels of combined thrust vectoring in pitch and yaw while retaining competitive performance when unvectored. Based on the discussion of the results obtained from the test, the following conclusions are considered relevant for this nozzle arrangement.

1. Resultant thrust ratios of the unvectored cruciform nozzle concept, even with its complex internal geometry, are only slightly lower (up to 1.4 percent) than those of previously tested two-dimensional convergent-divergent nozzles.
2. Thrust losses in single-axis thrust vectoring are dominated by complex flow interactions between regions of shearing flow.
3. Thrust losses in multiaxis thrust vectoring are probably dominated by the turning of supersonic flow to realign the flow direction with the channel walls.
4. Dry power nozzles that use the shifted-throat concept in multiaxis thrust vectoring generally achieve larger pitch and yaw thrust-vector angles than do the restricted-flap configurations. However, the restricted-flap configurations have up to 2 percent higher peak resultant thrust ratios than the shifted-throat configurations.
5. Dry power nozzles with narrow flaps achieve more equal resultant thrust-vector angles in pitch and yaw than do those with wide flaps. Peak resultant

thrust ratios of the wide-flap nozzles, however, are 1 to 2 percent higher than those of the narrow-flap nozzles.

6. Afterburning power nozzles achieve equal pitch and yaw thrust-vector angles, and increasing the flap width allows larger angles to be obtained.
7. The thrust performance of both the vertical-thrust and the thrust-reverser configurations are competitive with previously tested nozzles that have similar capabilities.
8. Downstream port walls of sufficient length are necessary to achieve the required high flow-turning angles of the vertical-thrust and thrust-reverser configurations.

NASA Langley Research Center
Hampton, VA 23665-5225
March 10, 1992

References

1. Herbst, W. B.: Future Fighter Technologies. *J. Aircr.*, vol. 17, no. 8, Aug. 1980, pp. 561-566.
2. Tamrat, B. F.: Fighter Aircraft Agility Assessment Concepts and Their Implication on Future Agile Fighter Design. AIAA-88-4400, Sept. 1988.
3. Frassinelli, Mark C.; and Carson, George T., Jr.: *Effect of Tail Size Reductions on Longitudinal Aerodynamic Characteristics of a Three-Surface F-15 Model With Nonaxisymmetric Nozzles*. NASA TP-3036, 1990.
4. Herbst, Wolfgang B.: X-31A. SAE Tech. Paper Ser. 871346, June 1987.
5. Ward, B. D.; and Lewis, W. J.: Advantages of Thrust Vectoring for STOVL. AIAA-87-1708, June-July 1987.
6. Herrick, Paul W.: Air Combat Payoffs of Vectoring/Reversing Exhaust Nozzles. AIAA-88-3239, July 1988.
7. Gal-Or, Benjamin: *Vectored Propulsion, Supermaneuverability and Robot Aircraft—Recent Advances in Military Aviation*. Springer-Verlag, 1990.
8. Nelson, B. D.; and Nicolai, L. M.: Application of Multifunction Nozzles to Advanced Fighters. AIAA-81-2618, Dec. 1981.
9. Mello, J. F.; and Kotansky, D. R.: Aero/Propulsion Technology for STOL and Maneuver. AIAA-85-4013, Oct. 1985.
10. Mace, J.; Smereczniak, P.; Krekeler, G.; Bowers, D.; MacLean, M.; and Thayer, E.: Advanced Thrust Vectoring Nozzles for Supercruise Fighter Aircraft. AIAA-89-2816, July 1989.
11. Poisson-Quinton, Ph.: Comments on Propulsion/Airframe Integration for Improving Combat Aircraft Operational Capabilities. *Special Course on Fundamentals*

- of Fighter Aircraft Design, AGARD-R-740, Oct. 1987, pp. 7A-1-7A-7.
12. Nguyen, Luat T.; and Gilbert, William P.: Impact of Emerging Technologies on Future Combat Aircraft Agility. AIAA-90-1304, May 1990.
 13. Berrier, Bobby L.: Results From NASA Langley Experimental Studies of Multiaxis Thrust Vectoring Nozzles. SAE Tech. Paper Ser. 881481, Oct. 1988.
 14. Capone, Francis J.; and Berrier, Bobby L.: *Investigation of Axisymmetric and Nonaxisymmetric Nozzles Installed on a 0.10-Scale F-18 Prototype Airplane Model*. NASA TP-1638, 1980.
 15. Leavitt, Laurence D.: Summary of Nonaxisymmetric Nozzle Internal Performance From the NASA Langley Static Test Facility. AIAA-85-1347, July 1985.
 16. Capone, Francis J.: *Static Performance of Five Twin-Engine Nonaxisymmetric Nozzles With Vectoring and Reversing Capability*. NASA TP-1224, 1978.
 17. Capone, Francis J.; Mason, Mary L.; and Leavitt, Laurence D.: *An Experimental Investigation of Thrust Vectoring Two-Dimensional Convergent-Divergent Nozzles Installed in a Twin-Engine Fighter Model at High Angles of Attack*. NASA TM-4155, 1990.
 18. Willard, C. M.; Capone, F. J.; Konarski, M.; and Stevens, H. L.: Static Performance of Vectoring/Reversing Non-Axisymmetric Nozzles. AIAA Paper 77-840, July 1977.
 19. Re, Richard J.; and Leavitt, Laurence D.: *Static Internal Performance Including Thrust Vectoring and Reversing of Two-Dimensional Convergent-Divergent Nozzles*. NASA TP-2253, 1984.
 20. Berrier, Bobby L.; and Mason, Mary L.: *Static Performance of an Axisymmetric Nozzle With Post-Exit Vanes for Multiaxis Thrust Vectoring*. NASA TP-2800, 1988.
 21. Capone, Francis J.; and Bare, E. Ann: *Multiaxis Control Power From Thrust Vectoring for a Supersonic Fighter Aircraft Model at Mach 0.20 to 2.47*. NASA TP-2712, 1987.
 22. Lacey, David W.; and Murphy, Richard D.: *Jet Engine Thrust Turning by the Use of Small Externally Mounted Vanes*. DTNSRDC-82/080, U.S. Navy, Jan. 1983. (Available from DTIC as AD B070 970L.)
 23. Schirmer, Alberto W.; and Capone, Francis J.: Parametric Study of a Simultaneous Pitch/Yaw Thrust Vectoring Single Expansion Ramp Nozzle. AIAA-89-2812, July 1989.
 24. Taylor, John G.: *Static Investigation of a Two-Dimensional Convergent-Divergent Exhaust Nozzle With Multiaxis Thrust-Vectoring Capability*. NASA TP-2973, 1990.
 25. Mercer, Charles E.; Berrier, Bobby L.; Capone, Francis J.; Grayston, Alan M.; and Sherman, C. D.: *Computations for the 16-Foot Transonic Tunnel—NASA, Langley Research Center*. NASA TM-86319, 1984.
 26. Staff of the Propulsion Aerodynamics Branch: *A User's Guide to the Langley 16-Foot Transonic Tunnel Complex—Revision 1*. NASA TM-102750, 1990.
 27. Liepmann, H. W.; and Roshko, A.: *Elements of Gasdynamics*. John Wiley & Sons, Inc., c.1957.
 28. Berrier, Bobby L.; and Re, Richard J.: *Investigation of Convergent-Divergent Nozzles Applicable to Reduced-Power Supersonic Cruise Aircraft*. NASA TP-1766, 1980.
 29. Re, Richard J.; and Mason, Mary L.: *Effect of Varying Internal Geometry on the Static Performance of Rectangular Thrust-Reverser Ports*. NASA TM-89061, 1987.
 30. Berrier, Bobby L.; and Capone, Francis J.: *Effect of Port Corner Geometry on the Internal Performance of a Rotating-Vane-Type Thrust Reverser*. NASA TP-2624, 1986.

Table 1. Cruciform Nozzle Configurations

(a) Unvectored and vectored configurations

Configuration	Parameter						
	Flap width	Throat area, in ²	$A_e A_t$	NPR_d	Pitch, deg	Yaw, deg	Description
1	Narrow	3.719	1.3	4.64	0	0	Baseline
2					20	0	Basic pitch
3					20	0	Restricted flap
4					20	-20	Restricted flap
5					20	0	Shifted throat
6					20	-20	Shifted throat
10		7.775	1.2	3.86	0	0	A/B baseline
11					20	0	A/B pitch
12					20	-20	A/B pitch-yaw
16		3.764	1.5	6.24	0	0	Baseline
17					20	0	Basic pitch
18					20	0	Restricted flap
19					20	-20	Restricted flap
20					20	0	Shifted throat
21					20	-20	Shifted throat
22	Wide	7.769	1.4	5.43	0	0	A/B baseline
23					20	0	A/B pitch
24					20	-20	A/B pitch-yaw
25		3.930	1.2	3.86	0	0	Baseline
26					20	0	Basic pitch
27					20	0	Restricted flap
28					20	-20	Restricted flap
29					20	0	Shifted throat
30					20	-20	Shifted throat
31		7.949	1.2	3.86	0	0	A/B baseline
32					20	0	A/B pitch
33					20	-20	A/B pitch-yaw
34		3.935	1.4	5.43	0	0	Baseline
35					20	0	Basic pitch
36					20	0	Restricted flap
37					20	-20	Restricted flap
38					20	0	Shifted throat
39					20	-20	Shifted throat
40		7.929	1.4	5.43	0	0	A/B baseline
41					20	0	A/B pitch
42					20	-20	A/B pitch-yaw

Table 1. Concluded

(b) Vertical- and reverse-thrust configurations

Configuration	Parameter				
	Flap width	Port area, in ²	Operation	Angle, deg	Extension, in.
43	Narrow	4.00	Vertical	90	0
44	Wide	4.00	Vertical	90	0
49	Narrow	4.00	Vertical	90	1.5
50	Wide	4.00	Vertical	90	1.5
45	Narrow	4.00	Reverser	120	1.5
46	Wide	4.00	Reverser	120	1.5
47	Narrow	4.00	Reverser	120	0
48	Wide	4.00	Reverser	120	0
51	Narrow	4.00	Reverser	120	0.75
52	Wide	4.00	Reverser	120	0.75

Table 2. Cruciform Nozzle Dimensions
[Dimensions in inches]

(a) Unvectored and vectored configurations

Configuration	Parameter										
	A	B	C	yt	yb	yl	yr	zt	zb	zl	zr
1	2.126	1.559	1.236	1.545	1.545	1.545	1.545	1.280	1.280	1.280	1.280
2				1.545	1.545	1.545	1.545	0.217	2.375	1.280	1.280
3				1.545	1.545	1.545	1.545	0.617	2.375	1.280	1.280
4				1.545	1.545	1.545	1.545	0.617	2.375	0.217	2.375
5				1.971	1.545	1.545	1.545	0.644	1.948	1.280	1.280
6				1.971	1.545	1.545	1.545	0.644	1.948	0.217	2.375
10				2.352	2.352	2.352	2.352	2.251	2.251	2.251	2.251
11				2.352	2.352	2.352	2.352	1.175	3.339	2.251	2.251
12				2.352	2.352	2.352	2.352	1.175	3.339	1.175	3.339
16				1.545	1.545	1.545	1.545	1.442	1.442	1.442	1.442
17				1.545	1.545	1.545	1.545	0.367	2.530	1.442	1.442
18				1.545	1.545	1.545	1.545	0.618	2.530	1.442	1.442
19				1.545	1.545	1.545	1.545	0.618	2.530	0.367	2.530
20				1.971	1.118	1.545	1.545	0.793	2.107	1.442	1.442
21				1.971	1.118	1.545	1.545	0.793	2.107	0.367	2.530
22				2.354	2.354	2.354	2.354	2.575	2.575	2.575	2.575
23				2.354	2.354	2.354	2.354	1.482	3.641	2.575	2.575
24				2.354	2.354	2.354	2.354	1.482	3.641	1.482	3.641
25	2.030	1.335	1.625	1.510	1.510	1.510	1.510	1.145	1.145	1.145	1.145
26				1.510	1.510	1.510	1.510	0.092	2.242	1.145	1.145
27				1.510	1.510	1.510	1.510	0.812	2.242	1.145	1.145
28				1.510	1.510	1.510	1.510	0.812	2.242	0.092	2.242
29				1.707	1.313	1.510	1.510	0.812	2.047	1.145	1.145
30				1.707	1.313	1.510	1.510	0.812	2.047	0.092	2.242
31				2.125	2.125	2.125	2.125	1.883	1.883	1.883	1.883
32				2.125	2.125	2.125	2.125	0.818	2.977	1.883	1.883
33				2.125	2.125	2.125	2.125	0.818	2.977	0.818	2.977
34				1.510	1.510	1.510	1.510	1.267	1.267	1.267	1.267
35				1.510	1.510	1.510	1.510	0.203	2.361	1.267	1.267
36				1.510	1.510	1.510	1.510	0.812	2.361	1.267	1.267
37				1.510	1.510	1.510	1.510	0.812	2.361	0.203	2.361
38				1.707	1.313	1.510	1.510	0.812	2.165	1.267	1.267
39				1.707	1.313	1.510	1.510	0.812	2.165	0.203	2.361
40				2.125	2.125	2.125	2.125	2.128	2.128	2.128	2.128
41				2.125	2.125	2.125	2.125	1.046	3.211	2.128	2.128
42				2.125	2.125	2.125	2.125	1.046	3.211	1.046	3.211

Table 2. Concluded

(b) Vertical- and reverse-thrust configurations

Configuration	Parameter											
	Operation	A	B	C	D	E	G	x	y	yb	yt	z
43	Vertical	2.126	1.559	1.236	0.675	2.424				1.545	1.545	2.890
44	Vertical	2.030	1.335	1.625	0.656	1.649				1.510	1.510	2.830
45	Reverser	2.126	1.559	1.236	0.675		1.937	4.543	1.545			2.460
46	Reverser	2.030	1.335	1.625	0.656		1.547	4.531	1.510			2.403
47	Reverser	2.126	1.559	1.236	0.675		1.937	4.543	1.545			2.460
48	Reverser	2.030	1.335	1.625	0.656		1.547	4.531	1.510			2.403
49	Vertical	2.126	1.559	1.236	0.675	2.424				1.545	1.545	2.890
50	Vertical	2.030	1.335	1.625	0.656	1.649				1.510	1.510	2.830
51	Reverser	2.126	1.559	1.236	0.675		1.937	4.543	1.545			2.460
52	Reverser	2.030	1.335	1.625	0.656		1.547	4.531	1.510			2.403

Table 3. Cruciform Nozzle Data

Configuration 1									
NPR	w_p/w_i	F_r/F_i	F_s/F_i	δ_p	δ_y	F_n/F_i	$M_y/F_i L$	F_g/F_i	$M_z/F_i L$
2.00	0.9744	0.9049	0.9048	-1.00	-0.34	-0.0158	0.2274	-0.0054	-0.0742
2.50	0.9754	0.9349	0.9349	-0.33	-0.12	-0.0054	0.0950	-0.0020	-0.0860
3.00	0.9727	0.9534	0.9534	0.10	-0.23	0.0017	-0.0071	-0.0038	-0.0317
3.51	0.9741	0.9652	0.9652	0.09	-0.16	0.0015	-0.0070	-0.0027	-0.0286
3.98	0.9719	0.9741	0.9741	0.18	-0.14	0.0031	-0.0241	-0.0023	-0.0218
4.52	0.9728	0.9770	0.9770	0.17	-0.08	0.0029	-0.0304	-0.0013	-0.0213
5.01	0.9720	0.9790	0.9790	0.18	-0.03	0.0030	-0.0343	-0.0005	-0.0155
5.53	0.9698	0.9817	0.9817	0.14	-0.01	0.0024	-0.0403	-0.0002	-0.0126
6.00	0.9705	0.9813	0.9813	0.15	0.01	0.0025	-0.0444	0.0001	-0.0110
7.01	0.9710	0.9787	0.9787	0.11	0.04	0.0019	-0.0482	0.0007	-0.0069
8.01	0.9702	0.9787	0.9787	0.09	0.06	0.0015	-0.0396	0.0010	-0.0061
Configuration 2									
NPR	w_p/w_i	F_r/F_i	F_s/F_i	δ_p	δ_y	F_n/F_i	$M_y/F_i L$	F_g/F_i	$M_z/F_i L$
2.00	0.9482	0.9171	0.9113	6.45	-0.14	0.1030	-1.6641	-0.0022	0.0696
2.52	0.9487	0.9119	0.8879	13.09	1.39	0.2065	-3.2247	0.0215	-0.3068
3.01	0.9438	0.9294	0.9029	13.70	0.36	0.2201	-3.4004	0.0057	-0.0452
3.51	0.9425	0.9398	0.9127	13.78	0.24	0.2239	-3.4205	0.0038	-0.0233
4.01	0.9415	0.9460	0.9143	14.86	0.28	0.2426	-3.6984	0.0045	-0.0322
4.50	0.9411	0.9528	0.9234	14.27	0.07	0.2349	-3.5302	0.0012	0.0172
5.01	0.9408	0.9576	0.9301	13.78	0.15	0.2280	-3.3797	0.0025	0.0066
5.52	0.9407	0.9615	0.9352	13.43	0.09	0.2233	-3.2703	0.0015	0.0130
5.99	0.9405	0.9630	0.9379	13.09	0.09	0.2181	-3.1793	0.0015	0.0139
7.03	0.9397	0.9634	0.9400	12.67	0.06	0.2113	-3.0250	0.0010	0.0182
8.01	0.9390	0.9630	0.9406	12.38	0.03	0.2065	-2.9205	0.0005	0.0185
Configuration 3									
NPR	w_p/w_i	F_r/F_i	F_s/F_i	δ_p	δ_y	F_n/F_i	$M_y/F_i L$	F_g/F_i	$M_z/F_i L$
2.00	0.9634	0.9220	0.9216	1.81	-0.48	0.0291	-0.5065	-0.0077	0.0593
2.50	0.9647	0.9418	0.9407	2.63	-0.69	0.0432	-0.6030	-0.0114	0.1447
2.99	0.9627	0.9209	0.9045	10.73	1.56	0.1713	-2.6537	0.0246	-0.4089
3.51	0.9615	0.9382	0.9198	11.36	0.30	0.1848	-2.8730	0.0048	-0.0732
4.01	0.9613	0.9459	0.9221	12.88	0.33	0.2109	-3.2761	0.0053	-0.0690
4.50	0.9602	0.9540	0.9271	13.65	0.46	0.2251	-3.4650	0.0074	-0.1063
5.01	0.9605	0.9593	0.9337	13.27	0.16	0.2202	-3.3760	0.0026	-0.0169
5.52	0.9599	0.9649	0.9404	12.94	0.13	0.2160	-3.2783	0.0021	-0.0127
6.01	0.9595	0.9672	0.9435	12.71	0.14	0.2128	-3.2048	0.0024	-0.0156
7.00	0.9588	0.9691	0.9466	12.36	0.12	0.2075	-3.0863	0.0020	-0.0056
8.02	0.9582	0.9702	0.9487	12.10	0.09	0.2035	-2.9909	0.0015	-0.0042

Table 3. Continued

Configuration 4

NPR	w_p/w_i	F_r/F_i	F_a/F_i	δ_p	δ_y	F_n/F_i	M_y/F_iL	F_s/F_i	M_z/F_iL
1.99	0.9095	0.8727	0.8293	9.16	-15.94	0.1336	-2.1045	-0.2369	3.6607
2.52	0.9120	0.8985	0.8620	10.39	-12.93	0.1581	-2.3655	-0.1979	2.9415
3.03	0.9114	0.9131	0.8782	10.43	-12.25	0.1616	-2.3566	-0.1907	2.7954
3.49	0.9102	0.9276	0.8824	12.41	-13.40	0.1942	-2.8799	-0.2102	3.0864
4.01	0.9103	0.9343	0.8776	13.33	-15.55	0.2079	-3.1005	-0.2442	3.6867
4.52	0.9097	0.9395	0.8864	12.90	-14.91	0.2030	-3.0036	-0.2360	3.5310
5.02	0.9093	0.9422	0.8938	12.33	-14.13	0.1954	-2.8589	-0.2250	3.3242
5.51	0.9089	0.9444	0.8999	11.84	-13.48	0.1886	-2.7305	-0.2157	3.1551
6.00	0.9087	0.9459	0.9037	11.67	-12.95	0.1866	-2.6861	-0.2079	3.0049
7.01	0.9088	0.9460	0.9091	11.19	-11.81	0.1798	-2.5471	-0.1901	2.6586
8.00	0.9079	0.9475	0.9136	10.74	-11.25	0.1733	-2.4147	-0.1817	2.4856

Configuration 5

NPR	w_p/w_i	F_r/F_i	F_a/F_i	δ_p	δ_y	F_n/F_i	M_y/F_iL	F_s/F_i	M_z/F_iL
2.00	0.9220	0.9021	0.8932	8.03	-0.59	0.1259	-2.3080	-0.0092	0.0367
2.50	0.9273	0.9070	0.8666	17.17	-0.40	0.2677	-4.4146	-0.0060	0.0695
3.00	0.9251	0.9272	0.8942	15.33	0.16	0.2450	-4.0202	0.0025	-0.0690
3.52	0.9238	0.9388	0.9088	14.52	0.00	0.2355	-3.8217	0.0000	0.0011
4.02	0.9239	0.9488	0.9212	13.87	0.08	0.2274	-3.6576	0.0014	-0.0153
4.50	0.9238	0.9539	0.9283	13.30	0.11	0.2195	-3.4878	0.0018	-0.0148
5.02	0.9235	0.9576	0.9338	12.81	0.12	0.2123	-3.3437	0.0020	-0.0081
5.51	0.9229	0.9598	0.9373	12.43	0.11	0.2065	-3.2347	0.0019	-0.0082
6.00	0.9224	0.9609	0.9393	12.16	0.13	0.2023	-3.1442	0.0021	-0.0044
7.00	0.9215	0.9611	0.9409	11.76	0.10	0.1959	-3.0117	0.0017	0.0016
8.02	0.9207	0.9607	0.9414	11.51	0.09	0.1917	-2.9077	0.0015	-0.0001

Configuration 6

NPR	w_p/w_i	F_r/F_i	F_a/F_i	δ_p	δ_y	F_n/F_i	M_y/F_iL	F_s/F_i	M_z/F_iL
2.03	0.8709	0.8726	0.8156	14.54	-15.53	0.2116	-3.6083	-0.2267	3.4570
2.53	0.8702	0.8923	0.8375	16.10	-12.84	0.2417	-4.0075	-0.1909	2.8490
3.01	0.8690	0.9048	0.8546	14.46	-13.13	0.2203	-3.5521	-0.1993	2.9198
3.54	0.8687	0.9109	0.8625	13.06	-13.92	0.2001	-3.1602	-0.2138	3.1352
4.05	0.8677	0.9177	0.8670	13.02	-14.50	0.2005	-3.1142	-0.2242	3.3041
4.56	0.8678	0.9225	0.8723	13.10	-14.23	0.2029	-3.1114	-0.2212	3.2178
5.07	0.8674	0.9243	0.8764	12.93	-13.71	0.2012	-3.0872	-0.2139	3.0850
5.56	0.8671	0.9253	0.8802	12.53	-13.30	0.1956	-2.9952	-0.2081	2.9782
6.10	0.8663	0.9240	0.8820	11.75	-13.10	0.1834	-2.7501	-0.2053	2.9088
7.10	0.8657	0.9262	0.8881	11.07	-12.52	0.1738	-2.5898	-0.1972	2.7492
8.11	0.8654	0.9258	0.8902	10.59	-12.16	0.1664	-2.4442	-0.1919	2.6302

Table 3. Continued

Configuration 10

NPR	w_p/w_i	F_r/F_i	F_a/F_i	δ_p	δ_y	F_n/F_i	M_y/F_iL	F_s/F_i	M_z/F_iL
1.99	0.9717	0.9319	0.9319	0.48	0.08	0.0079	0.0874	0.0013	-0.0276
2.50	0.9734	0.9577	0.9577	0.01	0.08	0.0002	0.1062	0.0013	-0.0323
2.99	0.9741	0.9710	0.9710	-0.06	0.03	-0.0011	0.0877	0.0006	-0.0217
3.50	0.9748	0.9802	0.9802	-0.08	0.07	-0.0014	0.0704	0.0013	-0.0224
3.99	0.9742	0.9846	0.9846	-0.07	0.06	-0.0012	0.0602	0.0011	-0.0236
4.49	0.9747	0.9856	0.9856	-0.11	0.04	-0.0019	0.0562	0.0007	-0.0174
4.99	0.9741	0.9856	0.9856	-0.08	0.08	-0.0014	0.0482	0.0013	-0.0147
5.49	0.9743	0.9843	0.9843	-0.07	0.10	-0.0012	0.0463	0.0017	-0.0119
5.99	0.9733	0.9833	0.9833	-0.06	0.11	-0.0011	0.0426	0.0019	-0.0066

Configuration 11

NPR	w_p/w_i	F_r/F_i	F_a/F_i	δ_p	δ_y	F_n/F_i	M_y/F_iL	F_s/F_i	M_z/F_iL
2.01	0.9540	0.9567	0.9556	2.76	-0.06	0.0461	-0.4603	-0.0010	0.0234
2.56	0.9559	0.9626	0.9580	5.65	0.26	0.0947	-1.3015	0.0044	-0.0813
3.01	0.9569	0.9547	0.9425	9.10	1.00	0.1509	-2.2663	0.0165	-0.2760
3.49	0.9575	0.9568	0.9417	10.20	0.41	0.1695	-2.6016	0.0067	-0.1114
4.00	0.9584	0.9586	0.9422	10.60	0.39	0.1764	-2.7186	0.0064	-0.1009
4.49	0.9587	0.9613	0.9455	10.40	0.43	0.1736	-2.6574	0.0071	-0.0953
5.00	0.9587	0.9627	0.9475	10.19	0.41	0.1702	-2.5784	0.0068	-0.0875
5.48	0.9599	0.9630	0.9483	10.01	0.44	0.1673	-2.5064	0.0073	-0.0815
6.00	0.9594	0.9627	0.9484	9.88	0.50	0.1651	-2.4492	0.0083	-0.0837

Configuration 12

NPR	w_p/w_i	F_r/F_i	F_a/F_i	δ_p	δ_y	F_n/F_i	M_y/F_iL	F_s/F_i	M_z/F_iL
1.99	0.9072	0.9331	0.9101	9.28	-8.89	0.1487	-2.1449	-0.1423	2.1535
2.49	0.9130	0.9067	0.8405	16.10	-15.84	0.2426	-3.7120	-0.2385	3.7623
2.99	0.9148	0.9178	0.8566	15.28	-15.16	0.2341	-3.5897	-0.2321	3.6268
3.49	0.9164	0.9302	0.8778	13.91	-13.94	0.2173	-3.2840	-0.2179	3.3180
4.00	0.9170	0.9369	0.8900	13.10	-13.09	0.2071	-3.0707	-0.2070	3.1076
4.50	0.9180	0.9415	0.8978	12.60	-12.56	0.2007	-2.9374	-0.2001	2.9699
4.97	0.9184	0.9434	0.9022	12.24	-12.16	0.1957	-2.8394	-0.1944	2.8758
5.51	0.9187	0.9436	0.9046	11.94	-11.78	0.1913	-2.7527	-0.1886	2.7882
5.99	0.9180	0.9438	0.9062	11.73	-11.54	0.1881	-2.6916	-0.1850	2.7251

Table 3. Continued

Configuration 16

NPR	w_p/w_i	F_r/F_i	F_s/F_i	δ_p	δ_y	F_n/F_i	M_y/F_iL	F_z/F_i	M_z/F_iL
2.01	0.9614	0.8734	0.8733	-0.10	-0.40	-0.0015	0.0568	-0.0061	-0.0034
2.52	0.9626	0.9179	0.9179	-0.23	-0.09	-0.0037	0.1231	-0.0015	-0.0328
3.00	0.9611	0.9349	0.9349	-0.11	-0.10	-0.0018	0.0931	-0.0016	-0.0069
3.50	0.9607	0.9475	0.9475	0.04	-0.05	0.0006	0.0452	-0.0009	-0.0062
4.01	0.9589	0.9584	0.9584	0.01	0.16	0.0002	0.0563	0.0027	-0.0490
4.50	0.9584	0.9657	0.9657	-0.13	0.24	-0.0021	0.0827	0.0041	-0.0636
5.03	0.9575	0.9717	0.9717	-0.12	0.22	-0.0021	0.0752	0.0037	-0.0510
5.51	0.9570	0.9753	0.9753	-0.15	0.23	-0.0025	0.0717	0.0039	-0.0481
6.01	0.9567	0.9780	0.9780	-0.20	0.22	-0.0033	0.0637	0.0037	-0.0407
6.99	0.9553	0.9810	0.9810	-0.21	0.20	-0.0035	0.0517	0.0034	-0.0346
8.00	0.9546	0.9832	0.9832	-0.21	0.19	-0.0036	0.0465	0.0032	-0.0339

Configuration 17

NPR	w_p/w_i	F_r/F_i	F_s/F_i	δ_p	δ_y	F_n/F_i	M_y/F_iL	F_z/F_i	M_z/F_iL
2.01	0.9389	0.9473	0.9469	1.62	-0.35	0.0268	-0.5710	-0.0058	-0.0084
2.50	0.9390	0.9465	0.9453	2.94	-0.27	0.0485	-0.7801	-0.0044	-0.0042
3.01	0.9390	0.9369	0.9296	7.13	-0.29	0.1163	-1.7797	-0.0046	0.0309
3.50	0.9372	0.9229	0.9003	12.71	0.54	0.2031	-3.1417	0.0084	-0.1564
4.01	0.9379	0.9346	0.9101	13.15	0.31	0.2126	-3.2631	0.0049	-0.0890
4.51	0.9369	0.9387	0.9089	14.48	0.27	0.2347	-3.6166	0.0043	-0.0653
5.02	0.9359	0.9469	0.9180	14.20	0.30	0.2323	-3.5463	0.0047	-0.0690
5.51	0.9350	0.9530	0.9252	13.87	0.18	0.2284	-3.4571	0.0030	-0.0358
6.00	0.9349	0.9561	0.9294	13.56	0.15	0.2242	-3.3712	0.0024	-0.0245
7.00	0.9334	0.9604	0.9353	13.14	0.14	0.2183	-3.2379	0.0022	-0.0174
8.00	0.9322	0.9633	0.9393	12.80	0.10	0.2134	-3.1270	0.0016	-0.0139

Configuration 18

NPR	w_p/w_i	F_r/F_i	F_s/F_i	δ_p	δ_y	F_n/F_i	M_y/F_iL	F_z/F_i	M_z/F_iL
2.01	0.9526	0.8971	0.8966	1.81	0.54	0.0283	-0.4151	0.0085	-0.1844
2.52	0.9561	0.9409	0.9408	-0.77	-0.21	-0.0126	0.3644	-0.0035	0.0194
3.01	0.9536	0.9439	0.9423	3.29	-0.05	0.0542	-0.6877	-0.0008	-0.0087
3.51	0.9527	0.9392	0.9304	7.85	-0.16	0.1282	-1.9019	-0.0025	0.0113
4.02	0.9499	0.9329	0.9147	11.33	0.19	0.1832	-2.8282	0.0030	-0.0556
4.50	0.9512	0.9366	0.9141	12.60	0.18	0.2043	-3.1929	0.0028	-0.0520
5.00	0.9507	0.9449	0.9206	13.00	0.31	0.2125	-3.3102	0.0049	-0.0807
5.51	0.9504	0.9515	0.9273	12.93	0.33	0.2129	-3.3113	0.0053	-0.0815
5.99	0.9498	0.9567	0.9332	12.73	0.25	0.2108	-3.2639	0.0041	-0.0572
7.05	0.9507	0.9611	0.9386	12.43	0.14	0.2069	-3.1514	0.0023	-0.0283
7.93	0.9457	0.9683	0.9465	12.18	0.13	0.2043	-3.0921	0.0022	-0.0234

Table 3. Continued

Configuration 19

NPR	w_p/w_i	F_r/F_i	F_a/F_i	δ_p	δ_y	F_n/F_i	M_y/F_iL	F_s/F_i	M_z/F_iL
2.02	0.9144	0.8948	0.8625	13.69	-7.45	0.2100	-3.4767	-0.1127	1.7104
2.51	0.9174	0.8786	0.8379	11.56	-13.51	0.1714	-2.7164	-0.2012	3.0485
3.03	0.9165	0.8984	0.8601	11.49	-12.58	0.1749	-2.6694	-0.1919	2.8405
3.51	0.9151	0.9152	0.8708	12.57	-13.19	0.1942	-2.9350	-0.2041	3.0321
4.03	0.9162	0.9292	0.8638	15.54	-15.77	0.2402	-3.6553	-0.2439	3.6959
4.51	0.9161	0.9340	0.8622	16.07	-16.73	0.2483	-3.7820	-0.2592	3.9668
5.00	0.9153	0.9375	0.8708	15.35	-16.16	0.2390	-3.6026	-0.2523	3.8348
5.51	0.9146	0.9398	0.8791	14.60	-15.32	0.2290	-3.4192	-0.2408	3.6090
6.00	0.9139	0.9412	0.8849	14.01	-14.71	0.2208	-3.2718	-0.2324	3.4460
7.01	0.9134	0.9440	0.8940	13.17	-13.80	0.2093	-3.0498	-0.2196	3.1825
8.02	0.9124	0.9480	0.9024	12.60	-13.03	0.2018	-2.9059	-0.2088	2.9719

Configuration 20

NPR	w_p/w_i	F_r/F_i	F_a/F_i	δ_p	δ_y	F_n/F_i	M_y/F_iL	F_s/F_i	M_z/F_iL
2.02	0.9231	0.8782	0.8735	5.57	-2.04	0.0852	-1.5000	-0.0311	0.3499
2.54	0.9251	0.8903	0.8800	8.61	-1.27	0.1332	-2.1937	-0.0195	0.2327
3.02	0.9235	0.8960	0.8686	14.16	1.06	0.2191	-3.5909	0.0160	-0.2914
3.50	0.9232	0.9147	0.8890	13.62	0.43	0.2154	-3.5192	0.0067	-0.1301
4.02	0.9226	0.9299	0.9042	13.48	-0.24	0.2168	-3.5402	-0.0037	0.0451
4.51	0.9217	0.9390	0.9125	13.63	-0.05	0.2213	-3.5775	-0.0007	-0.0018
5.03	0.9217	0.9432	0.9150	14.02	0.17	0.2286	-3.6908	0.0027	-0.0399
5.52	0.9206	0.9473	0.9195	13.92	0.12	0.2279	-3.6821	0.0020	-0.0125
5.99	0.9197	0.9518	0.9240	13.88	0.08	0.2283	-3.6477	0.0013	-0.0012
6.99	0.9192	0.9561	0.9300	13.43	-0.01	0.2220	-3.5305	-0.0002	0.0240
7.98	0.9178	0.9589	0.9340	13.10	0.06	0.2173	-3.4263	0.0010	0.0047

Configuration 21

NPR	w_p/w_i	F_r/F_i	F_a/F_i	δ_p	δ_y	F_n/F_i	M_y/F_iL	F_s/F_i	M_z/F_iL
2.00	0.8860	0.8912	0.8484	16.24	-7.79	0.2470	-4.2180	-0.1161	1.8191
2.50	0.8882	0.8892	0.8504	13.18	-11.08	0.1991	-3.3271	-0.1665	2.5827
3.51	0.8886	0.9112	0.8543	16.50	-12.59	0.2530	-4.1093	-0.1908	2.8746
4.02	0.8887	0.9166	0.8573	15.83	-14.08	0.2431	-3.8883	-0.2151	3.2613
4.53	0.8897	0.9229	0.8666	14.82	-14.22	0.2293	-3.6168	-0.2196	3.2970
5.05	0.8903	0.9281	0.8687	15.13	-14.65	0.2349	-3.6901	-0.2270	3.4024
5.52	0.8892	0.9301	0.8703	15.37	-14.45	0.2393	-3.7583	-0.2243	3.3413
6.04	0.8869	0.9325	0.8753	14.92	-14.19	0.2332	-3.6402	-0.2213	3.2780
7.01	0.8884	0.9322	0.8808	13.83	-13.72	0.2168	-3.3482	-0.2151	3.1469
8.01	0.8873	0.9332	0.8861	12.93	-13.36	0.2035	-3.0966	-0.2104	3.0340
3.01	0.8909	0.9192	0.8639	16.51	-11.90	0.2561	-3.8963	-0.1820	2.5199

Table 3. Continued

Configuration 22

NPR	w_p/w_i	F_r/F_i	F_s/F_i	δ_p	δ_y	F_n/F_i	M_y/F_iL	F_z/F_i	M_z/F_iL
1.99	0.9776	0.8788	0.8787	0.80	-0.20	0.0123	-0.0239	-0.0031	0.0572
2.48	0.9770	0.9009	0.9009	0.59	0.02	0.0092	0.0172	0.0003	-0.0282
2.99	0.9782	0.9319	0.9318	0.36	0.04	0.0058	0.0364	0.0006	-0.0401
3.49	0.9781	0.9497	0.9497	0.21	0.02	0.0035	0.0352	0.0003	-0.0318
3.98	0.9782	0.9624	0.9624	0.15	-0.01	0.0024	0.0397	-0.0001	-0.0299
4.50	0.9781	0.9718	0.9718	0.14	0.07	0.0024	0.0324	0.0011	-0.0284
5.00	0.9780	0.9759	0.9759	0.13	0.07	0.0022	0.0350	0.0011	-0.0257
5.49	0.9778	0.9799	0.9798	0.17	0.09	0.0030	0.0274	0.0015	-0.0246
5.99	0.9770	0.9810	0.9810	0.17	0.14	0.0029	0.0293	0.0023	-0.0201
5.98	0.9771	0.9808	0.9808	0.14	0.14	0.0024	0.0302	0.0025	-0.0209

Configuration 23

NPR	w_p/w_i	F_r/F_i	F_s/F_i	δ_p	δ_y	F_n/F_i	M_y/F_iL	F_z/F_i	M_z/F_iL
2.00	0.9610	0.9206	0.9203	1.42	0.54	0.0228	-0.0901	0.0088	-0.1773
2.51	0.9635	0.9431	0.9411	3.78	0.09	0.0622	-0.7840	0.0015	-0.0267
2.99	0.9643	0.9562	0.9525	5.06	0.07	0.0844	-1.1788	0.0012	-0.0332
3.50	0.9649	0.9630	0.9575	6.14	0.03	0.1031	-1.4888	0.0006	-0.0285
4.00	0.9645	0.9666	0.9596	6.89	0.08	0.1160	-1.7051	0.0013	-0.0262
4.50	0.9654	0.9567	0.9453	8.83	-0.41	0.1468	-2.1766	-0.0068	0.0997
4.99	0.9667	0.9590	0.9476	8.87	0.01	0.1478	-2.1983	0.0002	0.0052
5.50	0.9686	0.9615	0.9502	8.78	0.10	0.1467	-2.1895	0.0017	-0.0010
5.99	0.9694	0.9619	0.9507	8.77	0.20	0.1467	-2.1882	0.0033	-0.0226

Configuration 24

NPR	w_p/w_i	F_r/F_i	F_s/F_i	δ_p	δ_y	F_n/F_i	M_y/F_iL	F_z/F_i	M_z/F_iL
2.00	0.9427	0.9651	0.9583	5.15	-4.41	0.0865	-1.1218	-0.0739	1.1219
2.51	0.9505	0.9708	0.9614	5.85	-5.49	0.0985	-1.3876	-0.0925	1.3947
3.01	0.9514	0.9697	0.9555	7.10	-6.84	0.1191	-1.7240	-0.1147	1.7327
3.50	0.9525	0.9669	0.9485	8.08	-7.88	0.1347	-1.9854	-0.1312	1.9880
3.99	0.9525	0.9628	0.9409	8.82	-8.61	0.1461	-2.1623	-0.1425	2.1649
4.51	0.9530	0.9383	0.9057	10.90	-10.77	0.1744	-2.6068	-0.1723	2.6329
5.01	0.9536	0.9403	0.9079	10.89	-10.67	0.1746	-2.6029	-0.1711	2.6133
5.50	0.9553	0.9407	0.9085	10.93	-10.59	0.1754	-2.6016	-0.1698	2.5916
6.01	0.9545	0.9407	0.9086	10.93	-10.53	0.1755	-2.5984	-0.1689	2.5929

Table 3. Continued

Configuration 25

NPR	w_p/w_i	F_r/F_i	F_a/F_i	δ_p	δ_y	F_n/F_i	$M_y/F_i L$	F_g/F_i	$M_z/F_i L$
2.01	0.9712	0.9290	0.9283	-1.20	-1.83	-0.0194	0.2796	-0.0297	0.3886
2.50	0.9704	0.9501	0.9500	-0.27	-0.63	-0.0045	0.0504	-0.0105	0.0908
3.01	0.9701	0.9678	0.9677	-0.05	-0.45	-0.0009	0.0167	-0.0076	0.0640
3.52	0.9692	0.9775	0.9775	-0.07	-0.26	-0.0012	0.0201	-0.0045	0.0333
4.02	0.9686	0.9816	0.9816	-0.06	-0.17	-0.0011	0.0170	-0.0029	0.0224
4.51	0.9677	0.9838	0.9838	-0.03	-0.10	-0.0005	0.0015	-0.0017	0.0094
5.02	0.9676	0.9847	0.9847	-0.08	-0.03	-0.0014	0.0056	-0.0005	-0.0067
5.51	0.9674	0.9842	0.9842	-0.10	-0.01	-0.0017	-0.0039	-0.0002	-0.0043
6.00	0.9676	0.9830	0.9830	-0.12	0.00	-0.0020	-0.0131	0.0000	-0.0011
7.01	0.9678	0.9803	0.9803	-0.11	0.00	-0.0019	-0.0205	0.0000	0.0009
7.99	0.9675	0.9777	0.9777	-0.06	0.00	-0.0011	-0.0228	0.0001	0.0035

Configuration 26

NPR	w_p/w_i	F_r/F_i	F_a/F_i	δ_p	δ_y	F_n/F_i	$M_y/F_i L$	F_g/F_i	$M_z/F_i L$
2.00	0.9238	0.9202	0.8667	19.63	-0.41	0.3092	-4.9288	-0.0063	-0.0054
2.50	0.9233	0.9418	0.8854	19.93	-0.05	0.3210	-5.0370	-0.0008	-0.0468
3.03	0.9241	0.9560	0.9125	17.35	0.07	0.2850	-4.3533	0.0011	-0.0789
3.50	0.9273	0.9638	0.9270	15.88	0.00	0.2637	-3.9475	0.0001	-0.0408
4.00	0.9279	0.9671	0.9347	14.86	0.20	0.2480	-3.6411	0.0033	-0.0880
4.50	0.9277	0.9693	0.9389	14.40	0.27	0.2410	-3.4769	0.0044	-0.1016
5.01	0.9273	0.9697	0.9396	14.30	0.26	0.2396	-3.4190	0.0043	-0.0893
5.52	0.9274	0.9699	0.9413	13.94	0.21	0.2337	-3.2950	0.0034	-0.0682
5.99	0.9271	0.9693	0.9421	13.61	0.20	0.2281	-3.1898	0.0032	-0.0634
7.01	0.9267	0.9664	0.9411	13.13	0.14	0.2195	-3.0219	0.0023	-0.0480
8.00	0.9264	0.9643	0.9404	12.80	0.12	0.2137	-2.8976	0.0020	-0.0465

Configuration 27

NPR	w_p/w_i	F_r/F_i	F_a/F_i	δ_p	δ_y	F_n/F_i	$M_y/F_i L$	F_g/F_i	$M_z/F_i L$
2.02	0.9721	0.9205	0.9194	2.29	-1.68	0.0367	-0.8108	-0.0270	0.2653
2.50	0.9724	0.9291	0.9278	3.07	0.32	0.0497	-0.7769	0.0052	-0.1241
3.00	0.9724	0.9266	0.9092	11.10	-0.78	0.1784	-2.7502	-0.0123	0.1683
3.51	0.9721	0.9470	0.9274	11.68	-0.34	0.1918	-3.0066	-0.0055	0.0657
4.01	0.9708	0.9595	0.9381	12.14	-0.17	0.2017	-3.1212	-0.0027	0.0296
4.50	0.9702	0.9636	0.9313	14.88	0.34	0.2475	-3.8255	0.0055	-0.0988
5.01	0.9696	0.9702	0.9393	14.50	0.15	0.2430	-3.7680	0.0025	-0.0481
5.50	0.9692	0.9738	0.9441	14.19	0.09	0.2387	-3.7104	0.0015	-0.0225
6.00	0.9689	0.9765	0.9478	13.93	0.11	0.2351	-3.6316	0.0018	-0.0300
7.00	0.9675	0.9801	0.9529	13.52	0.06	0.2291	-3.5057	0.0010	-0.0222
8.00	0.9667	0.9816	0.9555	13.24	0.05	0.2249	-3.4070	0.0009	-0.0234

Table 3. Continued

Configuration 28

NPR	w_p/w_i	F_r/F_i	F_s/F_i	δ_p	δ_y	F_n/F_i	M_y/F_iL	F_g/F_i	M_z/F_iL
2.02	0.9192	0.8909	0.8399	4.28	-19.06	0.0629	-0.9098	-0.2903	4.3979
2.51	0.9199	0.9125	0.8688	6.71	-16.63	0.1023	-1.4408	-0.2594	3.8597
3.02	0.9197	0.9240	0.8818	8.10	-15.57	0.1255	-1.7581	-0.2458	3.6116
3.50	0.9187	0.9302	0.8790	8.68	-17.25	0.1342	-1.8760	-0.2730	4.0989
4.01	0.9192	0.9377	0.8850	10.04	-16.83	0.1567	-2.2599	-0.2676	3.9972
4.51	0.9186	0.9406	0.8900	10.73	-15.88	0.1686	-2.4607	-0.2532	3.7269
5.02	0.9187	0.9406	0.8952	10.95	-14.48	0.1731	-2.5454	-0.2311	3.3295
5.50	0.9185	0.9433	0.9019	10.65	-13.60	0.1696	-2.4810	-0.2183	3.1014
6.00	0.9183	0.9454	0.9070	10.32	-12.99	0.1652	-2.3987	-0.2093	2.9249
6.50	0.9179	0.9478	0.9121	10.02	-12.45	0.1611	-2.3133	-0.2013	2.7710
7.00	0.9180	0.9496	0.9152	9.84	-12.16	0.1588	-2.2578	-0.1972	2.6759
8.00	0.9172	0.9520	0.9199	9.55	-11.67	0.1548	-2.1629	-0.1901	2.5230

Configuration 29

NPR	w_p/w_i	F_r/F_i	F_s/F_i	δ_p	δ_y	F_n/F_i	M_y/F_iL	F_g/F_i	M_z/F_iL
1.99	0.9600	0.9173	0.9141	4.66	1.33	0.0745	-1.4237	0.0212	-0.3696
2.51	0.9606	0.9189	0.8978	12.29	0.41	0.1957	-3.1893	0.0065	-0.1252
3.01	0.9607	0.9370	0.9062	14.68	1.33	0.2374	-3.8804	0.0210	-0.3726
3.50	0.9594	0.9505	0.9154	15.61	0.51	0.2558	-4.1530	0.0082	-0.1584
4.01	0.9591	0.9607	0.9223	16.25	-0.05	0.2688	-4.3320	-0.0008	0.0002
4.50	0.9581	0.9674	0.9310	15.76	0.06	0.2628	-4.2064	0.0009	-0.0234
5.01	0.9576	0.9728	0.9384	15.27	0.13	0.2562	-4.0645	0.0022	-0.0362
5.60	0.9575	0.9761	0.9436	14.81	0.18	0.2496	-3.9291	0.0030	-0.0500
6.00	0.9570	0.9773	0.9459	14.56	0.14	0.2457	-3.8540	0.0023	-0.0398
7.00	0.9588	0.9795	0.9501	14.09	0.13	0.2384	-3.7143	0.0021	-0.0329
8.01	0.9597	0.9801	0.9519	13.79	0.08	0.2335	-3.6086	0.0014	-0.0295

Configuration 30

NPR	w_p/w_i	F_r/F_i	F_s/F_i	δ_p	δ_y	F_n/F_i	M_y/F_iL	F_g/F_i	M_z/F_iL
2.01	0.9021	0.9079	0.8496	6.01	-19.89	0.0895	-1.5033	-0.3074	4.7218
2.50	0.9027	0.9150	0.8655	10.06	-16.36	0.1535	-2.4182	-0.2541	3.7824
3.02	0.9030	0.9226	0.8636	10.93	-17.87	0.1667	-2.5813	-0.2784	4.2127
3.51	0.9018	0.9280	0.8716	11.07	-17.16	0.1705	-2.6100	-0.2691	4.0403
4.01	0.9015	0.9346	0.8814	11.26	-16.22	0.1755	-2.6688	-0.2564	3.7995
4.51	0.9011	0.9389	0.8895	11.06	-15.40	0.1738	-2.6255	-0.2450	3.5903
5.02	0.9007	0.9395	0.8945	10.90	-14.42	0.1723	-2.5933	-0.2300	3.3108
5.50	0.9005	0.9417	0.8993	10.86	-13.73	0.1725	-2.5857	-0.2198	3.1106
6.00	0.9002	0.9420	0.9024	10.69	-13.08	0.1703	-2.5498	-0.2097	2.9251
7.00	0.8996	0.9423	0.9066	10.46	-12.16	0.1674	-2.4787	-0.1953	2.6365
8.00	0.8988	0.9433	0.9098	10.22	-11.65	0.1641	-2.4043	-0.1875	2.4749

Table 3. Continued

Configuration 31

NPR	w_p/w_i	F_r/F_i	F_a/F_i	δ_p	δ_y	F_n/F_i	M_y/F_iL	F_s/F_i	M_z/F_iL
2.00	0.9793	0.9417	0.9416	0.70	0.36	0.0114	0.0472	0.0060	-0.1400
2.52	0.9814	0.9660	0.9660	0.56	0.09	0.0095	-0.0234	0.0016	-0.0668
2.98	0.9825	0.9781	0.9781	0.40	-0.01	0.0069	-0.0195	-0.0002	-0.0424
3.49	0.9835	0.9860	0.9860	0.30	-0.03	0.0052	-0.0140	-0.0005	-0.0378
3.99	0.9835	0.9889	0.9888	0.29	-0.04	0.0051	-0.0139	-0.0006	-0.0258
4.52	0.9828	0.9894	0.9894	0.24	-0.06	0.0042	-0.0095	-0.0010	-0.0211
4.99	0.9828	0.9884	0.9884	0.22	-0.01	0.0038	-0.0100	-0.0001	-0.0138
5.50	0.9822	0.9866	0.9866	0.21	0.02	0.0036	-0.0113	0.0003	-0.0137
6.02	0.9809	0.9850	0.9850	0.22	0.05	0.0038	-0.0124	0.0008	-0.0110

Configuration 32

NPR	w_p/w_i	F_r/F_i	F_a/F_i	δ_p	δ_y	F_n/F_i	M_y/F_iL	F_s/F_i	M_z/F_iL
2.01	0.9554	0.9552	0.9478	7.11	-0.06	0.1183	-1.7383	-0.0010	-0.0195
2.50	0.9561	0.9467	0.9189	13.90	-0.09	0.2274	-3.4237	-0.0015	-0.0311
3.00	0.9563	0.9536	0.9224	14.68	-0.18	0.2417	-3.7231	-0.0030	0.0143
3.50	0.9562	0.9618	0.9325	14.18	0.00	0.2357	-3.5951	0.0001	-0.0247
4.01	0.9562	0.9663	0.9391	13.62	0.00	0.2275	-3.4069	0.0001	-0.0288
4.50	0.9559	0.9678	0.9426	13.10	0.10	0.2194	-3.2631	0.0016	-0.0335
5.00	0.9553	0.9680	0.9441	12.76	0.13	0.2137	-3.1423	0.0022	-0.0322
5.50	0.9549	0.9671	0.9440	12.53	0.14	0.2098	-3.0424	0.0023	-0.0246
5.99	0.9540	0.9657	0.9436	12.27	0.18	0.2053	-2.9733	0.0030	-0.0239

Configuration 33

NPR	w_p/w_i	F_r/F_i	F_a/F_i	δ_p	δ_y	F_n/F_i	M_y/F_iL	F_s/F_i	M_z/F_iL
2.01	0.8935	0.9176	0.8597	15.08	-14.49	0.2316	-3.3716	-0.2221	3.3198
2.50	0.8965	0.9397	0.8854	14.26	-13.96	0.2250	-3.2030	-0.2201	3.2345
2.99	0.8991	0.9518	0.8859	15.60	-15.44	0.2474	-3.5831	-0.2446	3.6146
3.50	0.8997	0.9517	0.8878	15.29	-15.26	0.2427	-3.5175	-0.2422	3.5605
4.00	0.9003	0.9507	0.8948	14.24	-14.25	0.2270	-3.2222	-0.2272	3.2681
4.50	0.9002	0.9515	0.9016	13.40	-13.45	0.2148	-3.0064	-0.2156	3.0554
5.00	0.8997	0.9523	0.9059	12.90	-12.91	0.2075	-2.8712	-0.2077	2.9183
5.51	0.8993	0.9512	0.9078	12.52	-12.44	0.2016	-2.7670	-0.2002	2.8002
6.00	0.8986	0.9508	0.9093	12.28	-12.10	0.1980	-2.6948	-0.1949	2.7221

Table 3. Continued

Configuration 34

NPR	w_p/w_i	F_r/F_i	F_a/F_i	δ_p	δ_y	F_n/F_i	M_y/F_iL	F_z/F_i	M_z/F_iL
2.00	0.9755	0.9080	0.9039	0.01	-5.40	0.0002	-0.0085	-0.0854	1.2839
3.00	0.9750	0.9521	0.9521	0.19	-0.36	0.0031	-0.0275	-0.0059	0.0416
2.49	0.9735	0.9334	0.9334	0.11	-0.43	0.0018	-0.0210	-0.0070	0.0433
3.51	0.9733	0.9631	0.9631	0.25	-0.21	0.0043	-0.0464	-0.0036	0.0125
4.02	0.9725	0.9721	0.9721	0.25	-0.17	0.0043	-0.0495	-0.0028	0.0146
4.51	0.9720	0.9784	0.9784	0.22	-0.15	0.0038	-0.0434	-0.0026	0.0150
5.00	0.9715	0.9819	0.9819	0.18	-0.12	0.0031	-0.0386	-0.0020	0.0138
5.51	0.9713	0.9838	0.9838	0.13	-0.09	0.0022	-0.0363	-0.0016	0.0153
6.02	0.9710	0.9850	0.9850	0.09	-0.09	0.0016	-0.0392	-0.0016	0.0165
7.01	0.9708	0.9849	0.9849	0.06	-0.09	0.0010	-0.0453	-0.0016	0.0188
7.99	0.9704	0.9848	0.9848	0.08	-0.11	0.0014	-0.0457	-0.0019	0.0247

Configuration 35

NPR	w_p/w_i	F_r/F_i	F_a/F_i	δ_p	δ_y	F_n/F_i	M_y/F_iL	F_z/F_i	M_z/F_iL
2.01	0.9441	0.9276	0.9186	7.97	0.01	0.1287	-2.1205	0.0002	-0.0741
2.52	0.9466	0.9476	0.9332	10.00	-0.21	0.1645	-2.6029	-0.0035	-0.0150
3.00	0.9456	0.9383	0.8988	16.67	-0.60	0.2691	-4.1126	-0.0094	0.1201
3.51	0.9449	0.9511	0.9123	16.41	-0.08	0.2687	-4.1037	-0.0012	-0.0112
4.03	0.9454	0.9571	0.9185	16.32	0.01	0.2689	-4.0627	0.0002	-0.0228
4.51	0.9443	0.9604	0.9188	16.93	-0.01	0.2796	-4.1942	-0.0002	-0.0078
5.01	0.9441	0.9636	0.9247	16.34	-0.06	0.2711	-4.0342	-0.0009	0.0001
5.50	0.9440	0.9661	0.9289	15.94	-0.04	0.2653	-3.9113	-0.0006	-0.0004
6.00	0.9438	0.9679	0.9324	15.56	0.04	0.2596	-3.8072	0.0006	-0.0086
7.01	0.9429	0.9694	0.9363	15.03	0.07	0.2513	-3.6400	0.0012	-0.0209
8.00	0.9421	0.9698	0.9382	14.66	0.05	0.2455	-3.5141	0.0009	-0.0200

Configuration 36

NPR	w_p/w_i	F_r/F_i	F_a/F_i	δ_p	δ_y	F_n/F_i	M_y/F_iL	F_z/F_i	M_z/F_iL
2.00	0.9701	0.9613	0.9612	-0.15	-0.48	-0.0025	-0.1055	-0.0080	-0.0128
2.49	0.9713	0.9676	0.9672	-1.62	-0.17	-0.0273	0.4420	-0.0028	-0.0526
3.00	0.9715	0.9659	0.9659	0.48	-0.25	0.0081	-0.0178	-0.0043	-0.0146
3.50	0.9710	0.9572	0.9517	6.09	-0.57	0.1016	-1.5246	-0.0095	0.1139
4.01	0.9699	0.9471	0.9279	11.55	-0.13	0.1897	-2.8988	-0.0021	0.0021
4.51	0.9696	0.9576	0.9364	12.07	-0.08	0.2003	-3.0740	-0.0012	0.0042
4.99	0.9691	0.9643	0.9413	12.53	-0.05	0.2093	-3.1944	-0.0009	0.0021
5.50	0.9686	0.9673	0.9412	13.32	-0.04	0.2229	-3.4094	-0.0007	0.0085
6.00	0.9684	0.9681	0.9383	14.26	0.06	0.2385	-3.6953	0.0009	-0.0130
7.00	0.9675	0.9750	0.9457	14.10	0.01	0.2375	-3.6478	0.0002	-0.0030
8.00	0.9672	0.9784	0.9500	13.83	-0.03	0.2339	-3.5660	-0.0004	-0.0011

Table 3. Continued

Configuration 37

NPR	w_p/w_i	F_r/F_i	F_a/F_i	δ_p	δ_y	F_n/F_i	M_y/F_iL	F_g/F_i	M_z/F_iL
2.02	0.9324	0.8829	0.8418	9.62	-14.94	0.1426	-2.3182	-0.2247	3.4599
2.51	0.9326	0.9162	0.8819	8.62	-13.33	0.1337	-2.0965	-0.2089	3.1778
3.01	0.9313	0.9178	0.8660	9.92	-16.92	0.1514	-2.2639	-0.2634	3.9540
3.51	0.9307	0.9269	0.8677	12.29	-17.02	0.1891	-2.8322	-0.2656	3.9663
4.00	0.9308	0.9370	0.8699	11.98	-18.74	0.1846	-2.7078	-0.2952	4.4714
4.52	0.9299	0.9452	0.8766	12.52	-18.60	0.1946	-2.8637	-0.2950	4.4737
5.00	0.9307	0.9398	0.8753	13.33	-17.27	0.2074	-3.1105	-0.2722	4.0579
5.50	0.9302	0.9404	0.8816	13.08	-16.15	0.2048	-3.0576	-0.2554	3.7474
6.02	0.9302	0.9440	0.8905	12.54	-15.25	0.1981	-2.9299	-0.2428	3.5133
7.01	0.9289	0.9505	0.9027	11.96	-14.18	0.1912	-2.7847	-0.2281	3.2264
8.01	0.9281	0.9545	0.9098	11.55	-13.65	0.1860	-2.6828	-0.2209	3.0704

Configuration 38

NPR	w_p/w_i	F_r/F_i	F_a/F_i	δ_p	δ_y	F_n/F_i	M_y/F_iL	F_g/F_i	M_z/F_iL
1.99	0.9658	0.9070	0.9038	4.04	-2.53	0.0639	-1.4167	-0.0400	0.4422
2.51	0.9671	0.9364	0.9346	3.04	-1.80	0.0497	-0.9490	-0.0294	0.4000
3.00	0.9663	0.9397	0.9300	8.20	-0.82	0.1340	-2.2284	-0.0134	0.1655
3.51	0.9654	0.9372	0.9104	13.74	-0.25	0.2226	-3.6060	-0.0040	0.0372
4.01	0.9651	0.9513	0.9233	13.94	-0.05	0.2292	-3.6856	-0.0008	-0.0083
4.50	0.9644	0.9604	0.9313	14.16	0.02	0.2349	-3.7313	0.0003	-0.0164
5.02	0.9645	0.9660	0.9349	14.59	-0.12	0.2433	-3.8557	-0.0019	0.0295
5.51	0.9642	0.9686	0.9348	15.19	0.05	0.2538	-4.0225	0.0008	-0.0112
6.01	0.9640	0.9710	0.9369	15.24	0.08	0.2553	-4.0371	0.0013	-0.0181
7.00	0.9630	0.9753	0.9416	15.10	0.07	0.2540	-3.9949	0.0011	-0.0144
8.01	0.9622	0.9781	0.9459	14.75	0.07	0.2491	-3.8802	0.0012	-0.0249

Configuration 39

NPR	w_p/w_i	F_r/F_i	F_a/F_i	δ_p	δ_y	F_n/F_i	M_y/F_iL	F_g/F_i	M_z/F_iL
1.99	0.9214	0.9001	0.8546	8.15	-16.58	0.1223	-2.1700	-0.2544	3.9912
2.50	0.9219	0.9116	0.8624	11.15	-15.66	0.1699	-2.7820	-0.2418	3.7449
2.99	0.9199	0.9143	0.8519	14.55	-16.22	0.2211	-3.5190	-0.2478	3.7315
3.50	0.9196	0.9246	0.8574	14.61	-17.15	0.2234	-3.4904	-0.2646	3.9697
4.00	0.9198	0.9279	0.8516	14.47	-19.16	0.2198	-3.3746	-0.2959	4.5160
4.49	0.9200	0.9334	0.8604	14.17	-18.60	0.2172	-3.3221	-0.2895	4.4046
5.01	0.9204	0.9327	0.8646	14.50	-17.30	0.2236	-3.4339	-0.2694	4.0331
5.50	0.9197	0.9351	0.8711	14.47	-16.31	0.2248	-3.4456	-0.2549	3.7490
6.00	0.9200	0.9361	0.8766	14.07	-15.54	0.2198	-3.3590	-0.2438	3.5468
7.01	0.9187	0.9420	0.8890	13.26	-14.53	0.2094	-3.1606	-0.2304	3.2801
7.99	0.9177	0.9455	0.8962	12.77	-13.95	0.2032	-3.0394	-0.2226	3.1109

Table 3. Continued

Configuration 40

NPR	w_p/w_i	F_r/F_i	F_a/F_i	δ_p	δ_y	F_n/F_i	M_y/F_iL	F_g/F_i	M_z/F_iL
2.00	0.9765	0.8994	0.8993	0.48	-0.19	0.0076	0.0776	-0.0029	-0.0204
2.50	0.9779	0.9203	0.9202	0.37	-0.11	0.0059	0.0533	-0.0017	-0.0263
2.99	0.9813	0.9461	0.9461	0.32	0.03	0.0052	0.0209	0.0005	-0.0643
3.50	0.9821	0.9632	0.9632	0.27	0.01	0.0046	-0.0007	0.0002	-0.0596
4.02	0.9822	0.9743	0.9743	0.27	0.05	0.0046	-0.0119	0.0009	-0.0569
4.51	0.9817	0.9810	0.9810	0.26	0.08	0.0044	-0.0060	0.0013	-0.0551
4.99	0.9815	0.9840	0.9839	0.26	0.05	0.0044	-0.0080	0.0009	-0.0454
5.51	0.9813	0.9870	0.9870	0.24	0.09	0.0041	-0.0088	0.0015	-0.0372
6.01	0.9803	0.9885	0.9885	0.27	0.11	0.0046	-0.0064	0.0019	-0.0324

Configuration 41

NPR	w_p/w_i	F_r/F_i	F_a/F_i	δ_p	δ_y	F_n/F_i	M_y/F_iL	F_g/F_i	M_z/F_iL
2.01	0.9628	0.9528	0.9528	0.16	0.13	0.0027	0.2629	0.0022	-0.0608
2.50	0.9639	0.9618	0.9605	2.93	0.03	0.0492	-0.5373	0.0004	-0.0358
3.00	0.9643	0.9684	0.9639	5.49	-0.01	0.0927	-1.2861	-0.0002	-0.0292
3.51	0.9654	0.9558	0.9423	9.64	-0.43	0.1601	-2.3606	-0.0071	0.0936
3.99	0.9657	0.9612	0.9465	10.04	0.14	0.1676	-2.4801	0.0023	-0.0515
4.51	0.9653	0.9594	0.9409	11.26	0.12	0.1873	-2.8074	0.0020	-0.0390
5.03	0.9652	0.9606	0.9418	11.34	0.14	0.1889	-2.8288	0.0023	-0.0206
5.50	0.9642	0.9627	0.9443	11.23	0.15	0.1876	-2.7850	0.0024	-0.0134
6.00	0.9633	0.9645	0.9466	11.04	0.18	0.1846	-2.7370	0.0030	-0.0101

Configuration 42

NPR	w_p/w_i	F_r/F_i	F_a/F_i	δ_p	δ_y	F_n/F_i	M_y/F_iL	F_g/F_i	M_z/F_iL
2.00	0.9298	0.9434	0.9229	8.80	-8.27	0.1429	-2.1377	-0.1341	2.0186
2.49	0.9399	0.9441	0.9126	10.92	-10.30	0.1760	-2.6351	-0.1658	2.5231
3.00	0.9405	0.9269	0.8465	17.51	-17.49	0.2671	-4.0588	-0.2668	4.1315
3.49	0.9415	0.9280	0.8450	17.84	-17.77	0.2720	-4.1333	-0.2707	4.1784
4.00	0.9419	0.9364	0.8649	16.40	-16.29	0.2546	-3.8054	-0.2528	3.8478
4.52	0.9424	0.9423	0.8783	15.41	-15.32	0.2421	-3.5670	-0.2406	3.6099
5.00	0.9430	0.9457	0.8860	14.84	-14.73	0.2347	-3.4324	-0.2329	3.4764
5.51	0.9424	0.9468	0.8910	14.35	-14.16	0.2280	-3.3121	-0.2248	3.3551
6.00	0.9417	0.9486	0.8956	13.98	-13.75	0.2229	-3.2258	-0.2192	3.2701

Table 3. Continued

Configuration 43

NPR	w_p/w_i	F_r/F_i	F_a/F_i	δ_p	δ_y	F_n/F_i	M_y/F_iL	F_s/F_i	M_z/F_iL
2.00	0.8265	0.9556	0.1658	80.01	-3.86	0.9410	-11.2823	-0.0112	0.0350
2.52	0.8481	0.9643	0.1358	81.90	-4.03	0.9547	-11.4674	-0.0096	0.0492
3.03	0.8564	0.9644	0.1168	83.05	-4.26	0.9573	-11.5385	-0.0087	0.0559
3.51	0.8594	0.9639	0.1037	83.83	-4.00	0.9583	-11.5653	-0.0073	0.0491
4.00	0.8613	0.9621	0.0945	84.36	-4.42	0.9575	-11.5493	-0.0073	0.0488
4.49	0.8608	0.9605	0.0862	84.85	-4.13	0.9566	-11.5446	-0.0062	0.0451
5.01	0.8627	0.9552	0.0799	85.20	-4.13	0.9518	-11.4804	-0.0058	0.0557
5.53	0.8635	0.9542	0.0766	85.39	-4.61	0.9511	-11.4138	-0.0062	0.0648
6.61	0.8645	0.9555	0.0727	85.64	-4.44	0.9527	-11.2120	-0.0056	0.0696
6.03	0.8656	0.9552	0.0766	85.40	-4.35	0.9521	-11.2885	-0.0058	0.0683

Configuration 44

NPR	w_p/w_i	F_r/F_i	F_a/F_i	δ_p	δ_y	F_n/F_i	M_y/F_iL	F_s/F_i	M_z/F_iL
2.01	0.7958	0.9703	0.1434	81.50	-3.05	0.9596	-12.0191	-0.0076	0.0002
2.50	0.8253	0.9742	0.1101	83.51	-2.60	0.9679	-12.0714	-0.0050	0.0169
3.01	0.8373	0.9726	0.0875	84.84	-3.46	0.9687	-12.1303	-0.0053	0.0211
3.52	0.8426	0.9709	0.0736	85.65	-3.60	0.9681	-12.1303	-0.0046	0.0185
4.02	0.8452	0.9683	0.0640	86.21	-4.12	0.9662	-12.1015	-0.0046	0.0239
4.51	0.8467	0.9655	0.0577	86.57	-3.94	0.9637	-12.0690	-0.0040	0.0292
5.01	0.8477	0.9631	0.0523	86.89	-4.61	0.9617	-12.0242	-0.0042	0.0374
5.51	0.8481	0.9604	0.0486	87.10	-5.08	0.9592	-11.9820	-0.0043	0.0450
6.01	0.8482	0.9625	0.0464	87.24	-4.66	0.9614	-11.8956	-0.0038	0.0486

Configuration 45

NPR	w_p/w_i	F_r/F_i	F_a/F_i	δ_p	δ_y	F_n/F_i	M_y/F_iL	F_s/F_i	M_z/F_iL
2.01	0.7280	0.3598	-0.3597	-179.99	179.46	-0.0001	-0.0062	0.0034	-0.1970
2.52	0.7694	0.3924	-0.3924	-179.85	-179.95	-0.0011	0.0347	-0.0003	-0.0935
3.02	0.7876	0.4213	-0.4213	179.71	-179.88	0.0021	0.0336	-0.0008	-0.0556
3.53	0.7974	0.4386	-0.4385	179.26	-179.96	0.0057	-0.0094	-0.0003	-0.0442
4.02	0.8040	0.4509	-0.4509	179.35	-179.24	0.0051	0.0219	-0.0059	0.0330
4.51	0.8105	0.4537	-0.4536	179.20	-179.83	0.0063	-0.0042	-0.0013	-0.0013
5.04	0.8165	0.4571	-0.4571	179.20	-179.75	0.0064	-0.0004	-0.0020	0.0222
5.52	0.8213	0.4584	-0.4584	179.28	-179.71	0.0058	0.0063	-0.0024	0.0384
6.03	0.8257	0.4576	-0.4575	179.44	-179.67	0.0045	0.0118	-0.0027	0.0538

Table 3. Continued

Configuration 46

NPR	w_p/w_i	F_r/F_i	F_s/F_i	δ_p	δ_y	F_n/F_i	M_y/F_iL	F_z/F_i	M_z/F_iL
2.01	0.7229	0.5065	-0.5065	-179.91	-179.55	-0.0008	0.0082	-0.0040	-0.0432
2.51	0.7576	0.5543	-0.5543	179.97	179.93	0.0003	0.0171	0.0007	-0.0509
3.02	0.7766	0.5869	-0.5869	179.85	-179.98	0.0015	0.0253	-0.0002	-0.0193
3.50	0.7856	0.6052	-0.6052	179.80	-179.72	0.0021	0.0257	-0.0030	0.0239
4.00	0.7916	0.6156	-0.6156	179.76	-179.48	0.0025	0.0226	-0.0056	0.0674
4.51	0.7956	0.6201	-0.6201	179.75	-179.32	0.0027	0.0252	-0.0074	0.1088
4.99	0.7978	0.6222	-0.6221	179.74	-178.97	0.0028	0.0450	-0.0111	0.1623
5.50	0.8003	0.6208	-0.6207	179.74	-178.79	0.0028	0.0461	-0.0131	0.2024
6.00	0.8025	0.6180	-0.6179	179.83	-178.72	0.0018	0.0565	-0.0138	0.2246

Configuration 47

NPR	w_p/w_i	F_r/F_i	F_s/F_i	δ_p	δ_y	F_n/F_i	M_y/F_iL	F_z/F_i	M_z/F_iL
2.00	0.8625	0.0771	0.0771	0.08	-1.99	0.0001	0.0043	-0.0027	-0.0388
2.51	0.8990	0.0613	0.0612	2.33	-2.50	0.0025	-0.0076	-0.0027	-0.0228
3.02	0.9126	0.0521	0.0519	4.85	1.77	0.0044	-0.0170	0.0016	-0.0417
3.50	0.9189	0.0443	0.0440	6.16	1.33	0.0048	-0.0178	0.0010	-0.0380
4.01	0.9218	0.0378	0.0374	7.54	3.27	0.0050	-0.0180	0.0021	-0.0336
4.52	0.9242	0.0335	0.0331	7.43	4.23	0.0043	-0.0180	0.0024	-0.0321
5.00	0.9254	0.0292	0.0290	5.76	0.37	0.0029	-0.0131	0.0002	-0.0039
5.51	0.9262	0.0282	0.0279	7.48	3.02	0.0037	-0.0209	0.0015	-0.0075
6.01	0.9268	0.0260	0.0256	8.50	5.50	0.0038	-0.0349	0.0025	-0.0129

Configuration 48

NPR	w_p/w_i	F_r/F_i	F_s/F_i	δ_p	δ_y	F_n/F_i	M_y/F_iL	F_z/F_i	M_z/F_iL
2.01	0.8300	0.0216	0.0179	-5.14	-33.88	-0.0016	-0.0026	-0.0120	0.0856
2.50	0.8660	0.0115	-0.0005	134.15	-92.39	0.0005	-0.0087	-0.0115	0.1009
3.01	0.8827	0.0196	-0.0166	172.99	-148.32	0.0020	-0.0035	-0.0102	0.1014
3.52	0.8908	0.0298	-0.0280	173.00	-161.45	0.0034	-0.0199	-0.0094	0.1048
4.00	0.8955	0.0372	-0.0362	175.82	-167.35	0.0026	-0.0015	-0.0081	0.0986
4.50	0.8992	0.0427	-0.0419	176.38	-169.56	0.0027	0.0023	-0.0077	0.1063
5.00	0.9012	0.0465	-0.0460	177.83	-172.52	0.0017	0.0058	-0.0060	0.0941
5.52	0.9027	0.0496	-0.0492	177.70	-173.15	0.0020	0.0026	-0.0059	0.0997
6.02	0.9032	0.0503	-0.0499	177.63	-173.80	0.0021	-0.0033	-0.0054	0.1049

Table 3. Continued

Configuration 49

NPR	w_p/w_i	F_r/F_i	F_a/F_i	δ_p	δ_y	F_n/F_i	M_y/F_iL	F_s/F_i	M_z/F_iL
2.01	0.8197	0.9497	0.1070	83.53	-2.39	0.9436	-11.5370	-0.0045	-0.0219
2.51	0.8442	0.9605	0.0755	85.49	-2.92	0.9575	-11.6703	-0.0039	-0.0123
3.02	0.8525	0.9630	0.0420	87.50	-3.69	0.9621	-11.8073	-0.0027	-0.0072
3.50	0.8562	0.9627	0.0178	88.94	-8.04	0.9626	-11.8815	-0.0025	-0.0086
4.00	0.8583	0.9620	-0.0005	90.03	-107.33	0.9620	-11.9087	-0.0016	-0.0067
4.50	0.8596	0.9607	-0.0150	90.90	-179.07	0.9606	-11.9162	-0.0002	-0.0142
5.02	0.8605	0.9591	-0.0253	91.51	-178.09	0.9588	-11.9033	-0.0008	-0.0043
5.51	0.8609	0.9583	-0.0303	91.81	-179.53	0.9579	-11.8555	-0.0002	-0.0008
6.00	0.8613	0.9613	-0.0350	92.09	179.48	0.9607	-11.7702	0.0003	0.0047

Configuration 50

NPR	w_p/w_i	F_r/F_i	F_a/F_i	δ_p	δ_y	F_n/F_i	M_y/F_iL	F_s/F_i	M_z/F_iL
2.02	0.7873	0.9634	0.0133	89.21	-26.28	0.9633	-12.4011	-0.0066	0.0124
2.50	0.8200	0.9690	-0.0238	91.41	-163.73	0.9687	-12.4820	-0.0069	0.0287
3.00	0.8344	0.9692	-0.0529	93.13	-173.38	0.9677	-12.5577	-0.0061	0.0360
3.52	0.8420	0.9693	-0.0750	94.44	-175.76	0.9664	-12.5899	-0.0056	0.0393
4.00	0.8449	0.9715	-0.0907	95.36	-176.53	0.9672	-12.6054	-0.0055	0.0455
4.50	0.8477	0.9699	-0.1032	96.11	-177.12	0.9643	-12.5976	-0.0052	0.0397
5.02	0.8490	0.9698	-0.1122	96.64	-177.78	0.9633	-12.5829	-0.0043	0.0421
5.50	0.8496	0.9711	-0.1175	96.95	-178.28	0.9639	-12.5338	-0.0035	0.0458
6.00	0.8497	0.9760	-0.1226	97.22	-178.44	0.9682	-12.4565	-0.0033	0.0464

Configuration 51

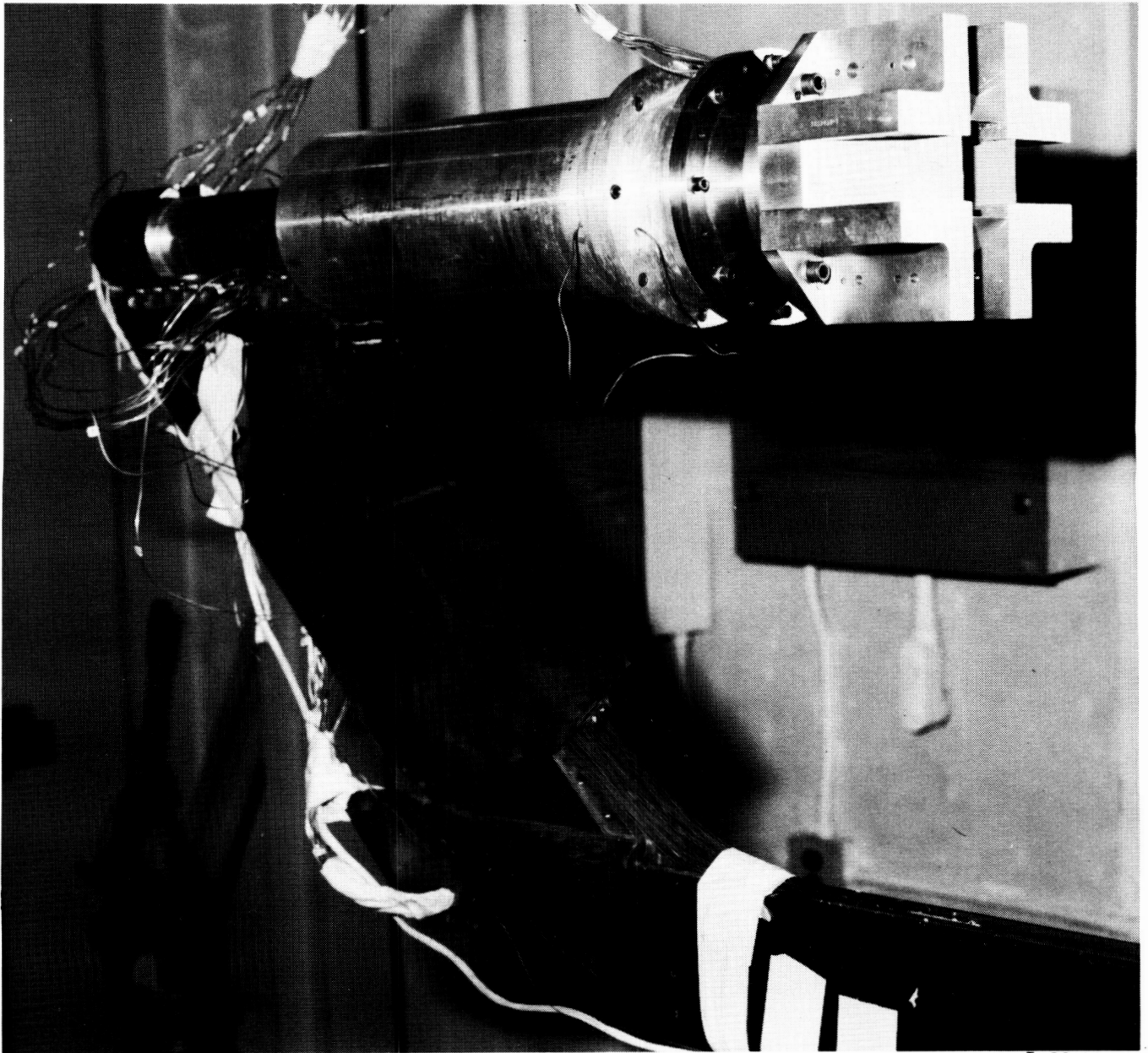
NPR	w_p/w_i	F_r/F_i	F_a/F_i	δ_p	δ_y	F_n/F_i	M_y/F_iL	F_s/F_i	M_z/F_iL
2.00	0.7444	0.2308	-0.2303	179.40	-176.39	0.0024	0.0437	-0.0145	0.0096
2.51	0.7795	0.2647	-0.2645	179.14	-177.74	0.0040	0.0399	-0.0104	0.0082
3.02	0.7967	0.2861	-0.2860	179.11	-178.71	0.0045	0.0468	-0.0064	0.0005
3.50	0.8044	0.2981	-0.2981	178.90	-179.25	0.0057	0.0334	-0.0039	-0.0061
4.00	0.8101	0.3039	-0.3039	179.05	-179.59	0.0050	0.0303	-0.0022	-0.0133
4.50	0.8133	0.3064	-0.3064	179.06	179.87	0.0050	0.0230	0.0007	-0.0247
5.01	0.8159	0.3088	-0.3088	179.23	179.65	0.0041	0.0220	0.0019	-0.0279
5.49	0.8171	0.3099	-0.3099	179.24	179.48	0.0041	0.0209	0.0028	-0.0254
6.00	0.8189	0.3097	-0.3097	179.39	179.21	0.0033	0.0168	0.0043	-0.0336

Table 3. Concluded

Configuration 52

NPR	w_p/w_i	F_r/F_i	F_a/F_i	δ_p	δ_y	F_n/F_i	M_y/F_iL	F_z/F_i	M_z/F_iL
2.02	0.7213	0.4298	-0.4297	-179.83	-178.71	-0.0013	0.0113	-0.0097	-0.0047
2.51	0.7573	0.4672	-0.4671	179.89	-179.10	0.0009	0.0121	-0.0073	0.0133
3.01	0.7800	0.4818	-0.4818	179.83	-179.64	0.0015	0.0311	-0.0031	0.0044
3.51	0.7904	0.4818	-0.4818	179.72	-179.57	0.0023	0.0383	-0.0036	0.0196
4.01	0.7978	0.4782	-0.4782	179.78	-179.52	0.0019	0.0462	-0.0040	0.0349
4.50	0.8036	0.4737	-0.4736	179.57	-179.63	0.0035	0.0334	-0.0030	0.0352
5.01	0.8076	0.4676	-0.4675	179.50	-179.90	0.0041	0.0311	-0.0008	0.0244
5.51	0.8100	0.4621	-0.4621	179.53	179.95	0.0038	0.0313	0.0004	0.0179
6.01	0.8135	0.4553	-0.4553	179.65	179.82	0.0028	0.0387	0.0014	0.0157

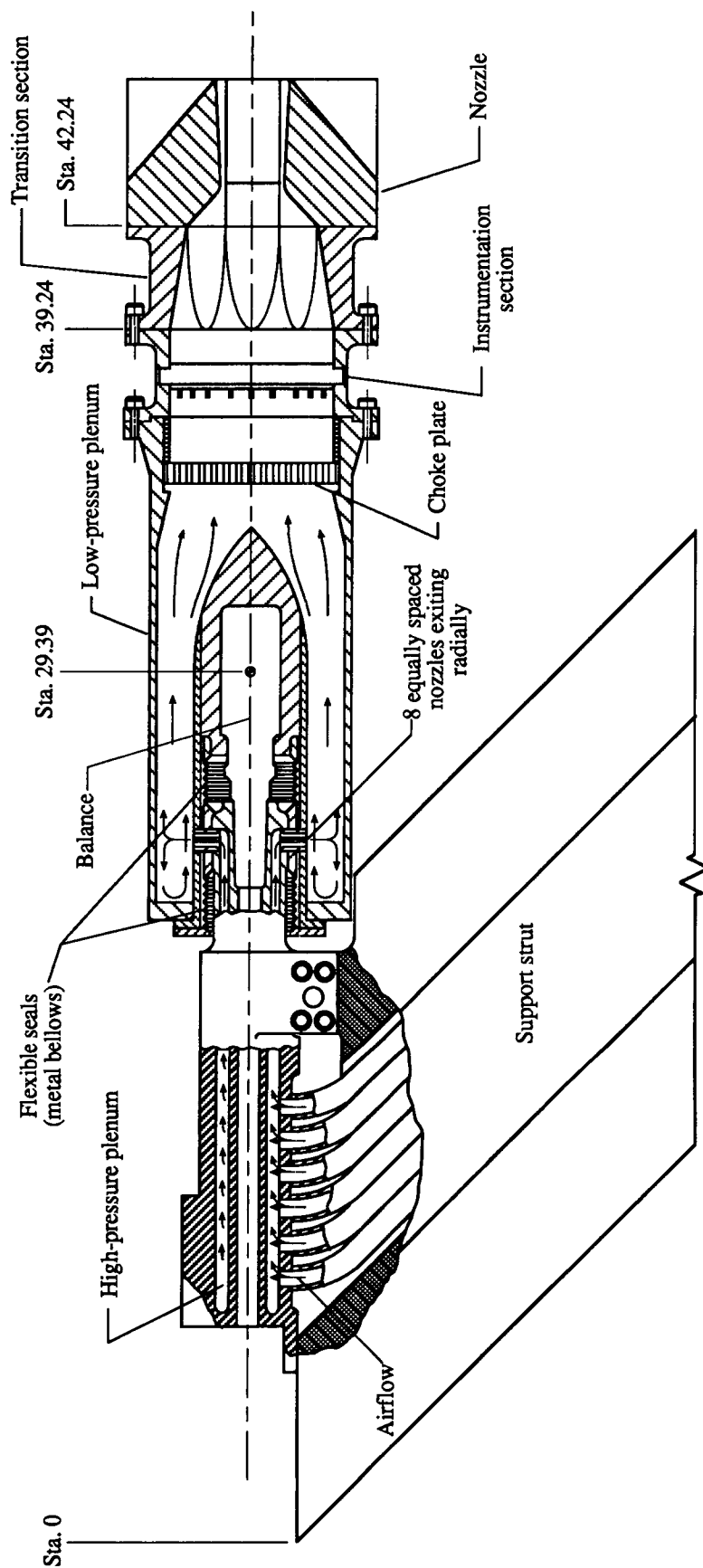
ORIGINAL PAGE
BLACK AND WHITE PHOTOGRAPH



L-89-12938

(a) Propulsion simulation system with a typical cruciform nozzle configuration installed.

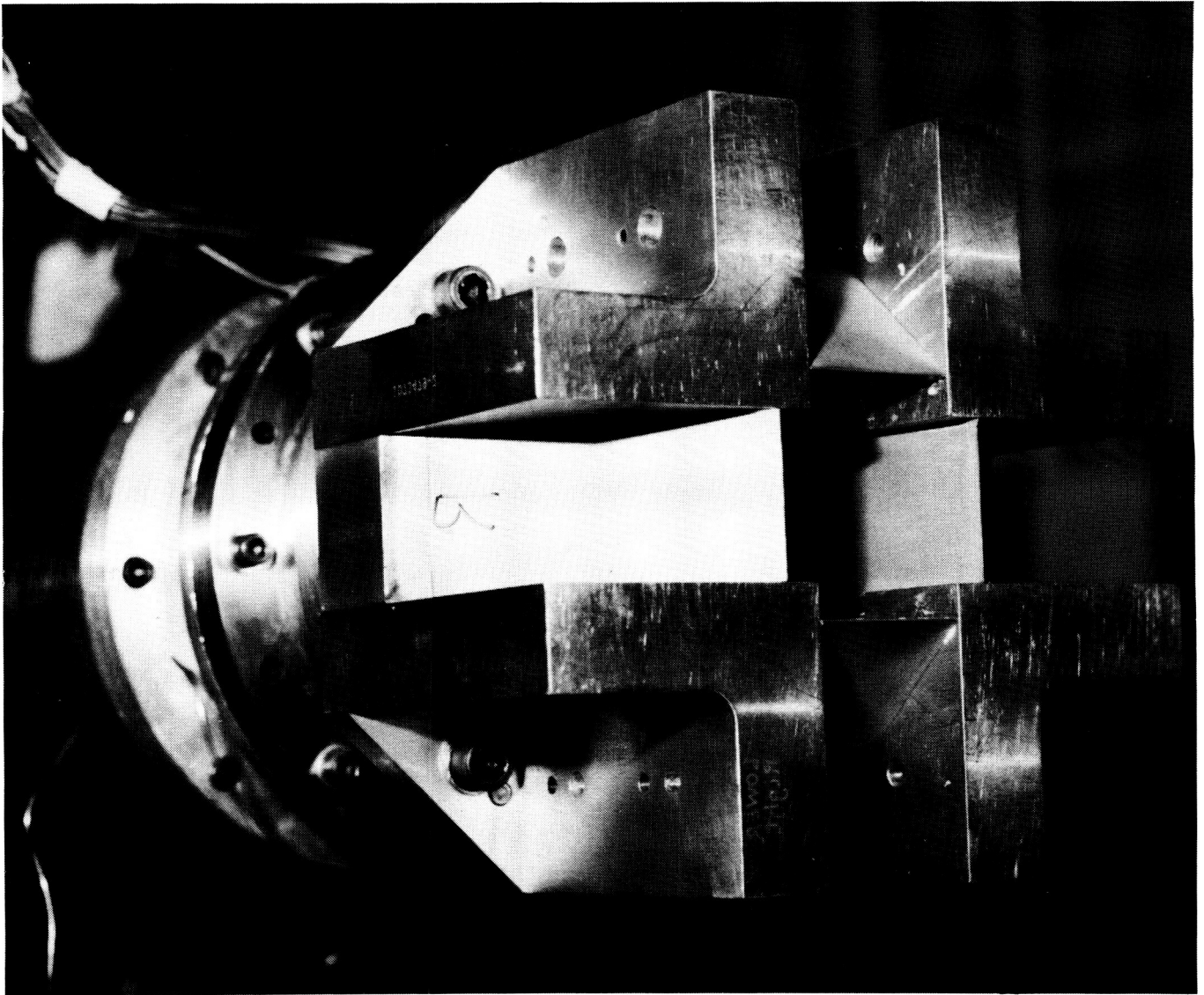
Figure 1. Single-engine propulsion simulation system.



(b) Propulsion simulation system. Station numbers are in inches.

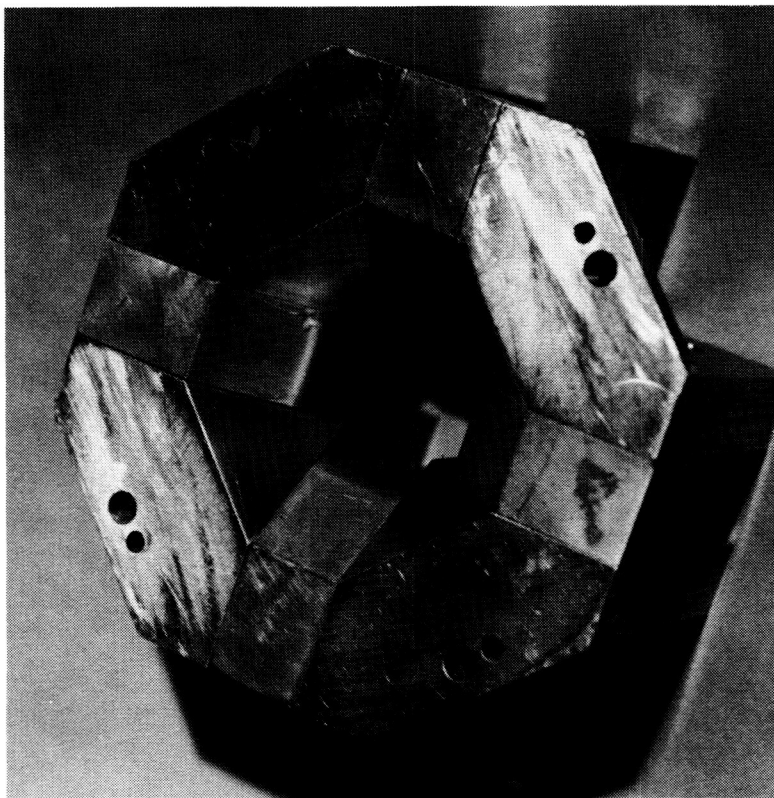
Figure 1. Concluded.

ORIGINAL PAGE
BLACK AND WHITE PHOTOGRAPH



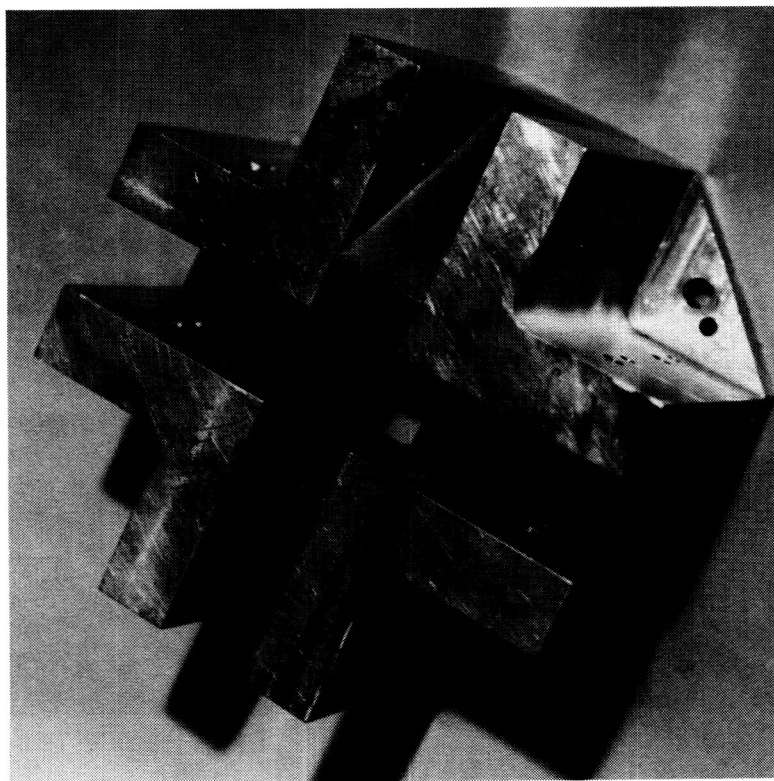
L-89-12939

Figure 2. Unvectored cruciform nozzle with wide flaps mounted on test stand.



L-92-02087

Looking downstream

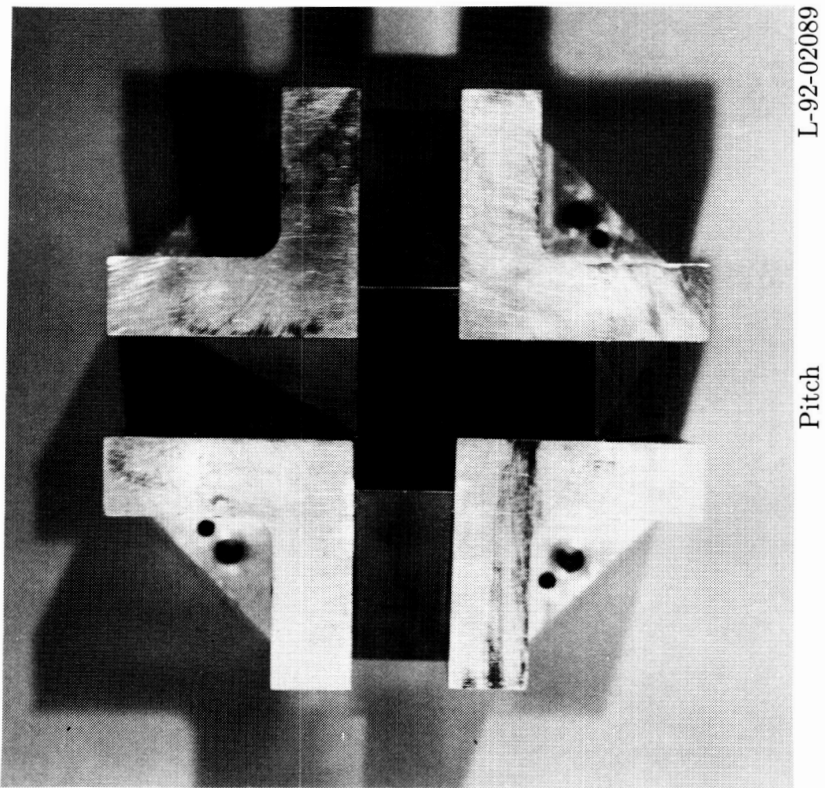
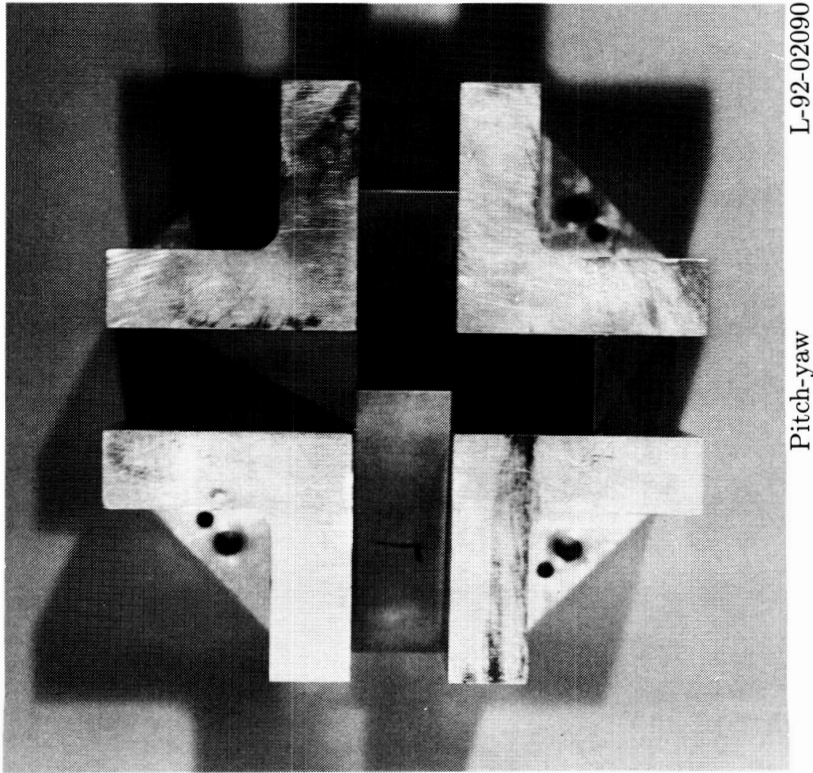


L-92-02088

Looking upstream

(a) Upstream and downstream views.

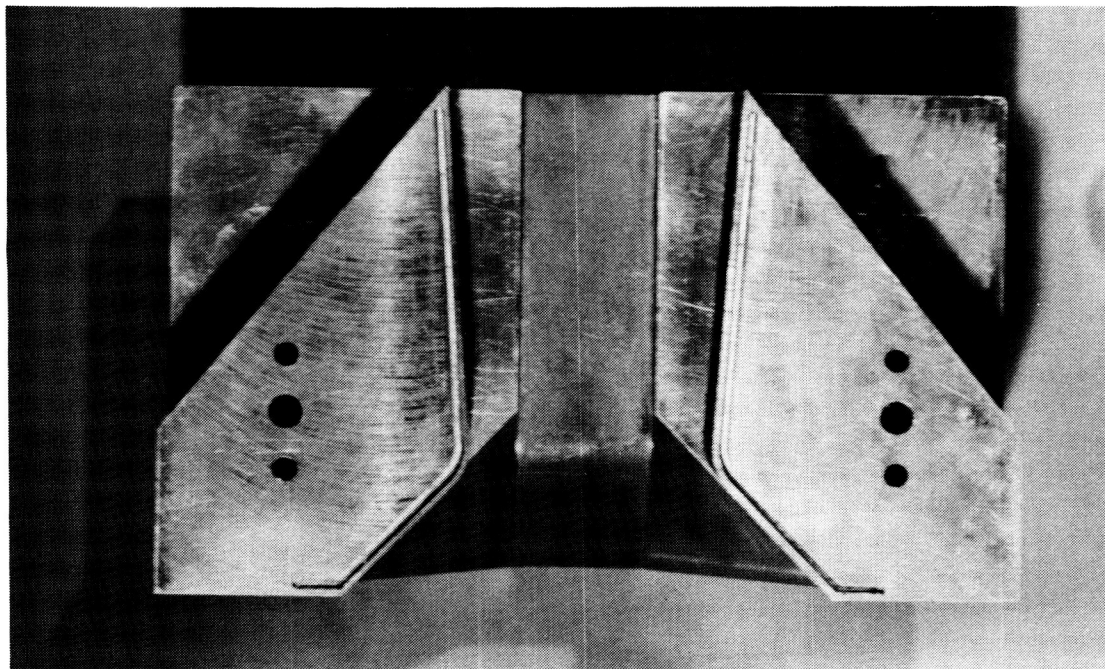
Figure 3. Cruciform nozzle configurations with narrow flaps.



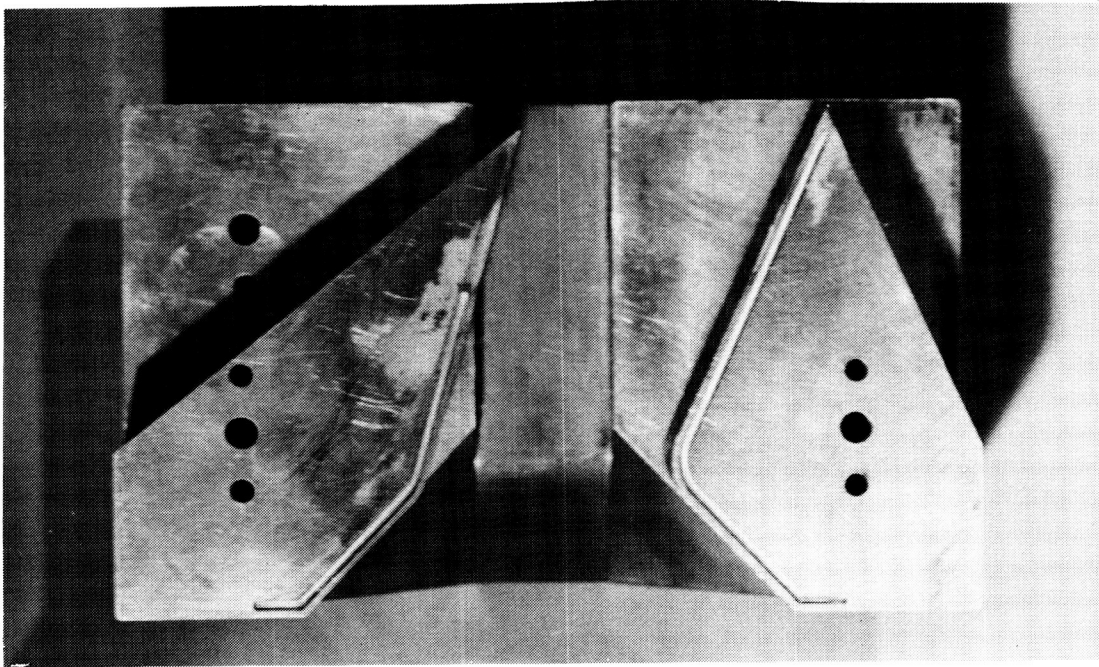
(b) Restricted-flap configuration for pitch and pitch-yaw vectoring.

Figure 3. Continued.

ORIGINAL PAGE
BLACK AND WHITE PHOTOGRAPH



Unvectored L-92-02092

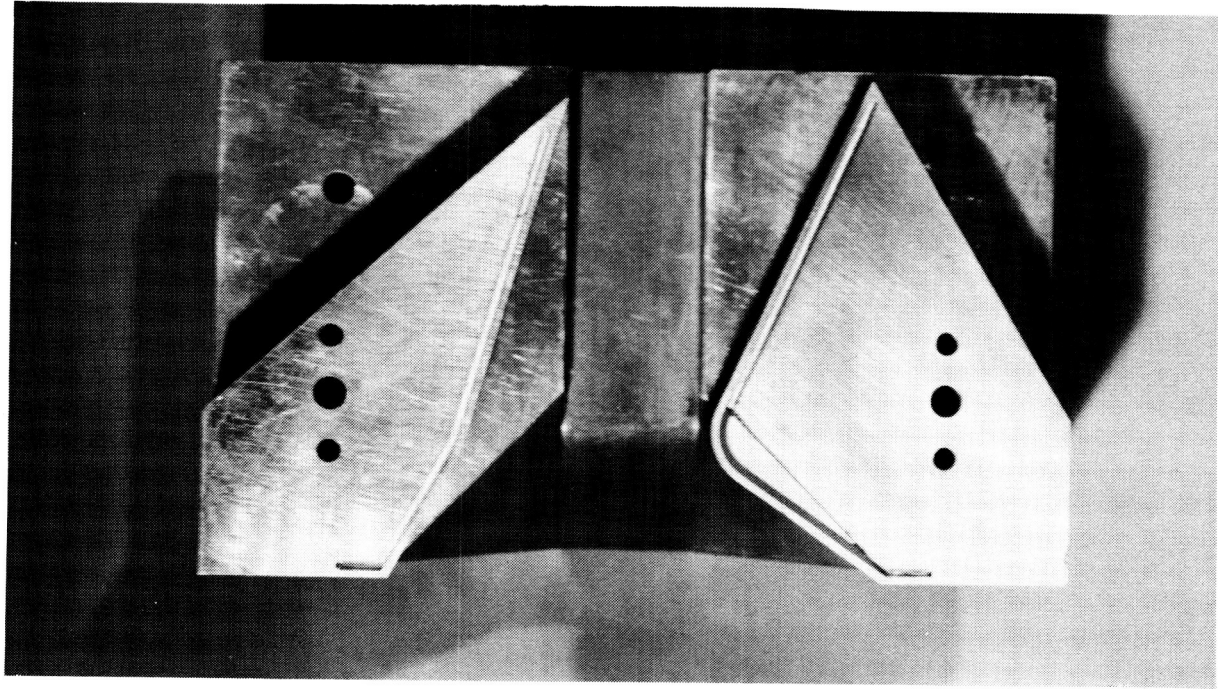


Basic pitch vectored L-92-02091

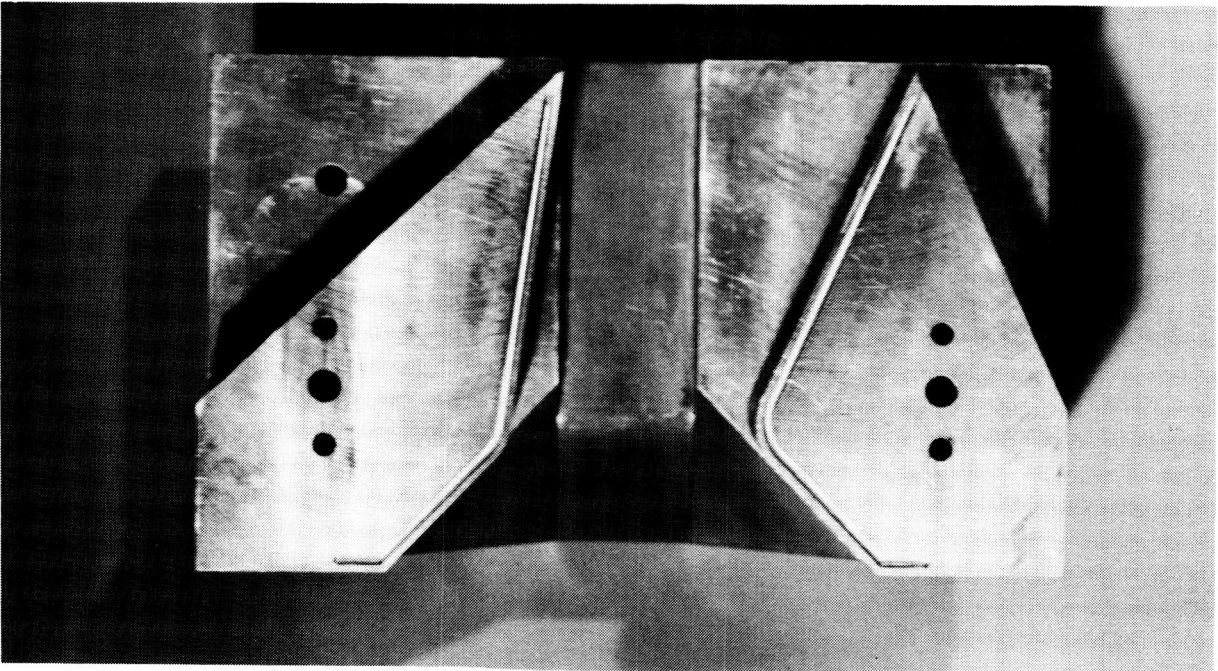
(c) Unvectored and basic pitch-vectored configurations with flow from left to right. Model disassembled for clarity.

Figure 3. Continued.

ORIGINAL PAGE
BLACK AND WHITE PHOTOGRAPH



Shifted throat L-92-02093

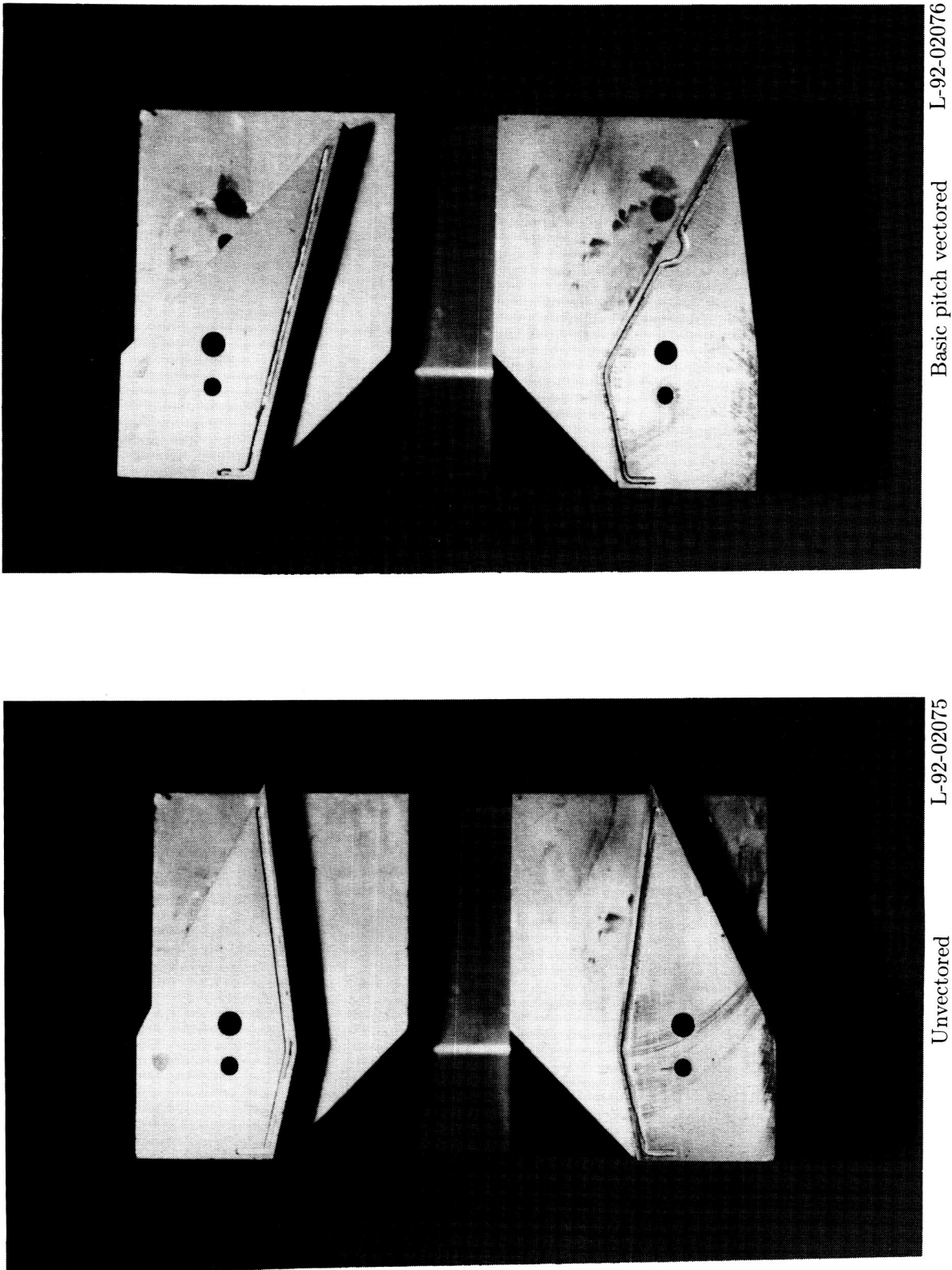


Restricted flap L-92-02094

(d) Restricted-flap and shifted-throat configurations with flow from left to right. Model disassembled for clarity.

Figure 3. Continued.

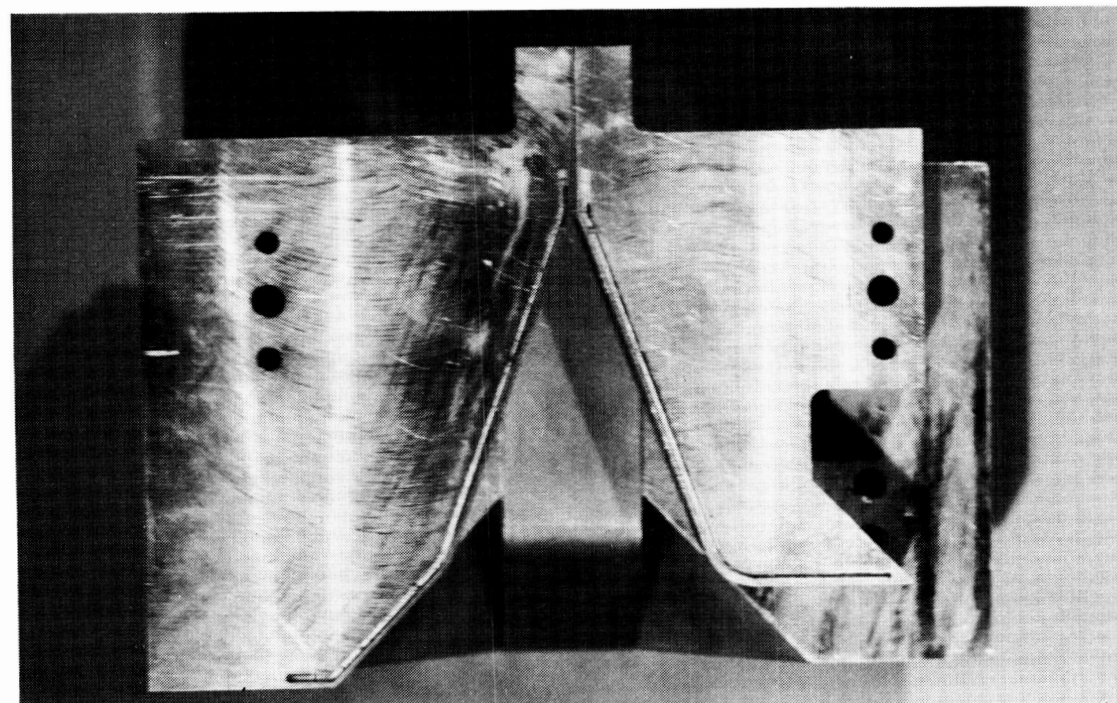
ORIGINAL PAGE
BLACK AND WHITE PHOTOGRAPH



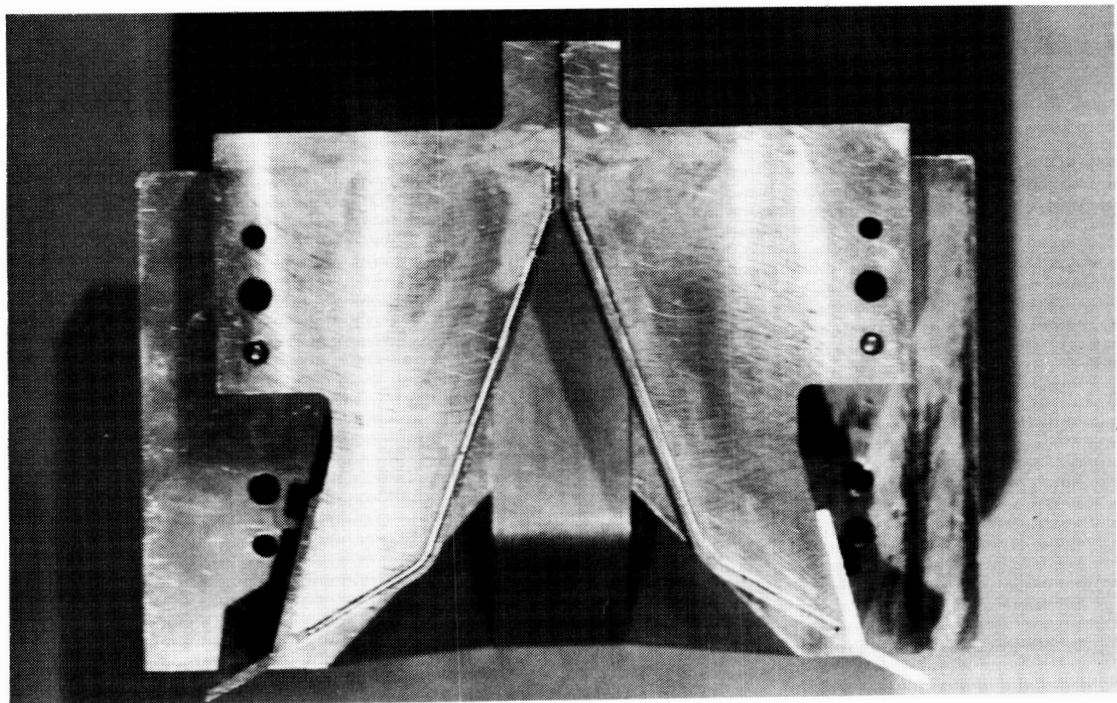
(e) Unvectored and basic pitch-vectored nozzle in A/B mode with flow from left to right. Model disassembled for clarity.

Figure 3. Continued.

ORIGINAL PAGE
BLACK AND WHITE PHOTOGRAPH



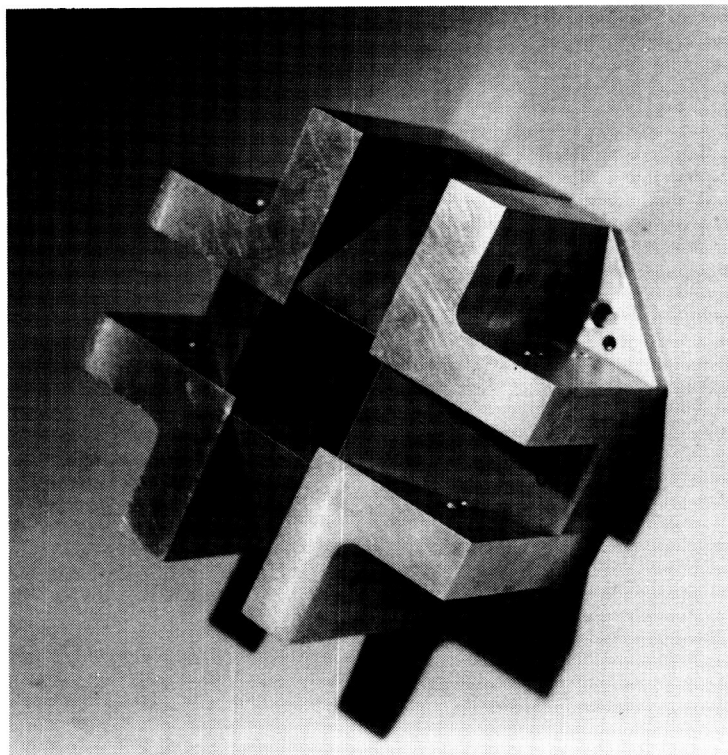
Vertical thrust L-92-02083



Thrust reverse L-92-02084

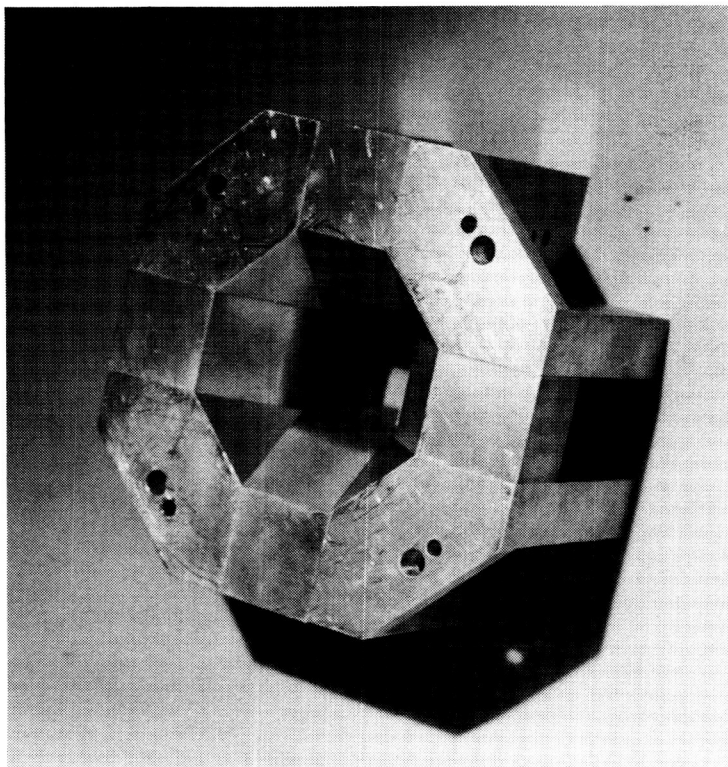
(f) Vertical-thrust and thrust-reverser configurations with flow entering from left. Model disassembled for clarity.

Figure 3. Concluded.



Looking upstream

L-92-02082

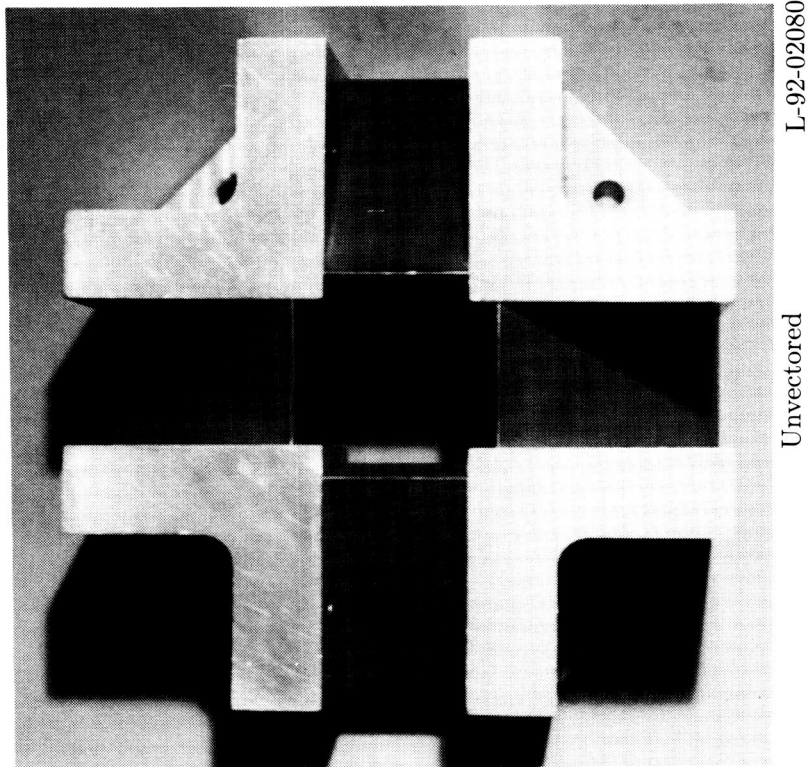
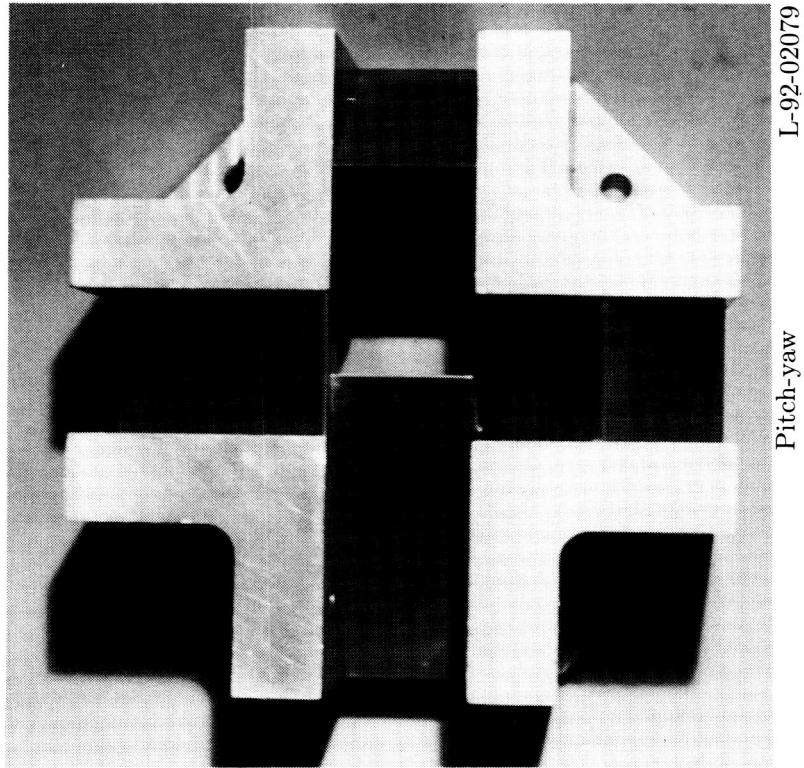


Looking downstream

L-92-02081

(a) Upstream and downstream views.

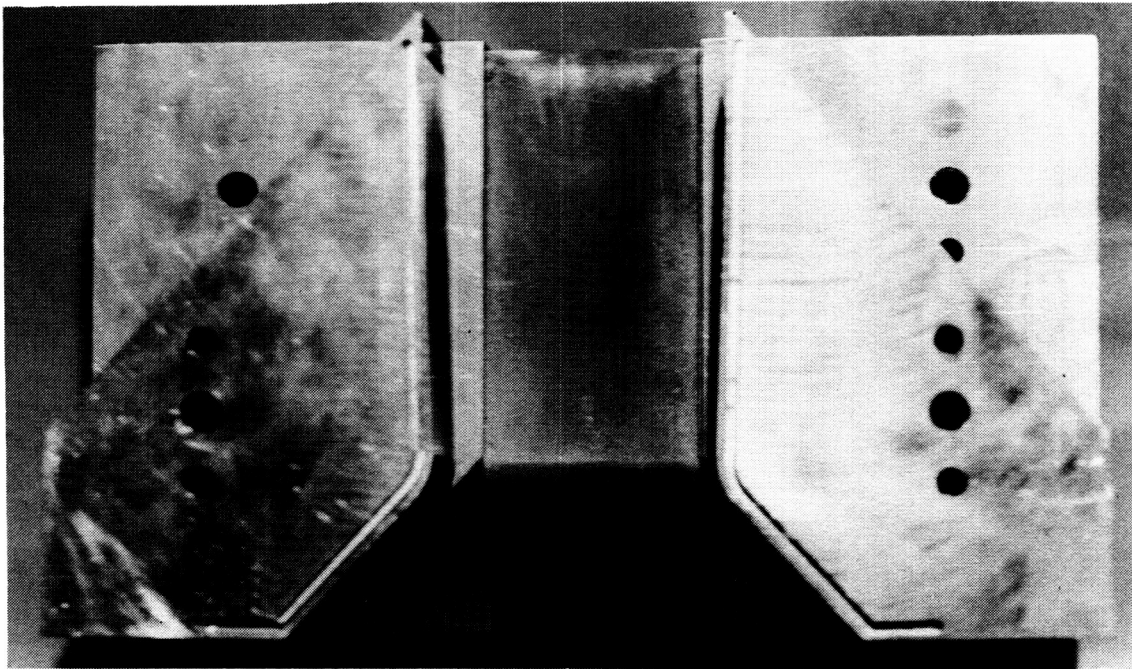
Figure 4. Cruciform nozzle configurations with wide flaps.



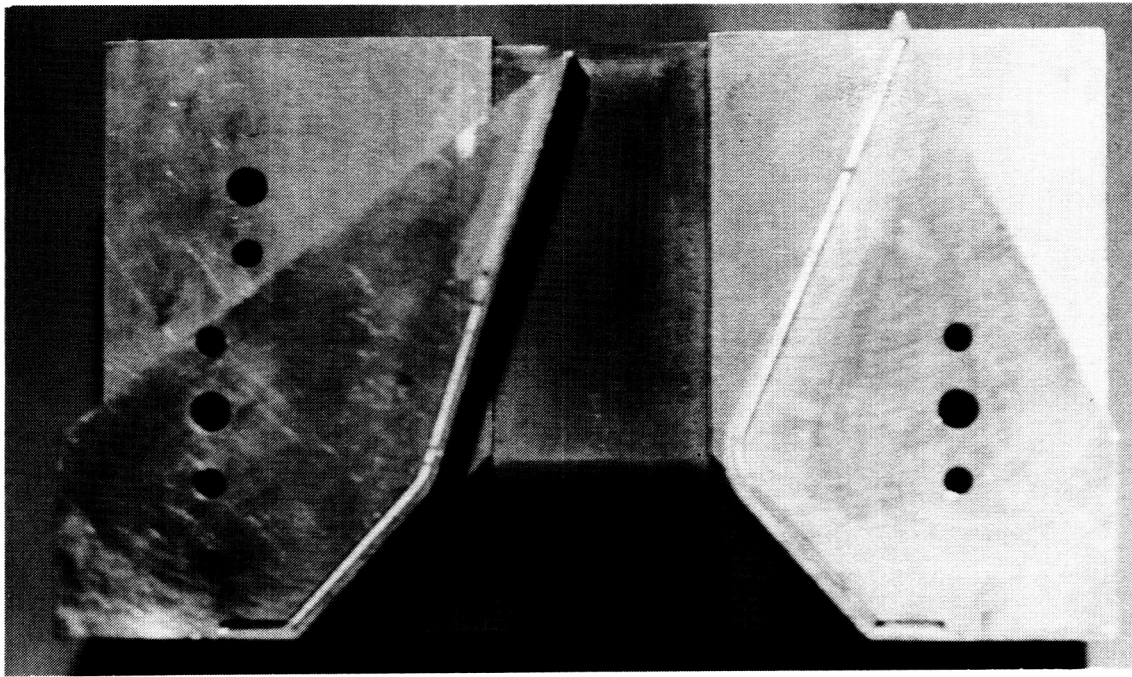
(b) Unvectored configuration and restricted-flap configuration for pitch-yaw vectoring.

Figure 4. Continued.

ORIGINAL PAGE
BLACK AND WHITE PHOTOGRAPH



Unvectored L-92-02078

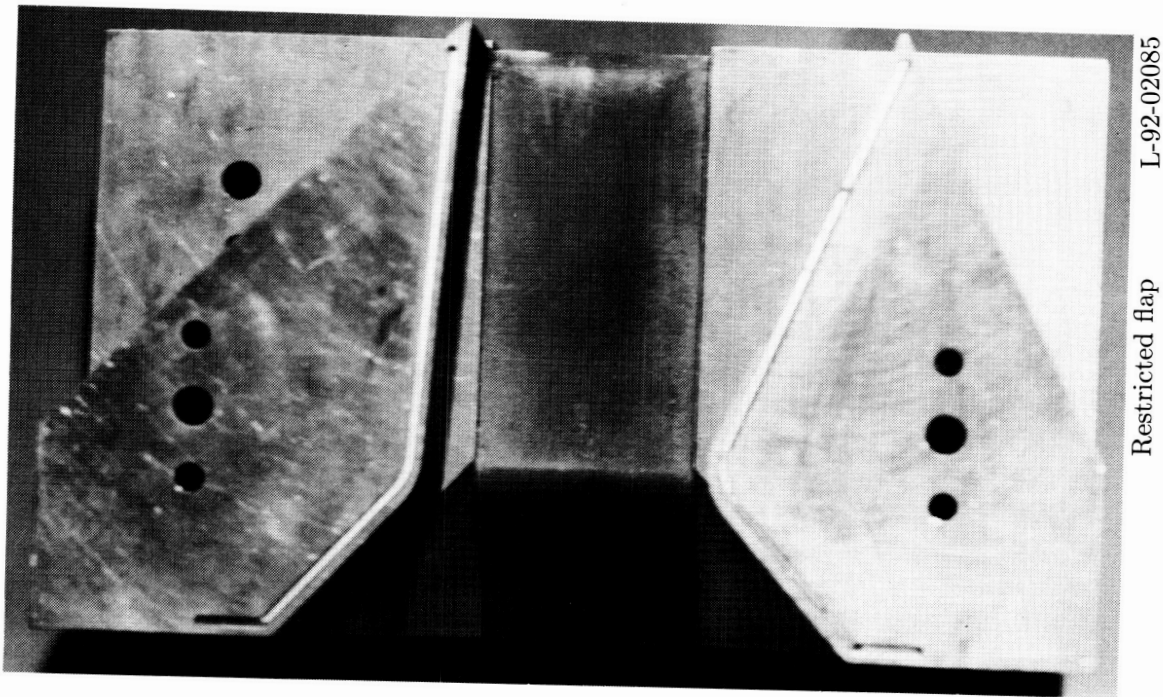


Basic pitch vectored L-92-02077

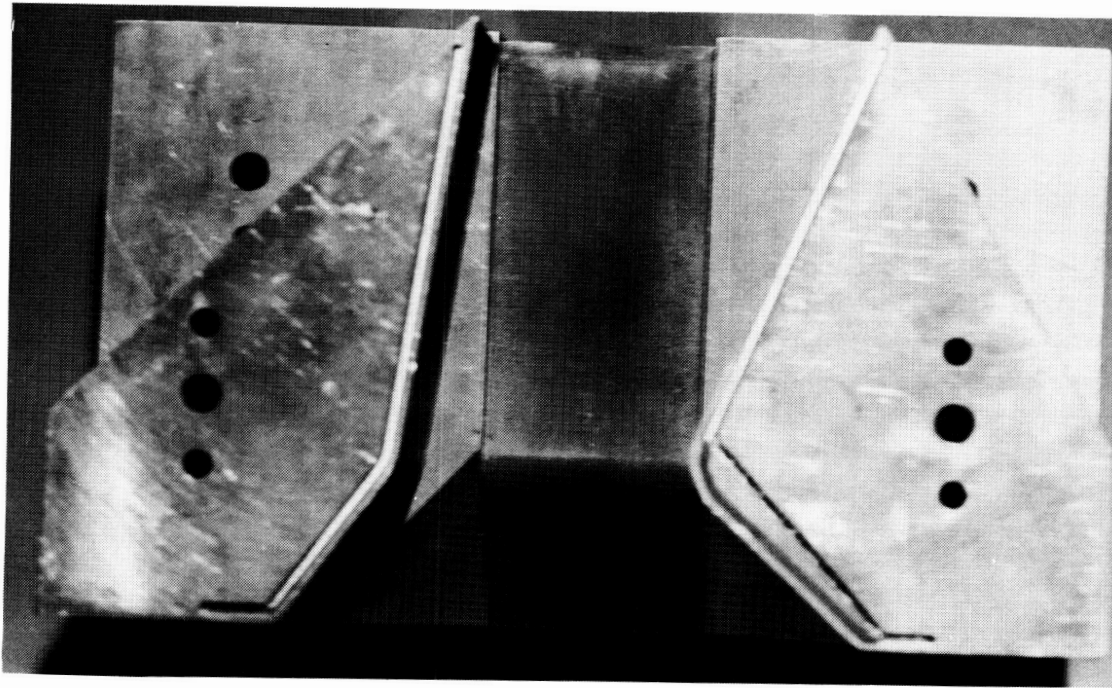
(c) Unvectored and basic pitch-vectored configurations with flow from left to right. Model disassembled for clarity.

Figure 4. Continued.

ORIGINAL PAGE
BLACK AND WHITE PHOTOGRAPH



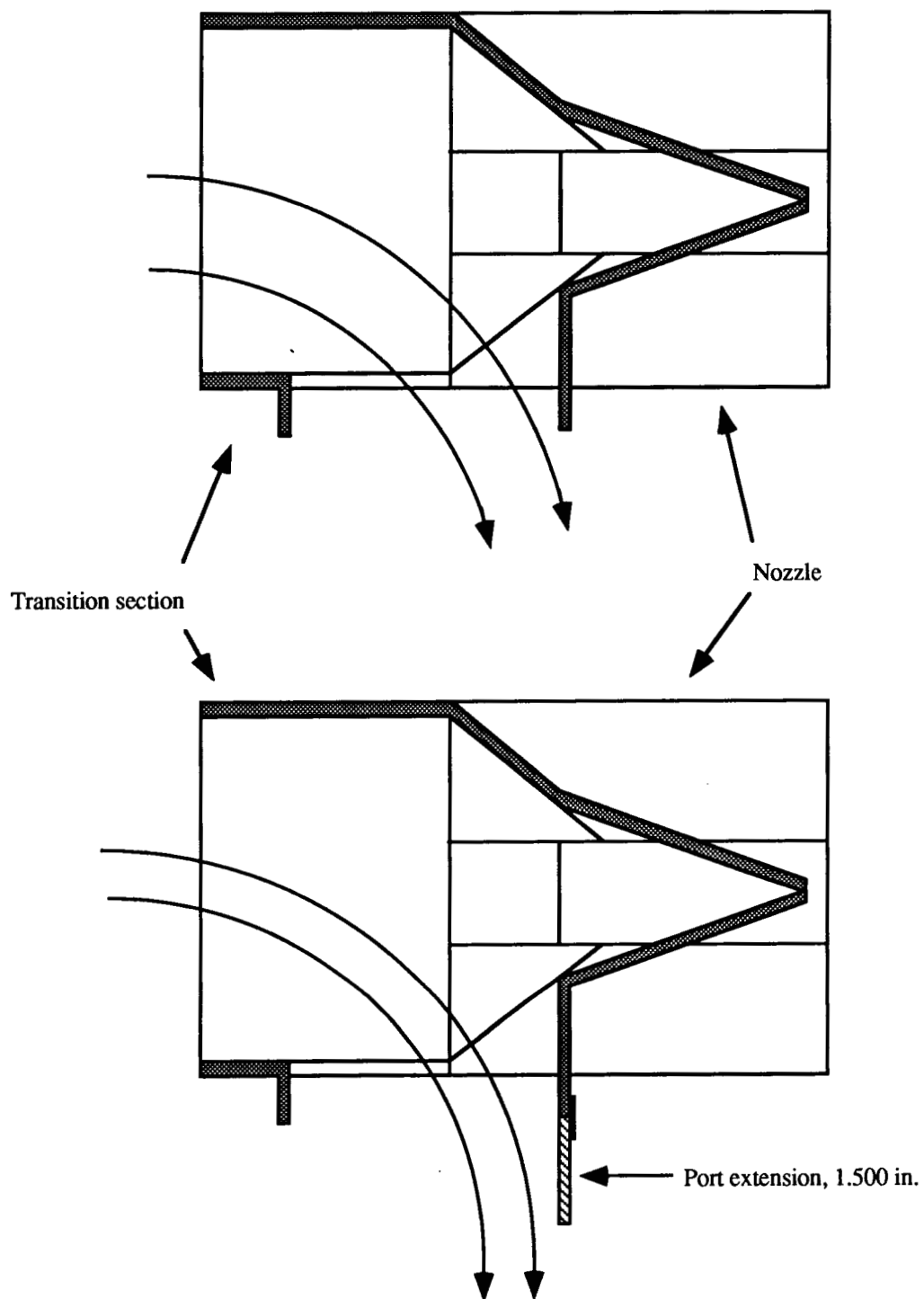
Restricted flap L-92-02085



Shifted throat L-92-02086

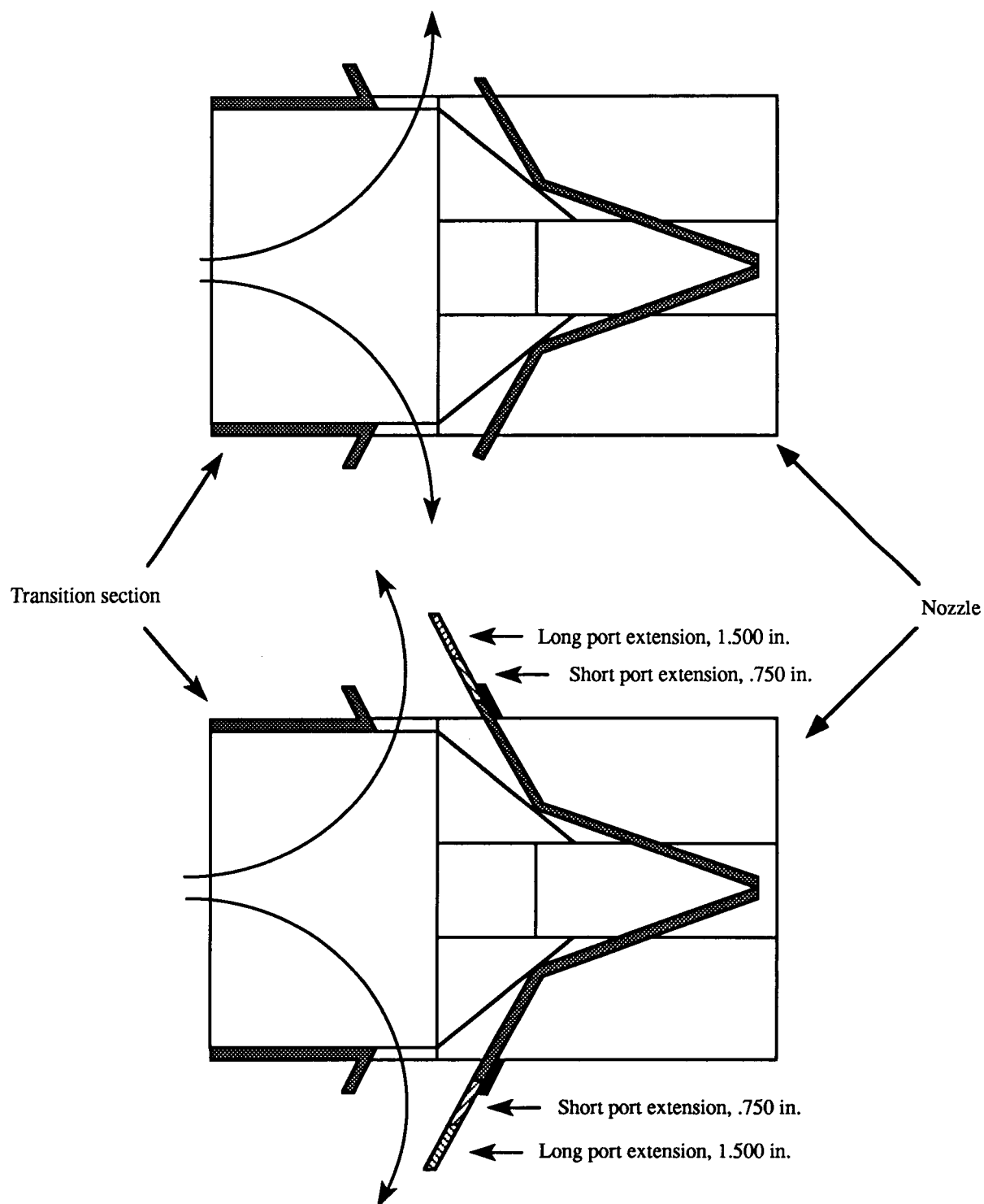
(d) Restricted-flap and shifted-throat configurations with flow from left to right. Model disassembled for clarity.

Figure 4. Concluded.



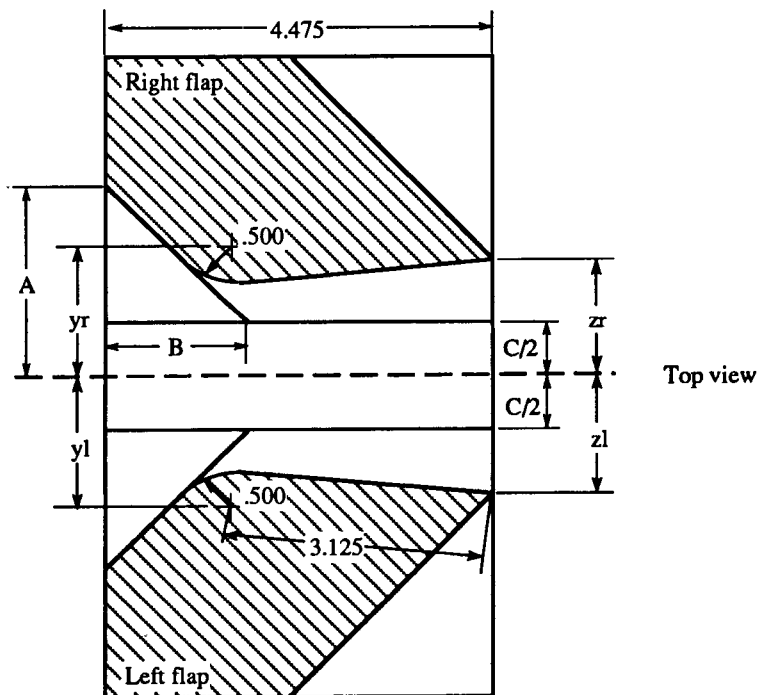
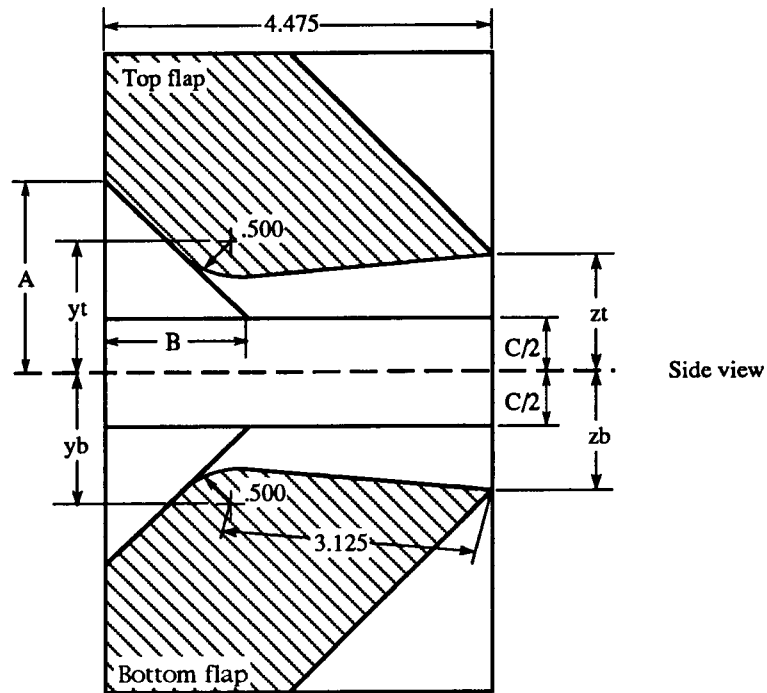
(a) Vertical-thrust mode; side view.

Figure 5. Vertical-thrust and thrust-reverser configurations.



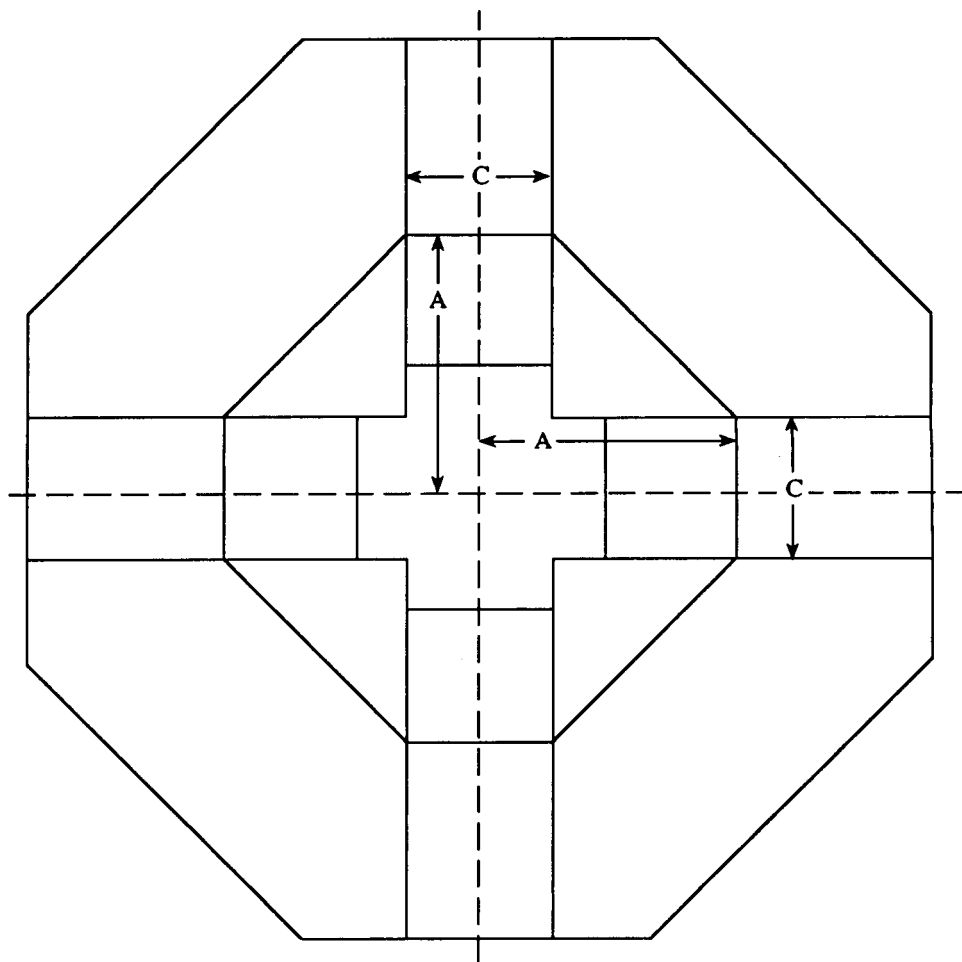
(b) Thrust-reverser mode; top view.

Figure 5. Concluded.



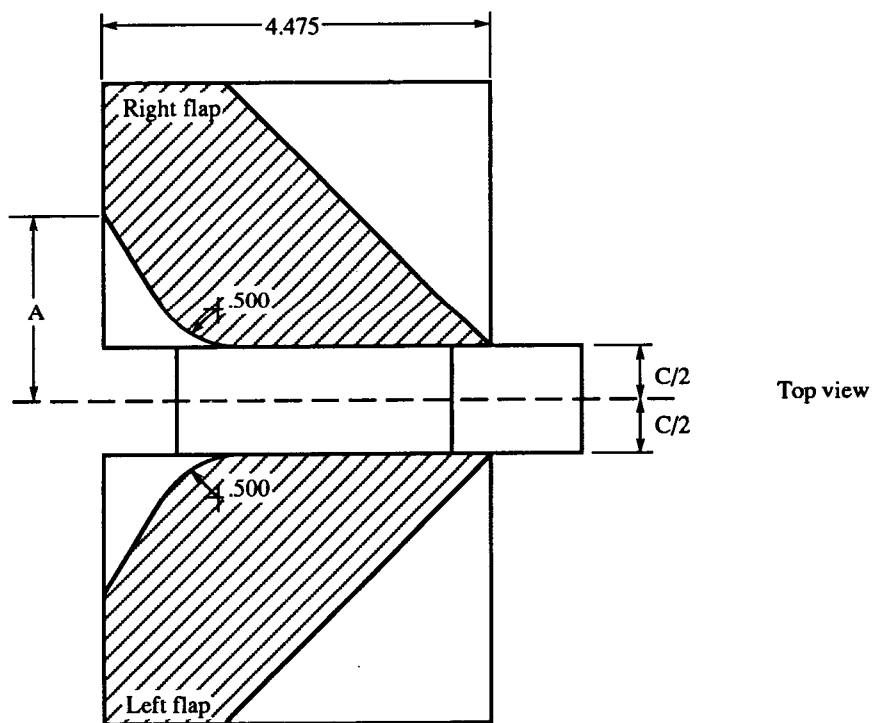
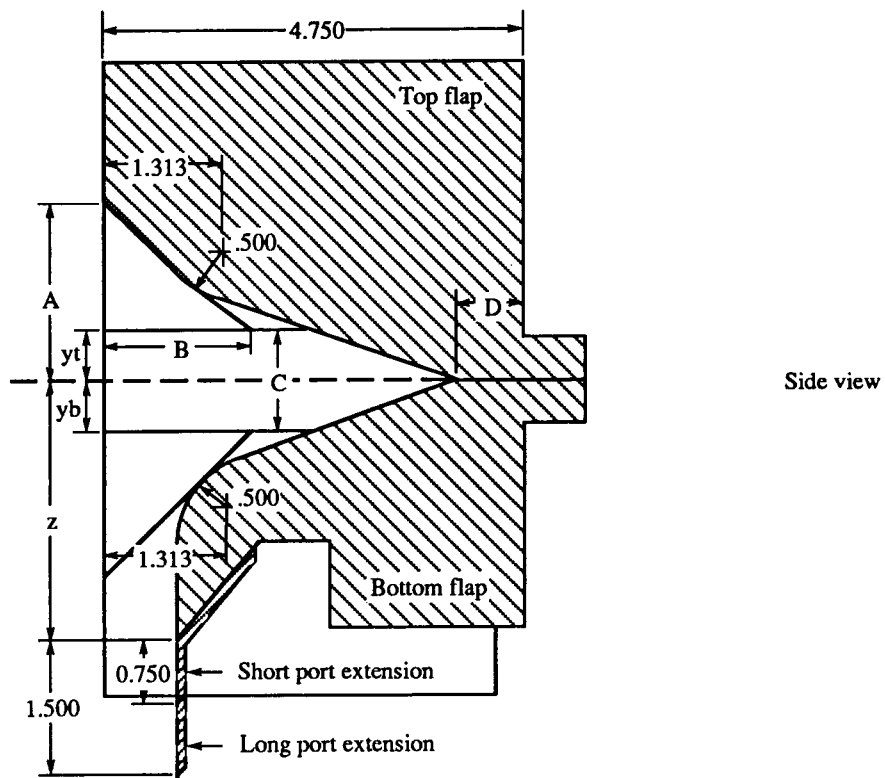
(a) Internal dimensions of cruciform nozzle.

Figure 6. Nozzle geometric details. All dimensions in inches unless otherwise noted.



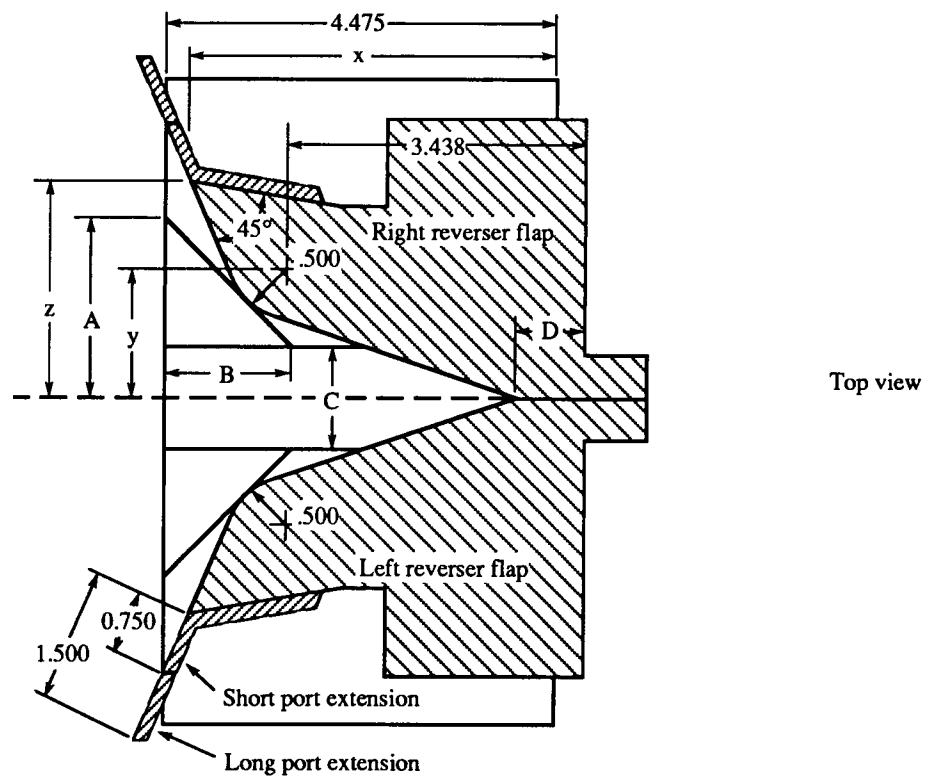
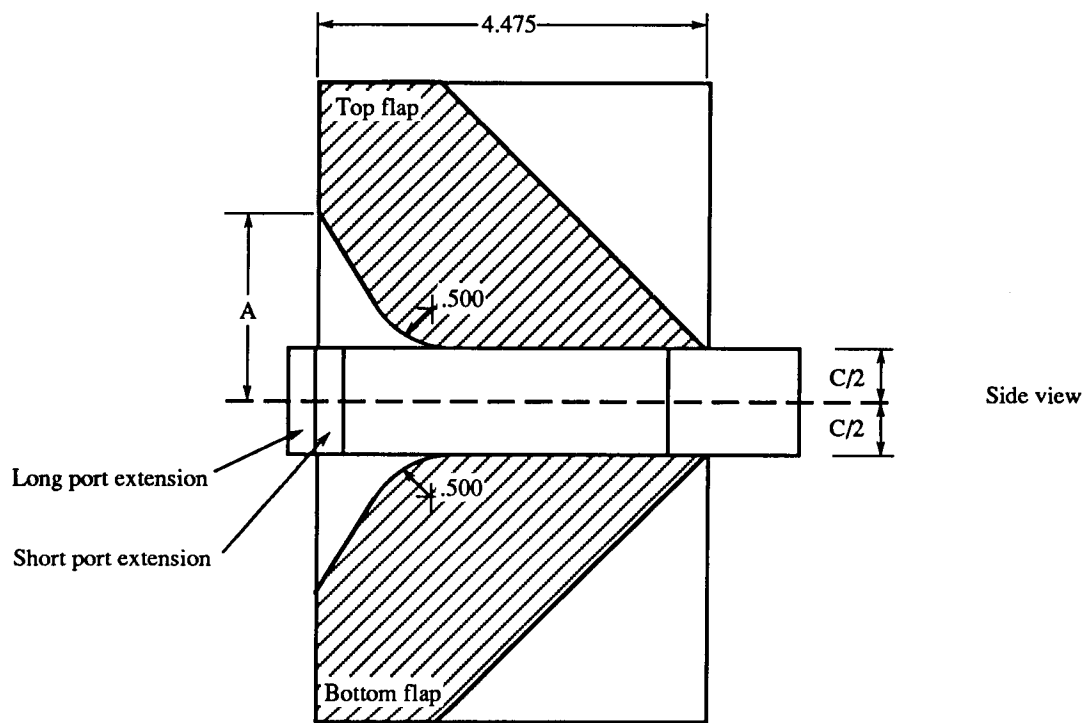
(b) Upstream view of cruciform nozzle.

Figure 6. Continued.



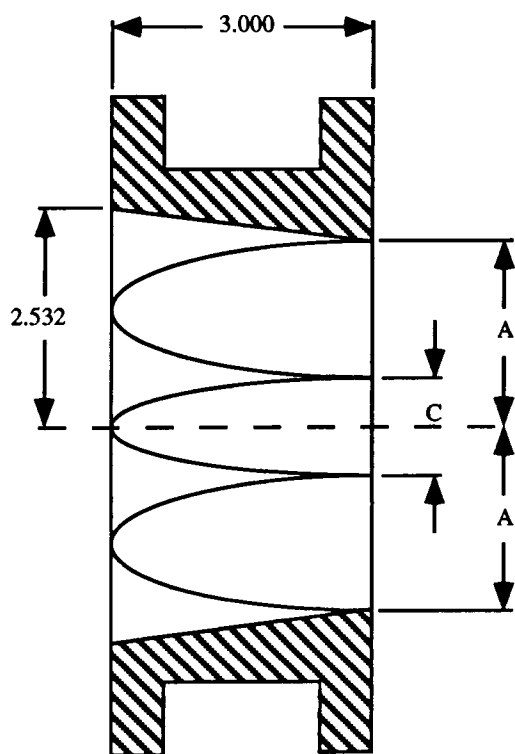
(c) Internal dimensions of vertical-thrust configuration.

Figure 6. Continued.

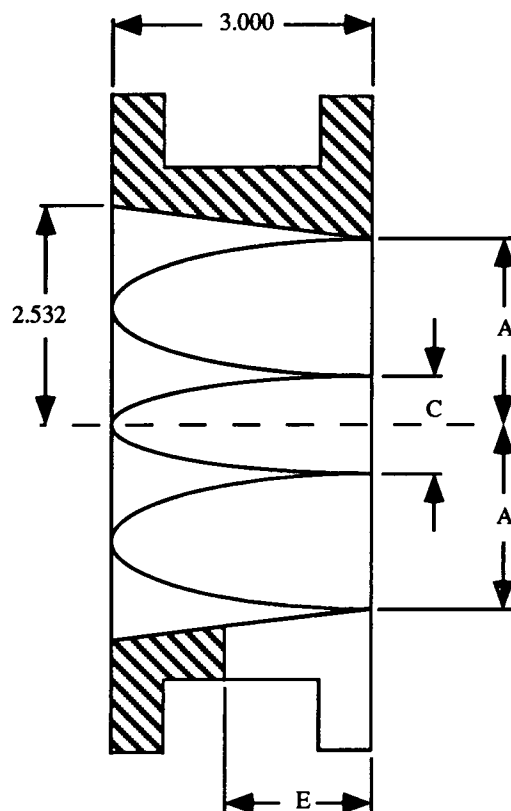


(d) Internal dimensions of thrust-reverser configuration.

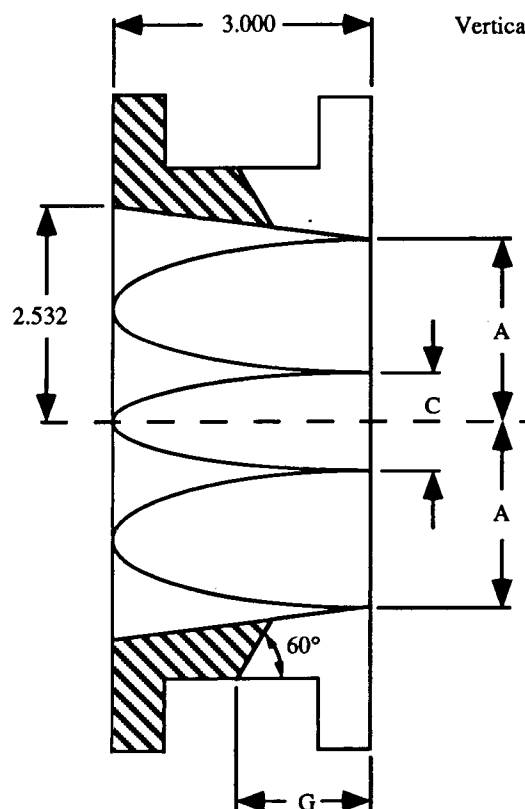
Figure 6. Continued.



Cruise transition section



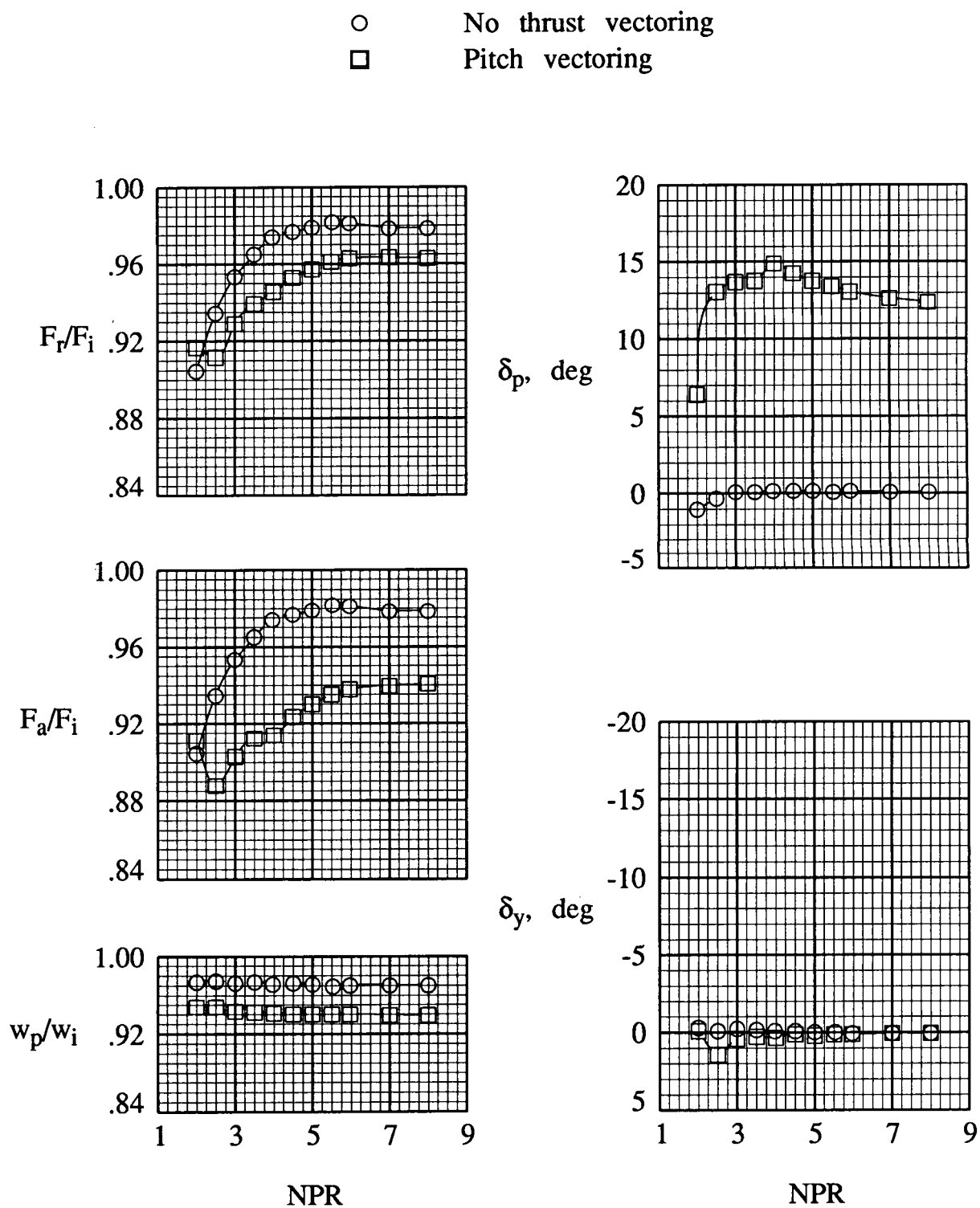
Vertical-thrust transition section



Thrust-reverser transition section

(e) Transition section from circular to octagonal cross section; flow enters from left.

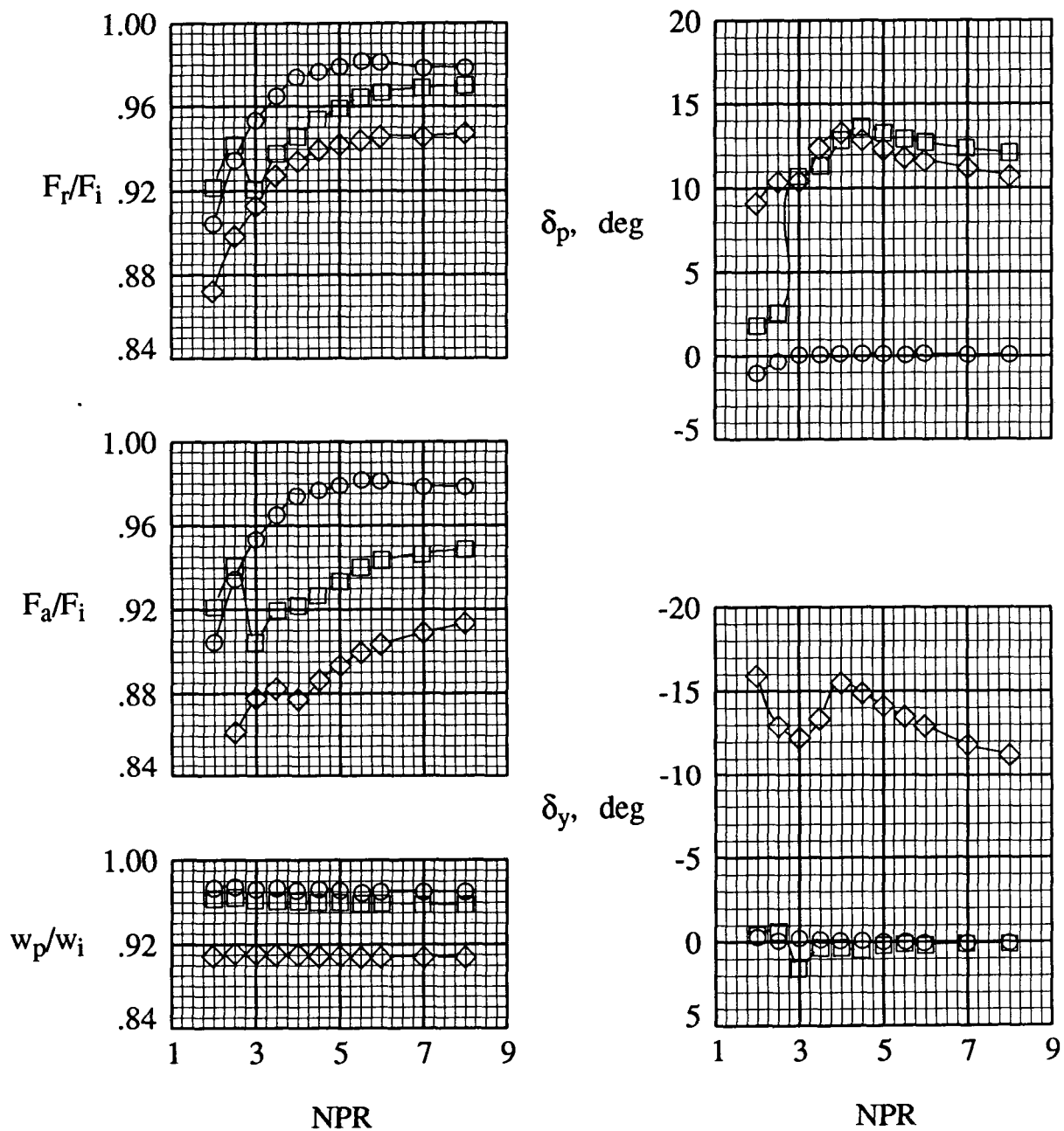
Figure 6. Concluded.



(a) Basic pitch configuration.

Figure 7. Performance of dry power cruciform nozzle with narrow flaps and $A_e/A_t = 1.3$.

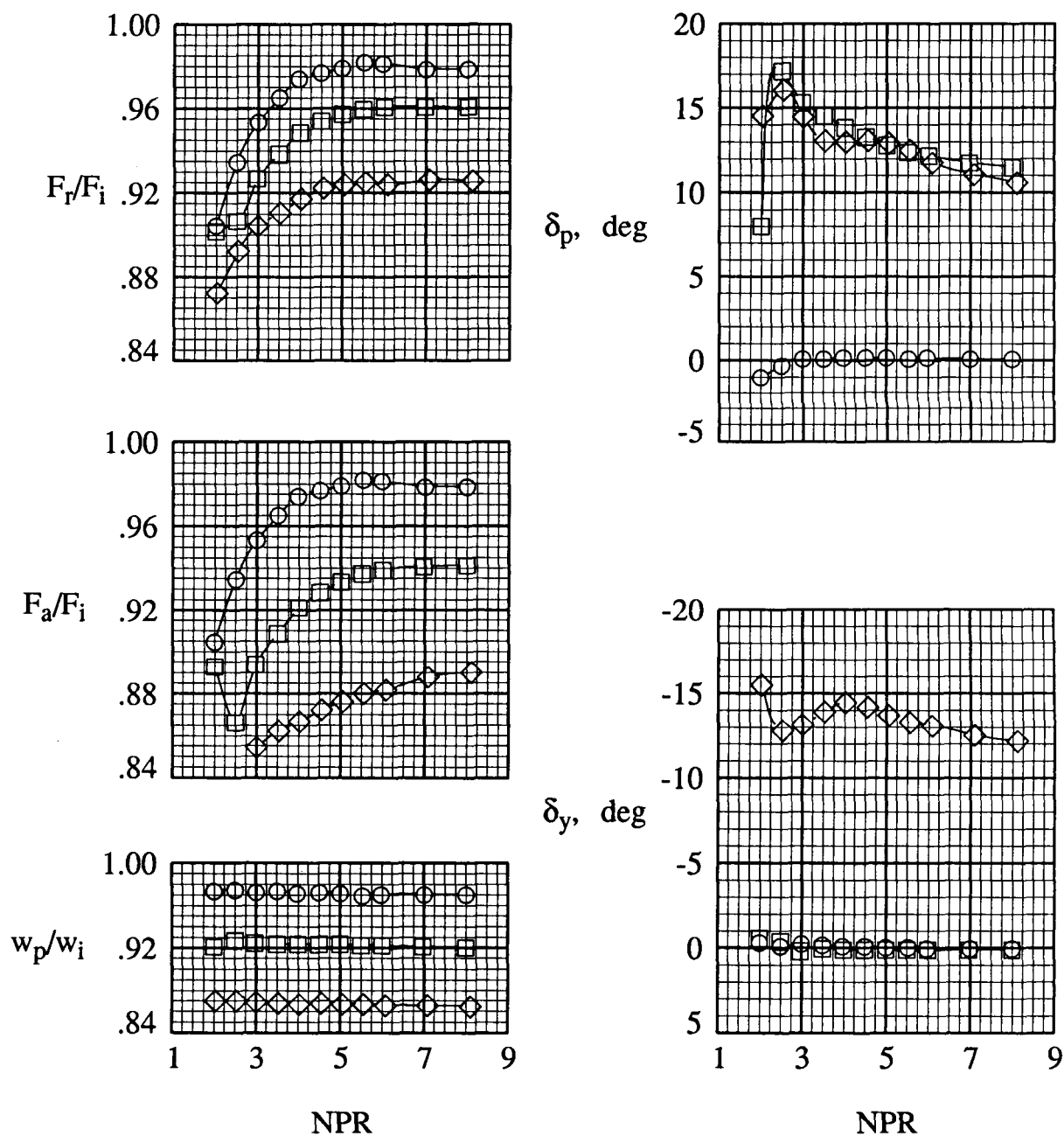
- No thrust vectoring
- Pitch vectoring
- ◇ Pitch-yaw vectoring



(b) Restricted-flap configuration.

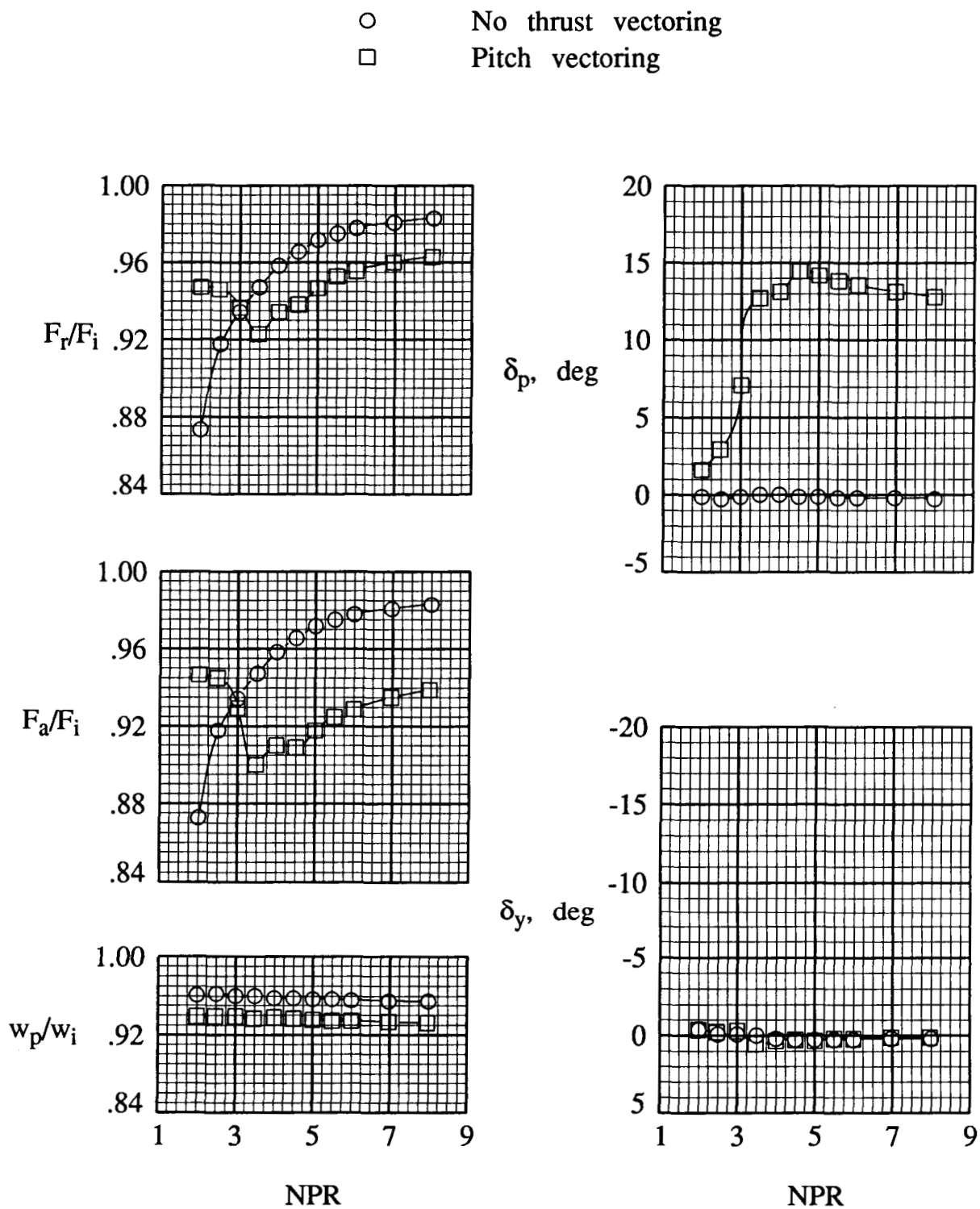
Figure 7. Continued.

- No thrust vectoring
- Pitch vectoring
- ◇ Pitch-yaw vectoring



(c) Shifted-throat configuration.

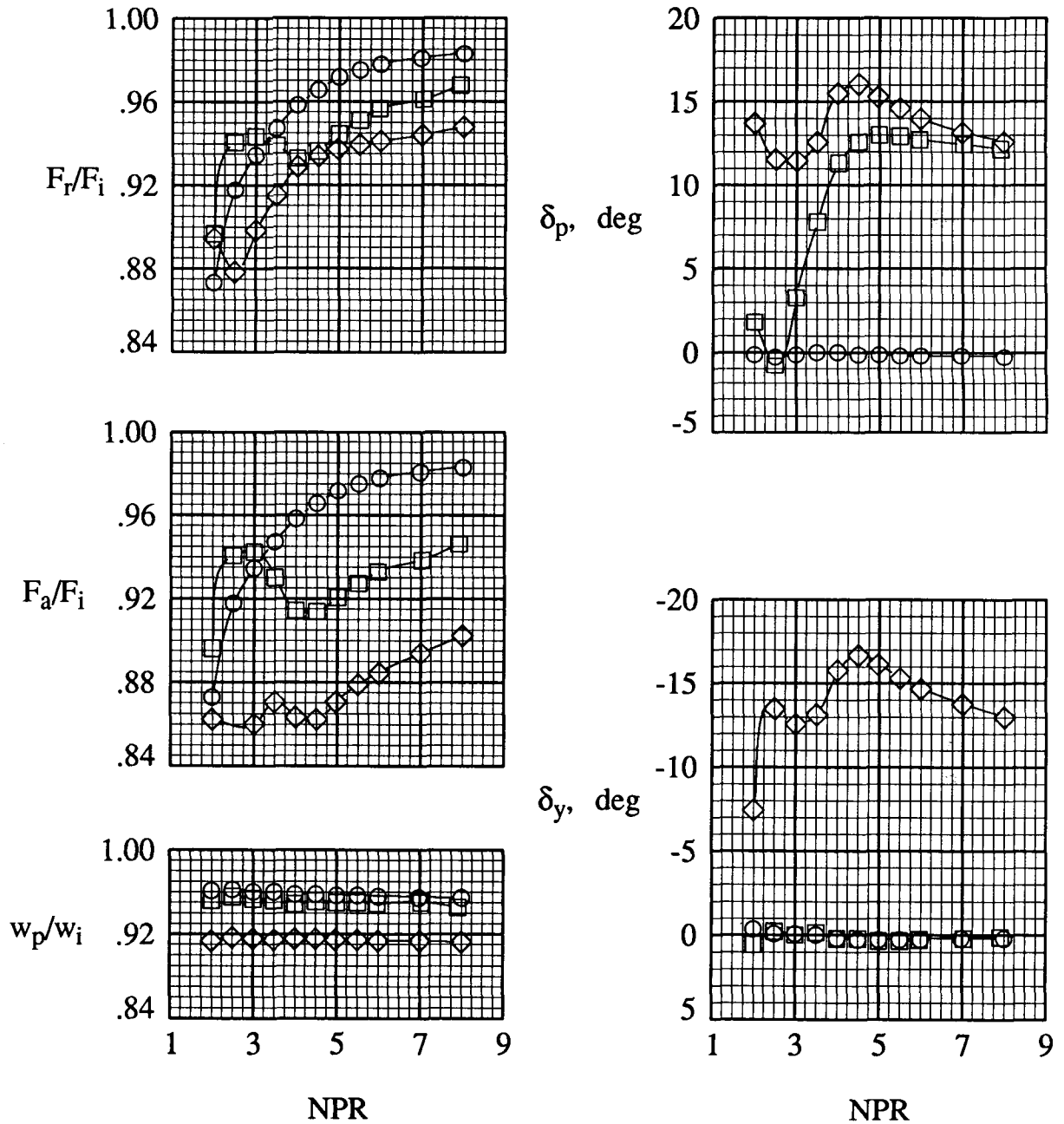
Figure 7. Concluded.



(a) Basic pitch configuration.

Figure 8. Performance of dry power cruciform nozzle with narrow flaps and $A_e/A_t = 1.5$.

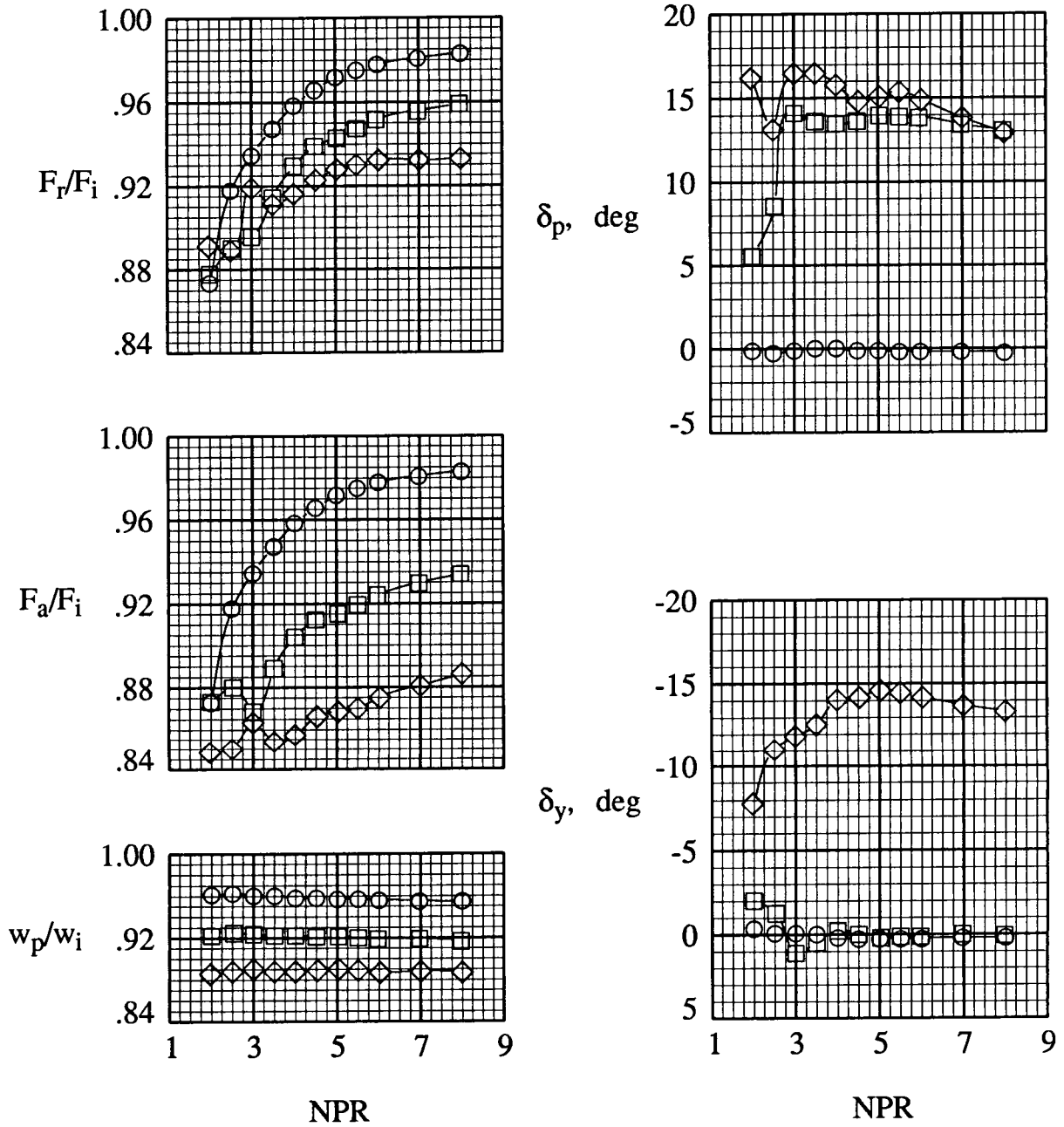
- No thrust vectoring
- Pitch vectoring
- ◇ Pitch-yaw vectoring



(b) Restricted-flap configuration.

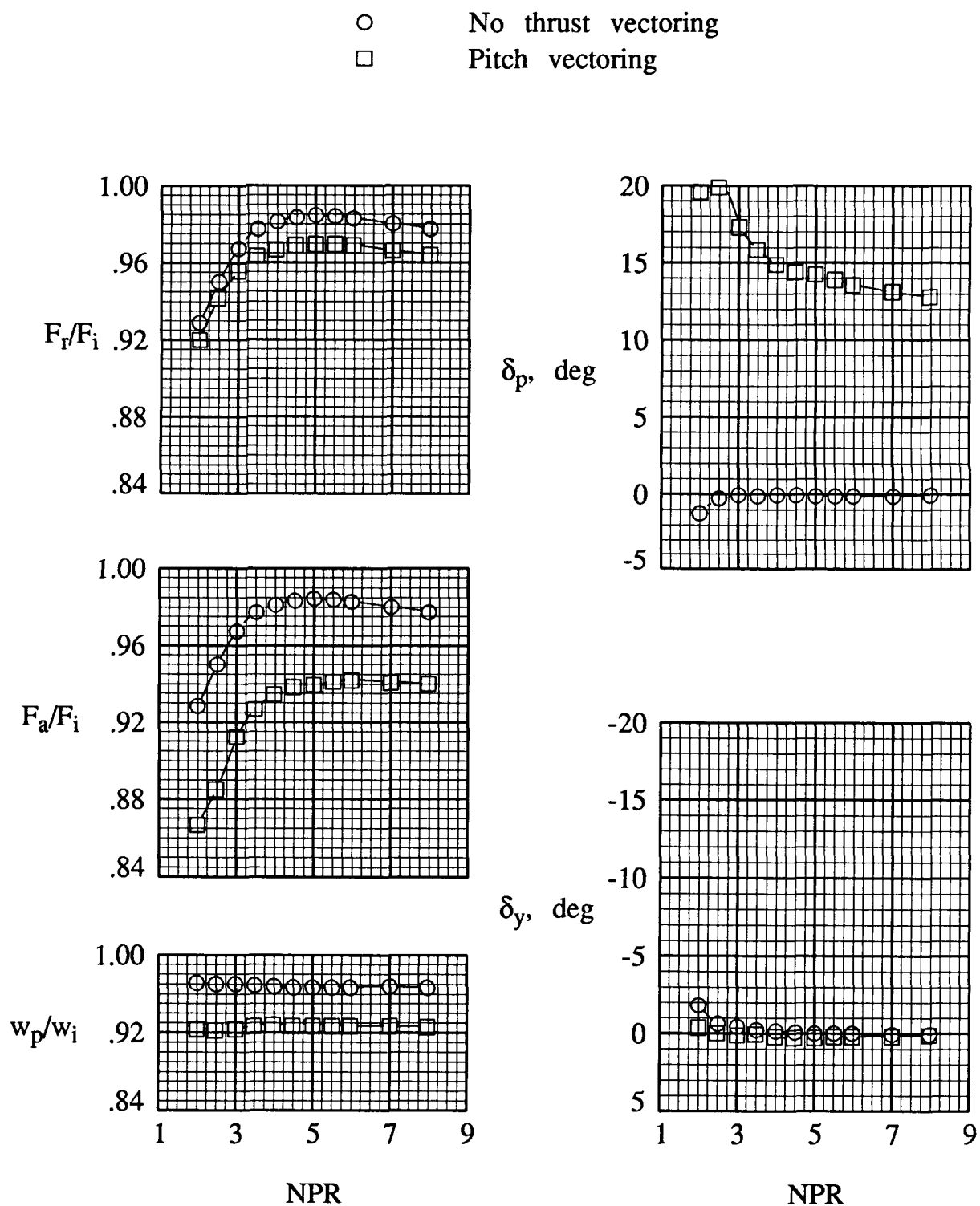
Figure 8. Continued.

- No thrust vectoring
- Pitch vectoring
- ◇ Pitch-yaw vectoring



(c) Shifted-throat configuration.

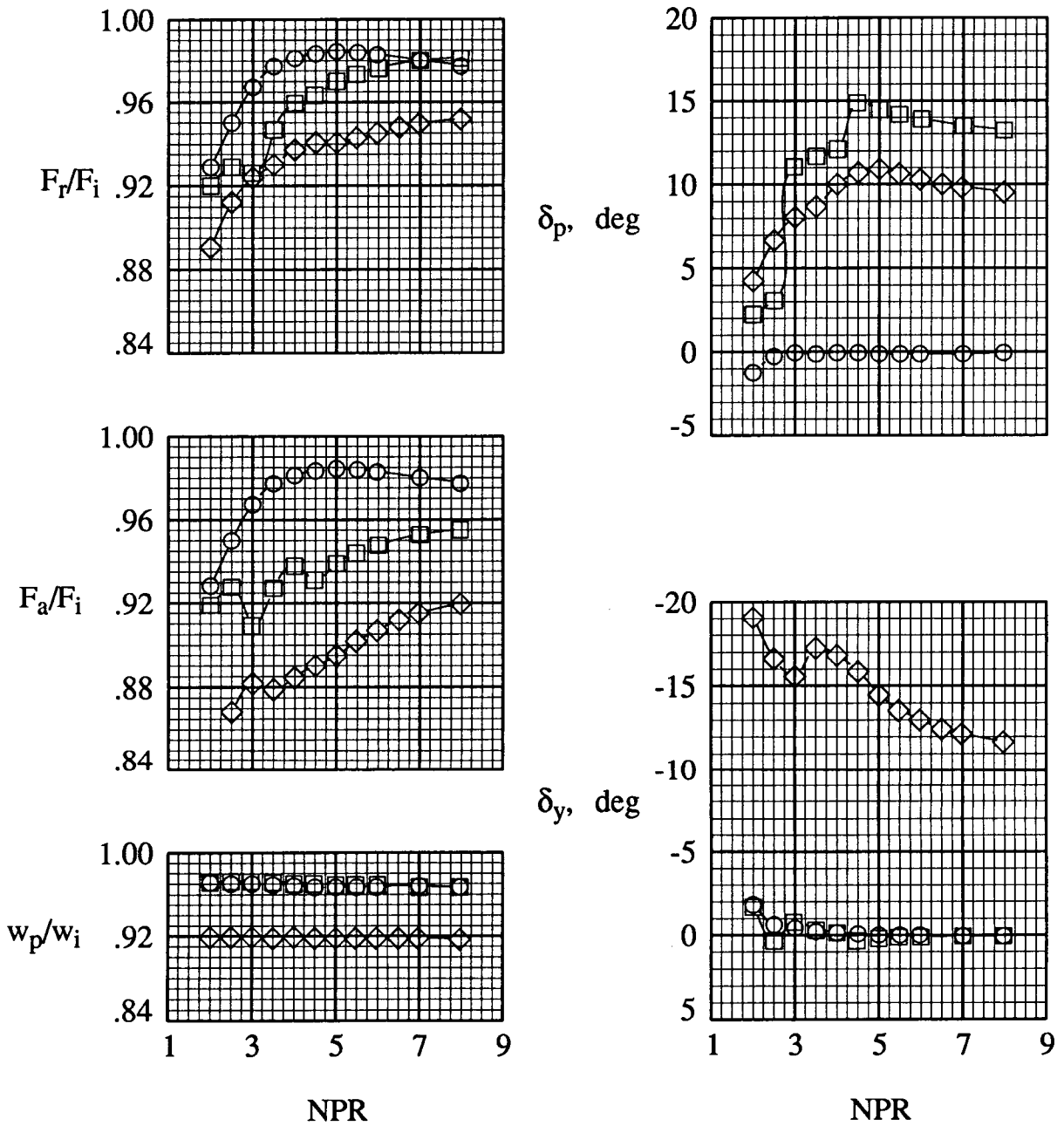
Figure 8. Concluded.



(a) Basic pitch configuration.

Figure 9. Performance of dry power cruciform nozzle with wide flaps and $A_e/A_t = 1.2$.

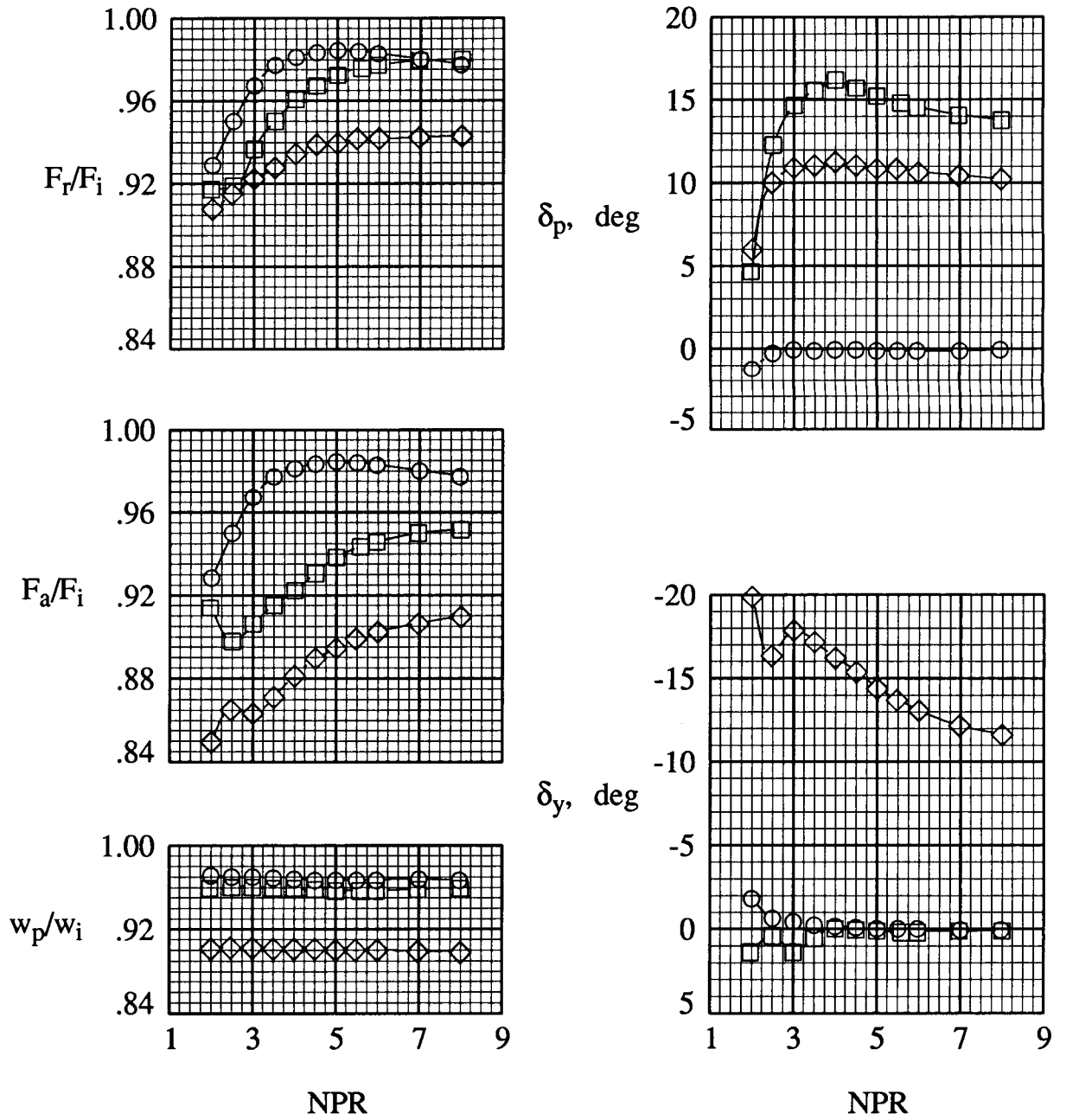
- No thrust vectoring
- Pitch vectoring
- ◇ Pitch-yaw vectoring



(b) Restricted-flap configuration.

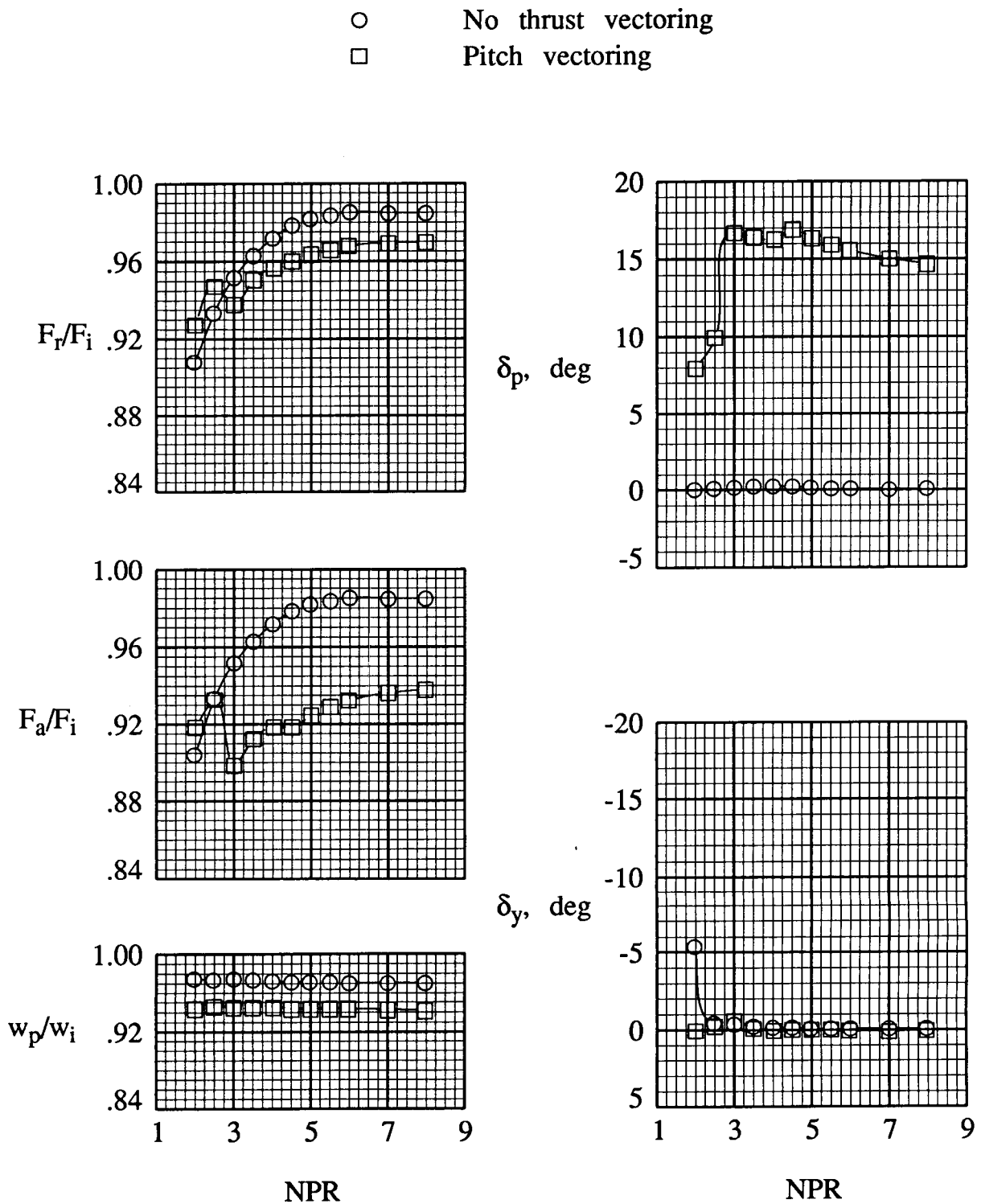
Figure 9. Continued.

- No thrust vectoring
- Pitch vectoring
- ◇ Pitch-yaw vectoring



(c) Shifted-throat configuration.

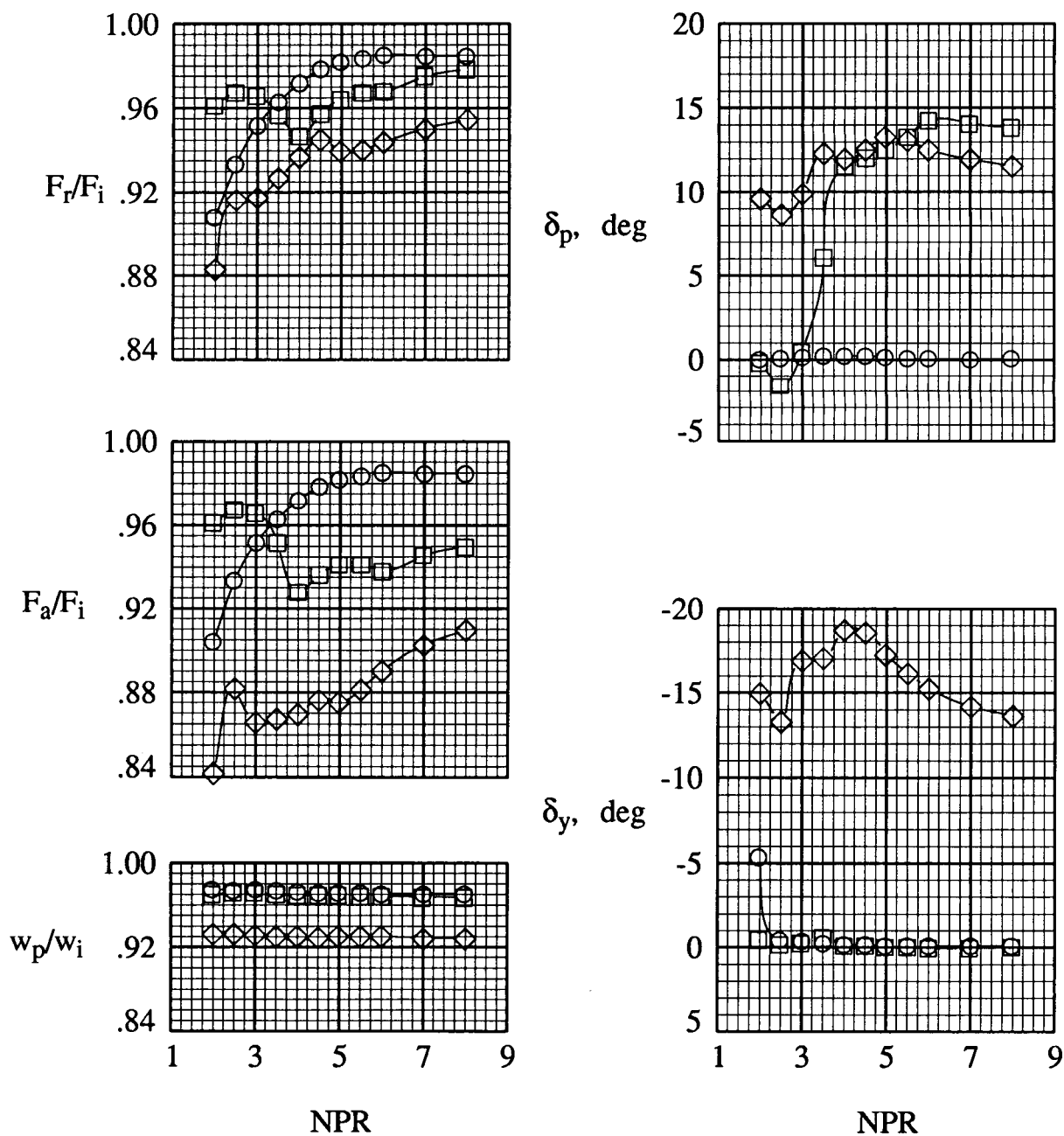
Figure 9. Concluded.



(a) Basic pitch configuration.

Figure 10. Performance of dry power cruciform nozzle with wide flaps and $A_e/A_t = 1.4$.

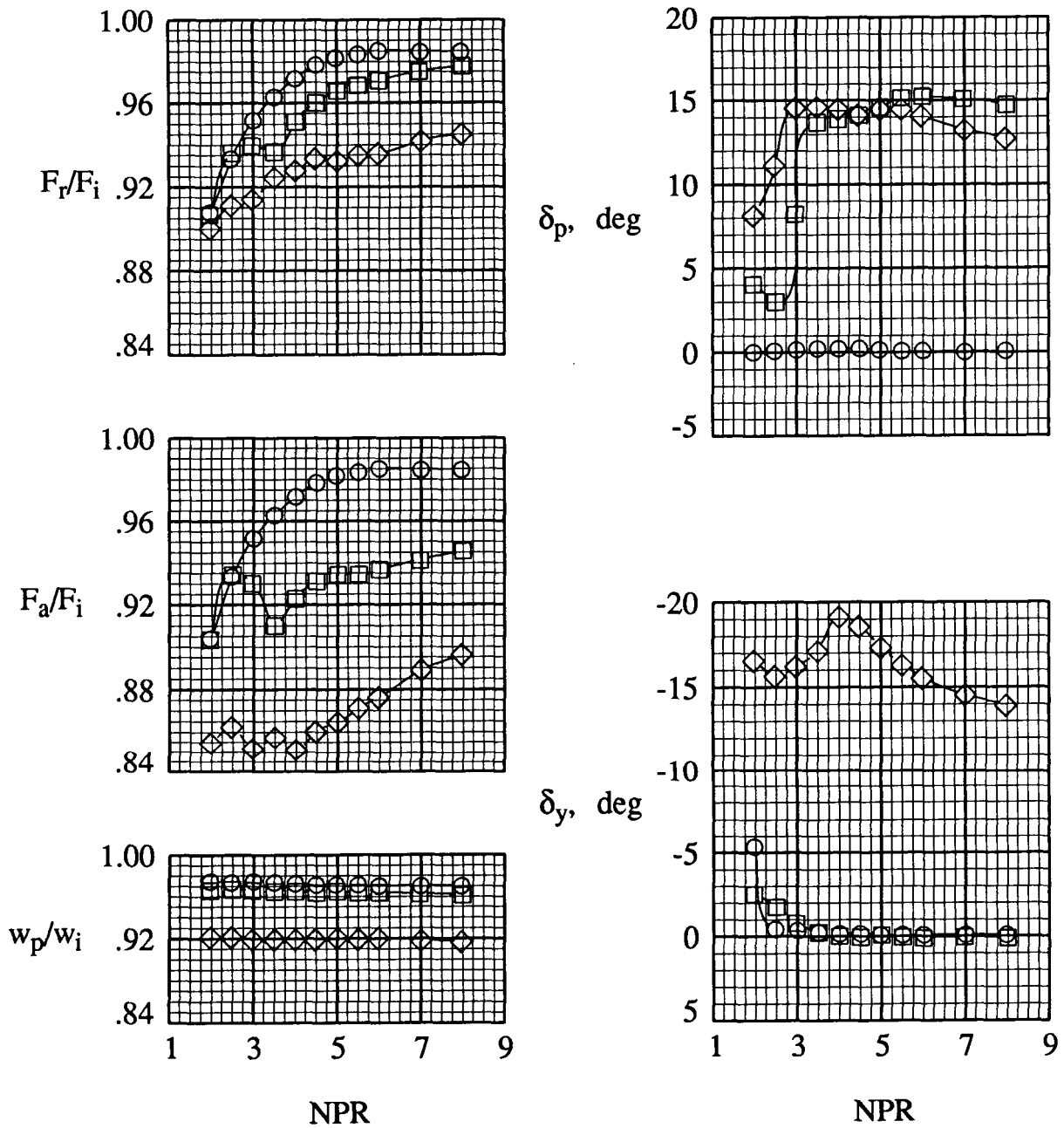
- No thrust vectoring
- Pitch vectoring
- ◇ Pitch-yaw vectoring



(b) Restricted-flap configuration.

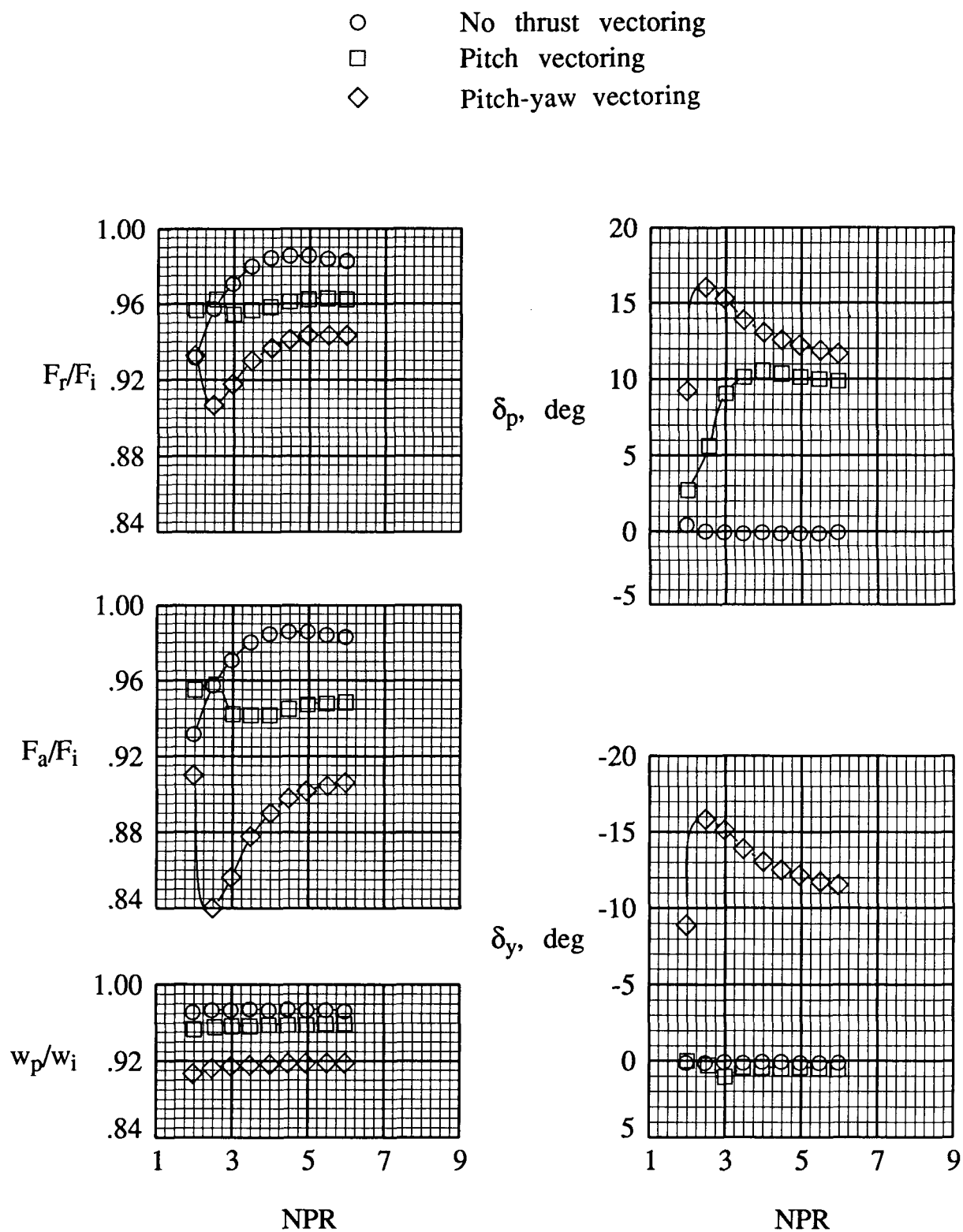
Figure 10. Continued.

- No thrust vectoring
- Pitch vectoring
- ◇ Pitch-yaw vectoring



(c) Shifted-throat configuration.

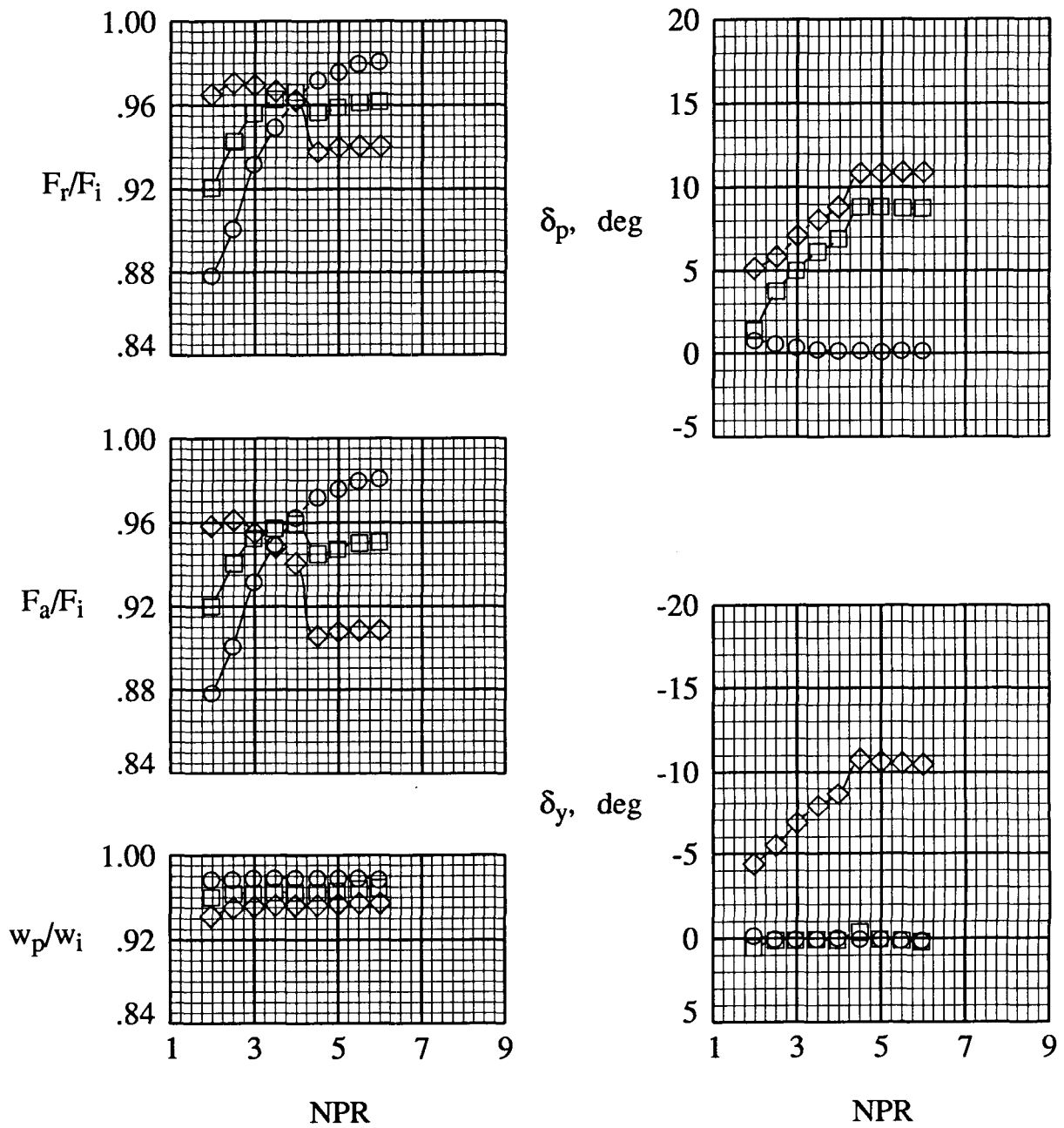
Figure 10. Concluded.



(a) Narrow flaps; $A_e/A_t = 1.2$.

Figure 11. Performance of afterburning power cruciform nozzle.

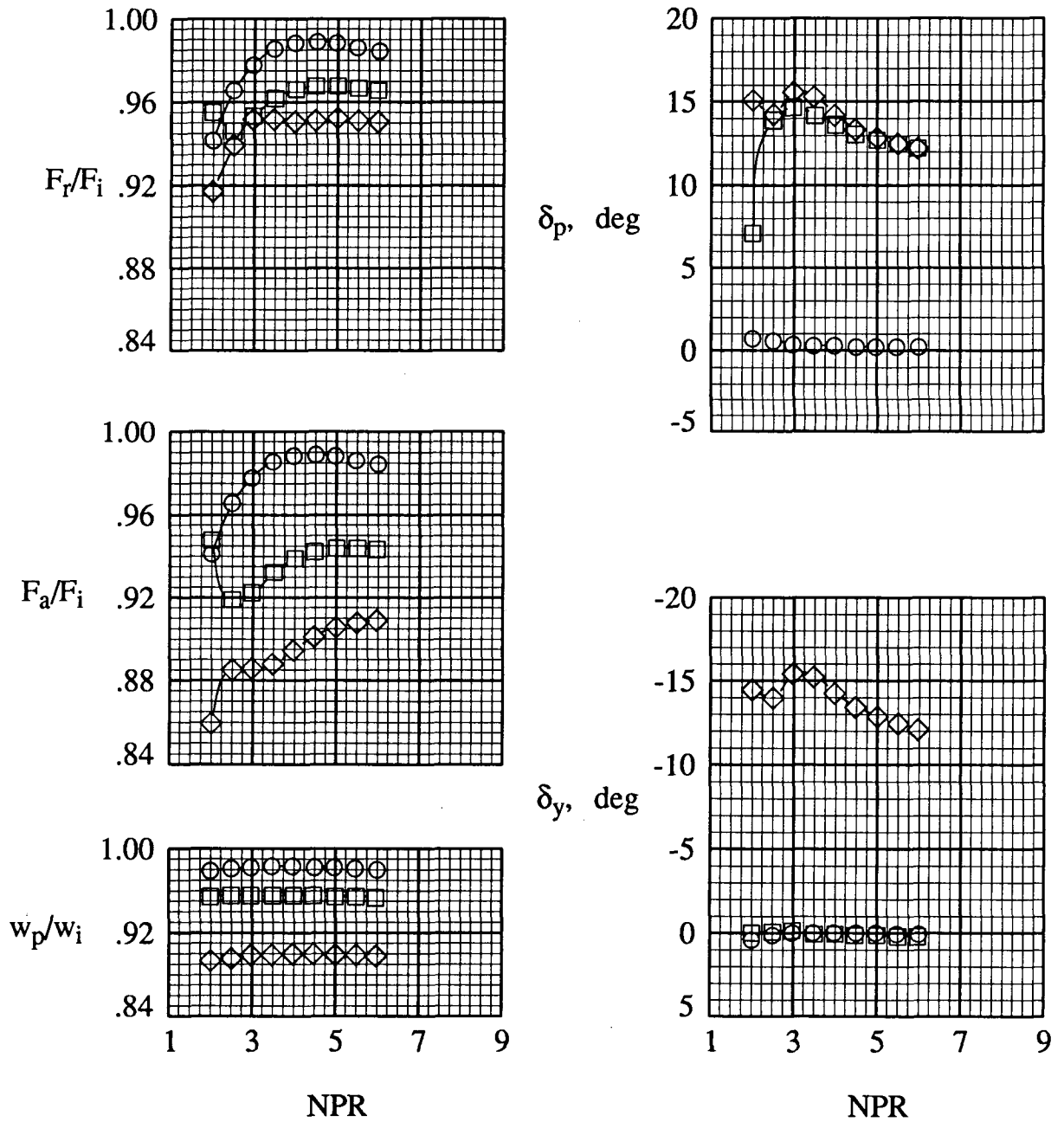
- No thrust vectoring
- Pitch vectoring
- ◇ Pitch-yaw vectoring



(b) Narrow flaps; $A_e/A_t = 1.4$.

Figure 11. Continued.

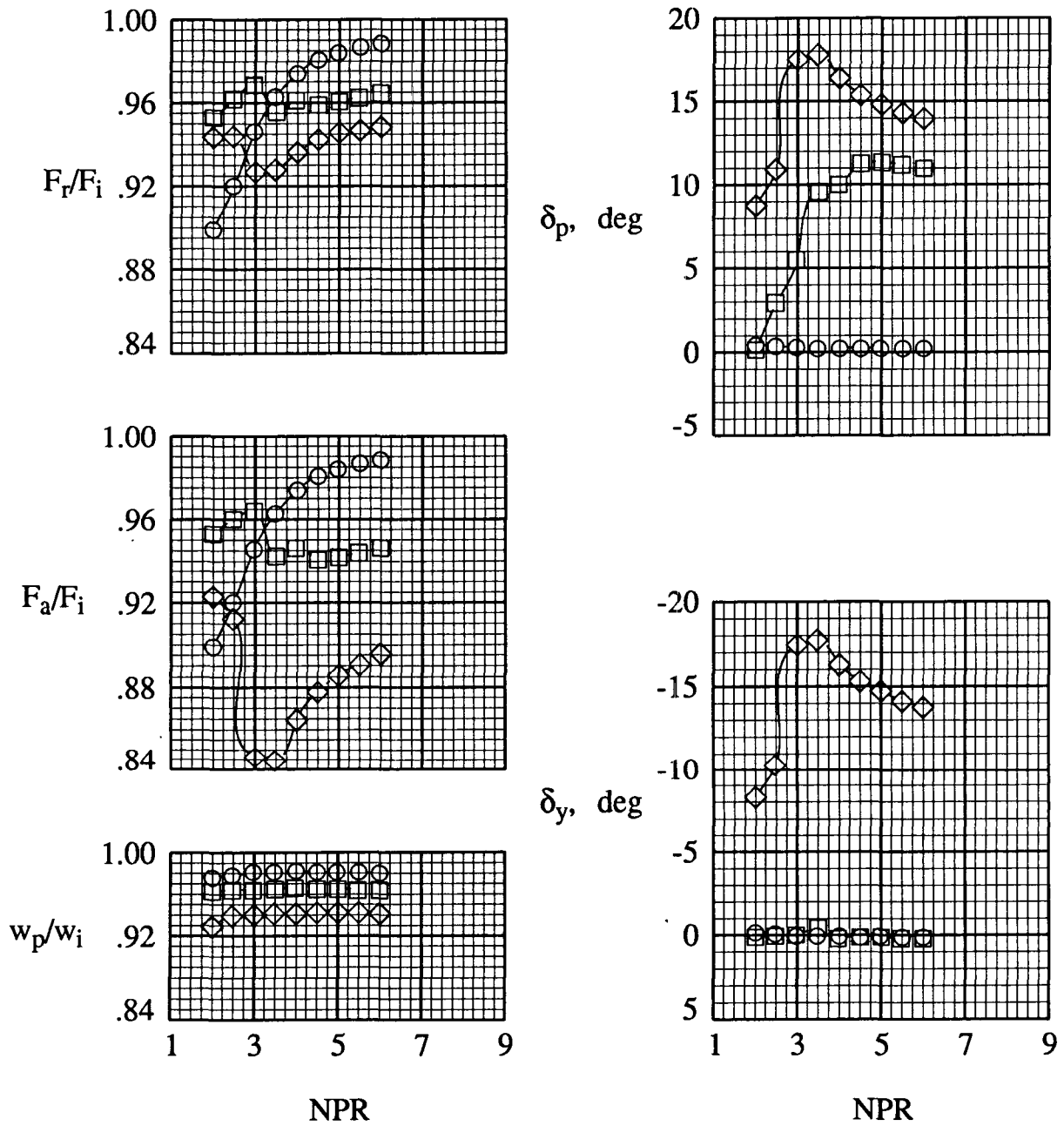
- No thrust vectoring
- Pitch vectoring
- ◇ Pitch-yaw vectoring



(c) Wide flaps; $A_e/A_t = 1.2$.

Figure 11. Continued.

- No thrust vectoring
- Pitch vectoring
- ◇ Pitch-yaw vectoring



(d) Wide flaps; $A_e/A_t = 1.4$.

Figure 11. Concluded.

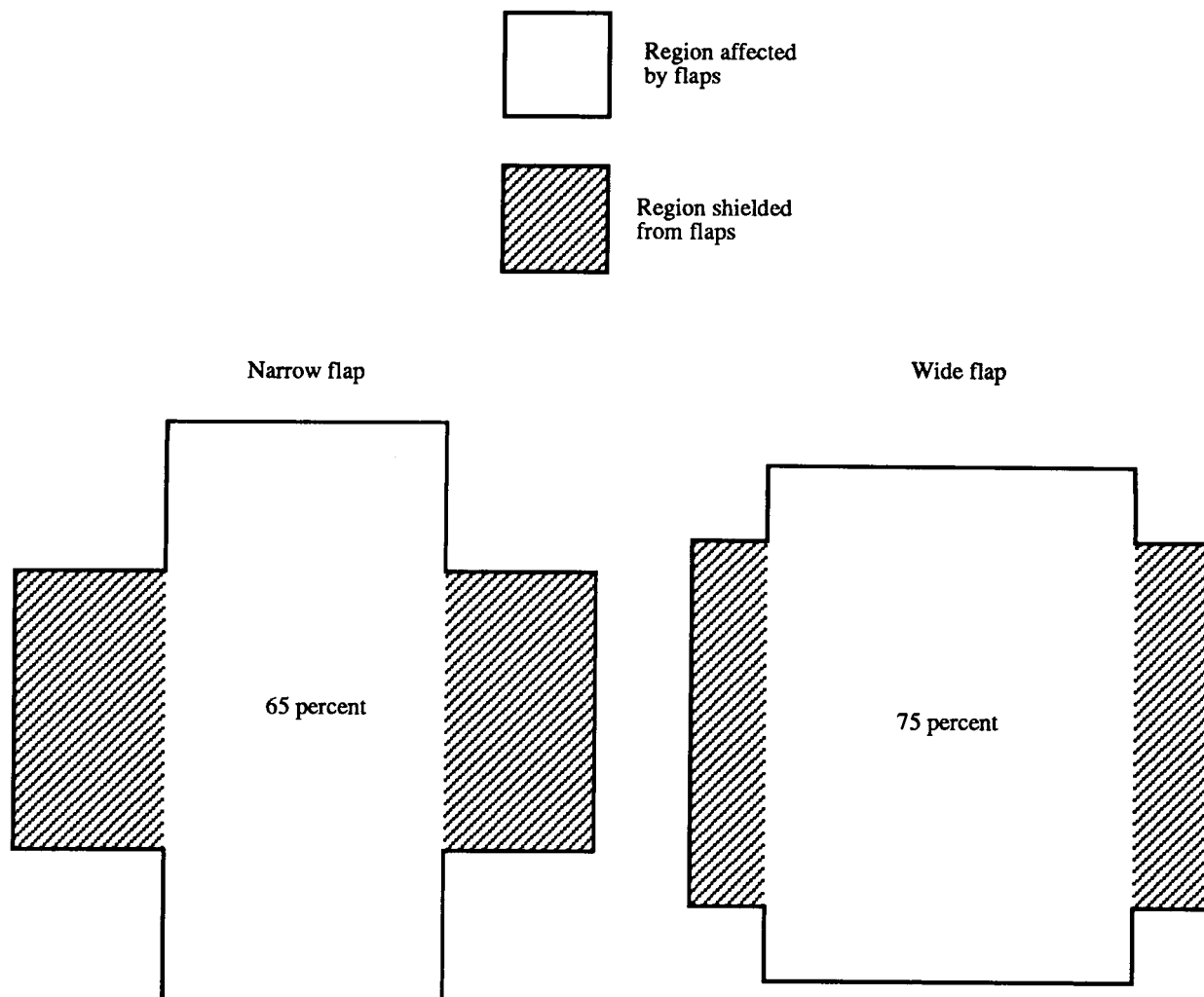


Figure 12. Percentage of flow area affected by pitch flaps of dry power cruciform nozzles.

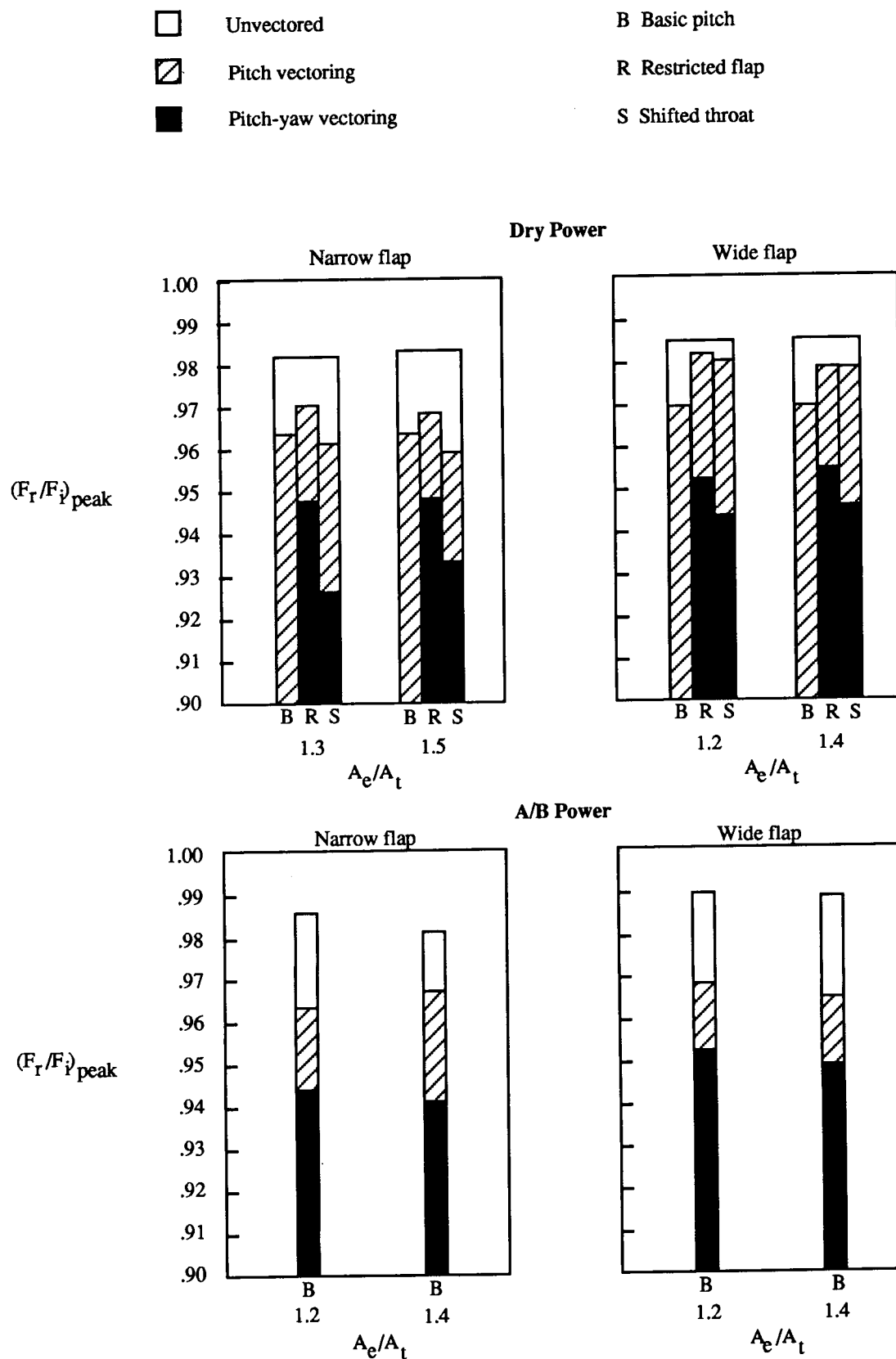


Figure 13. Peak resultant thrust ratios of cruciform nozzle configurations.

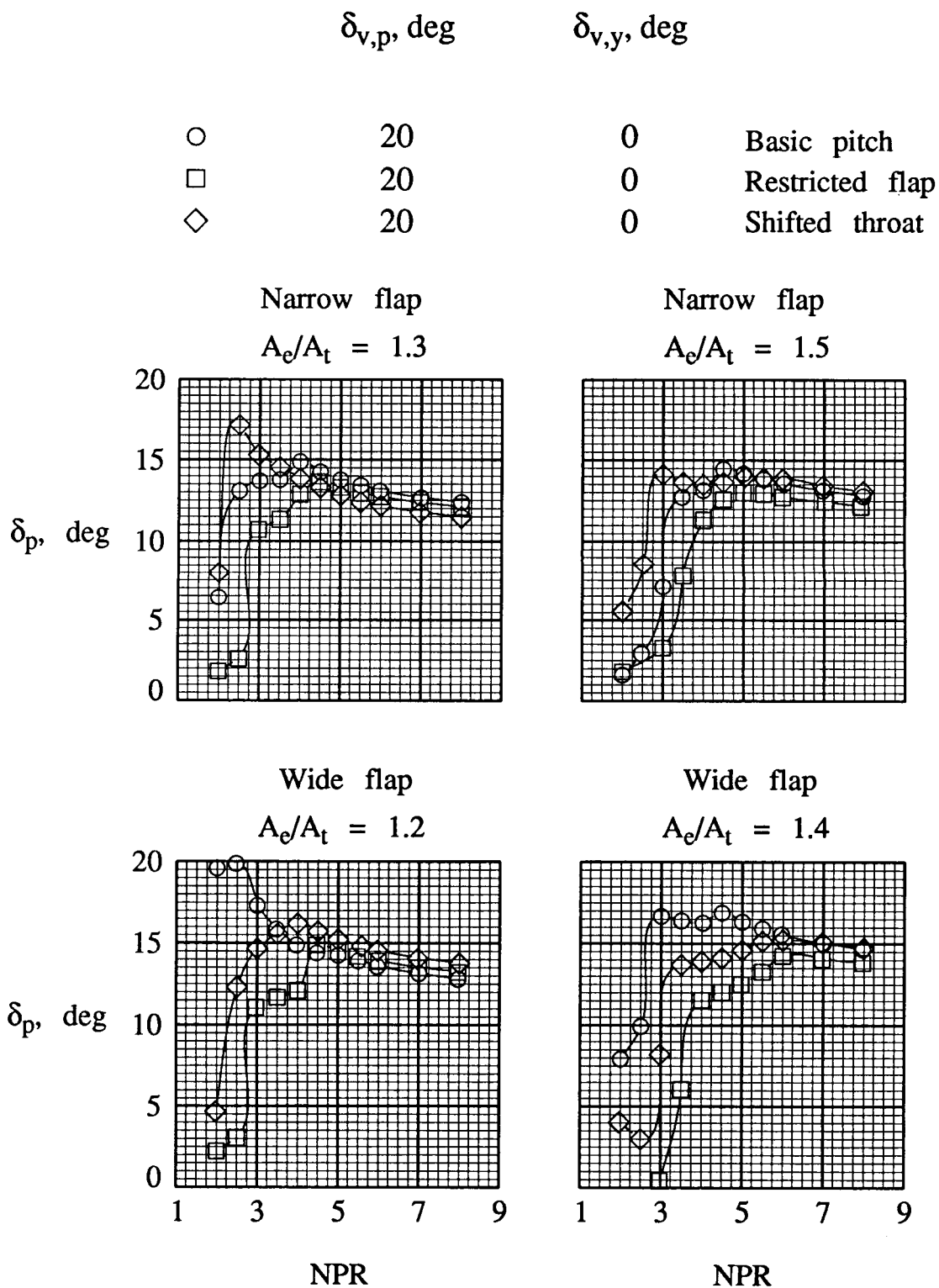
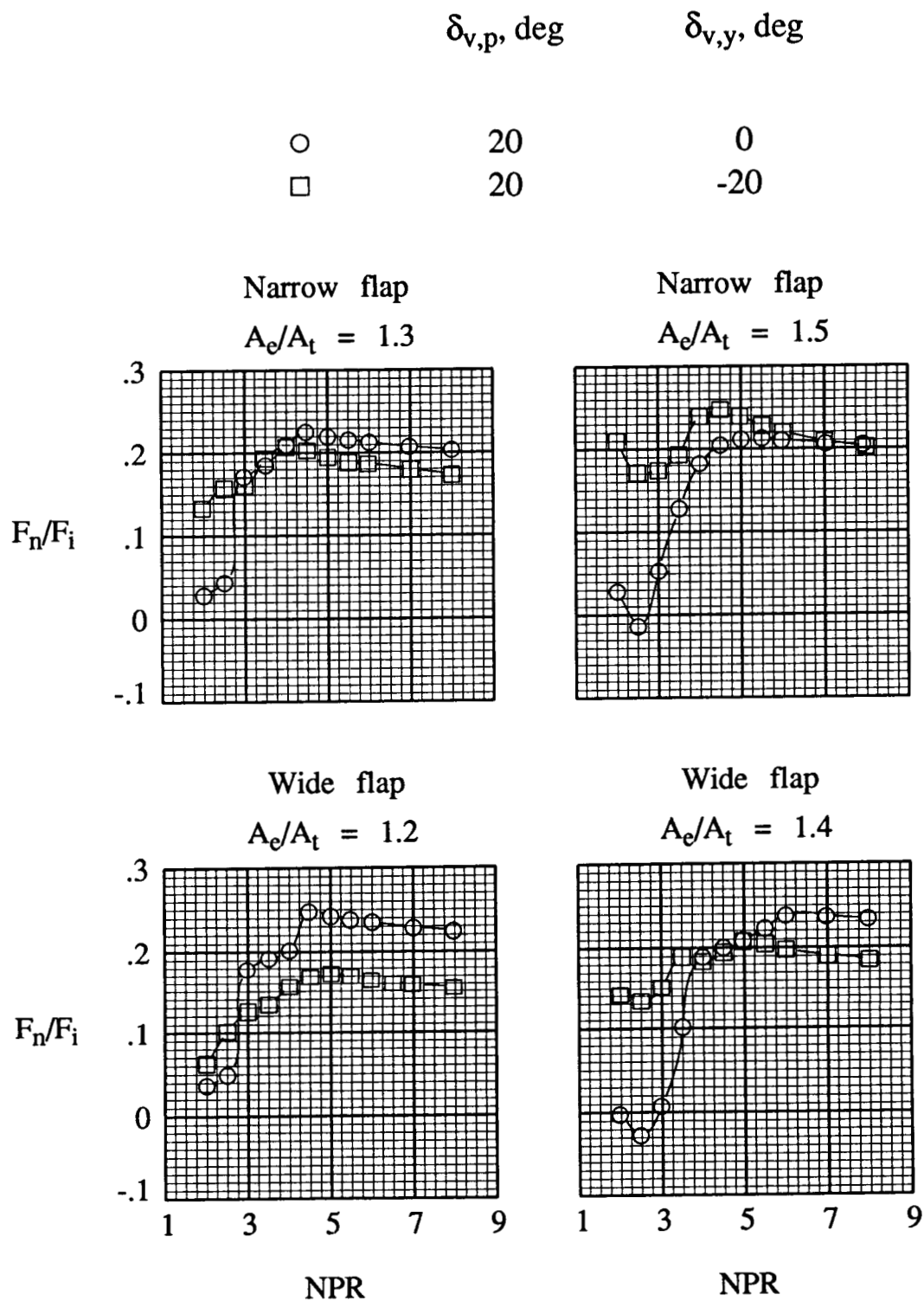
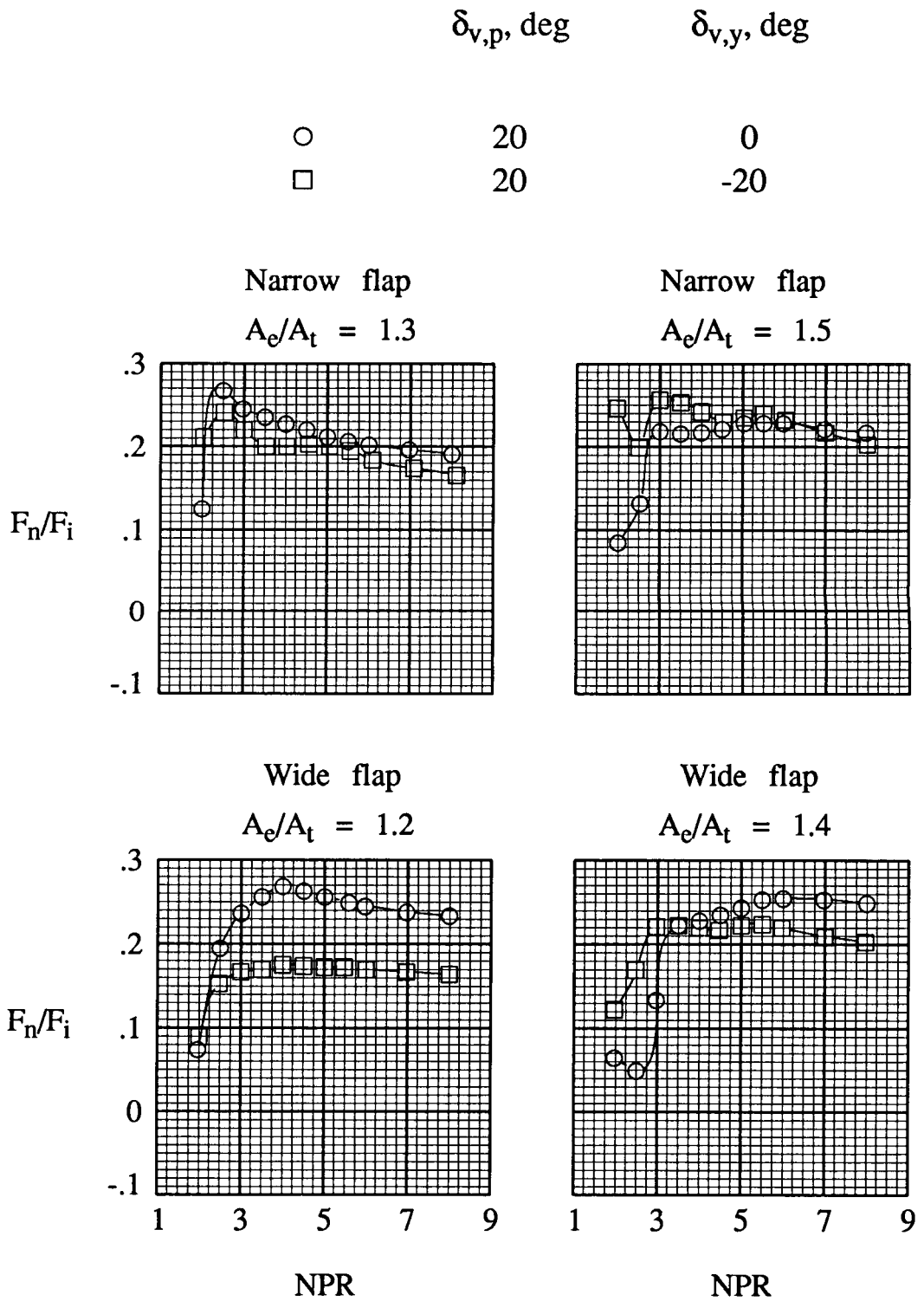


Figure 14. Pitch-vectoring capability of cruciform nozzle configurations.



(a) Restricted flap.

Figure 15. Effect of yaw vectoring on normal-force ratio for dry power setting.



(b) Shifted throat.

Figure 15. Concluded.

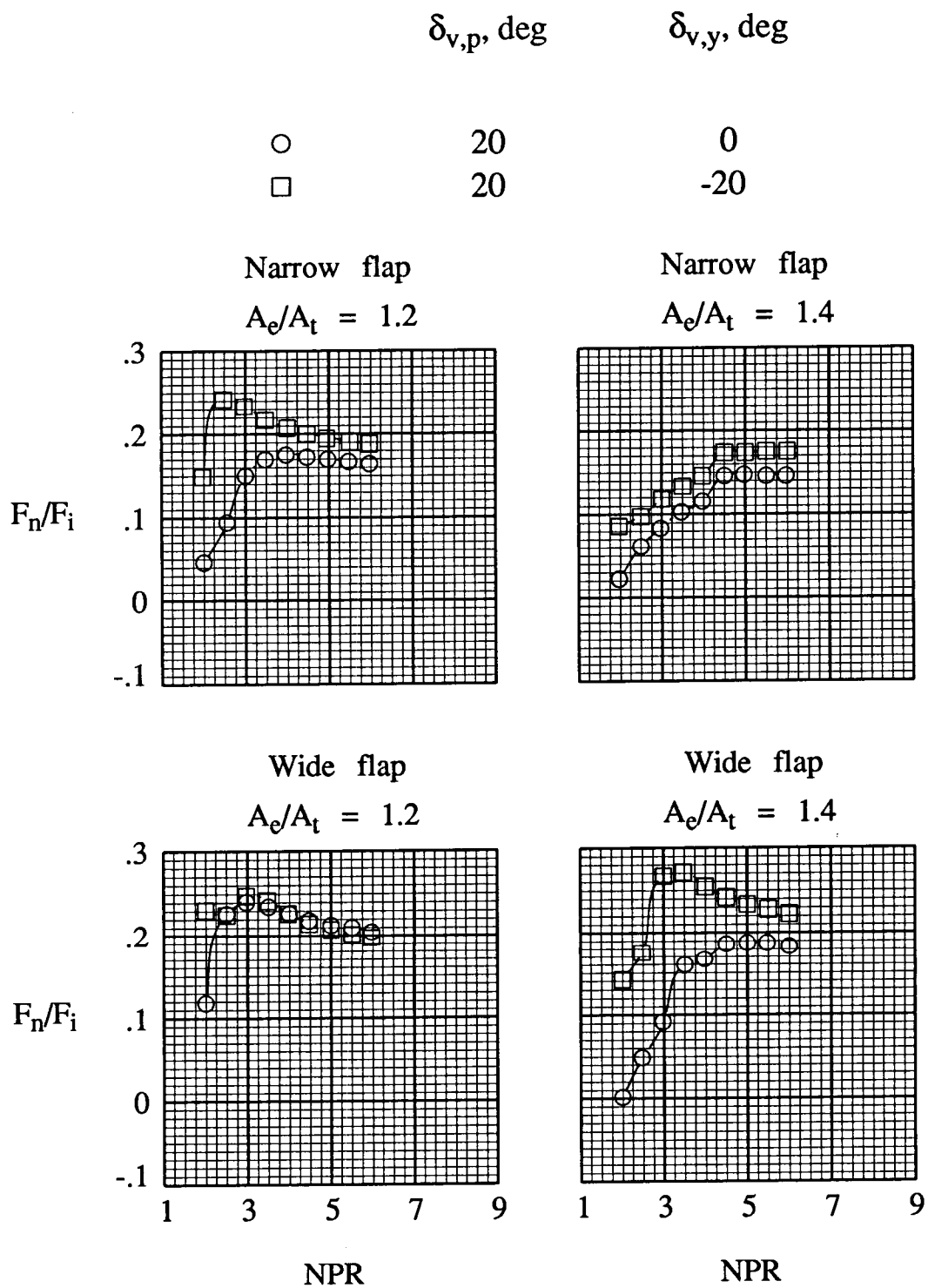


Figure 16. Effect of yaw vectoring on normal-force ratio for afterburning power setting.

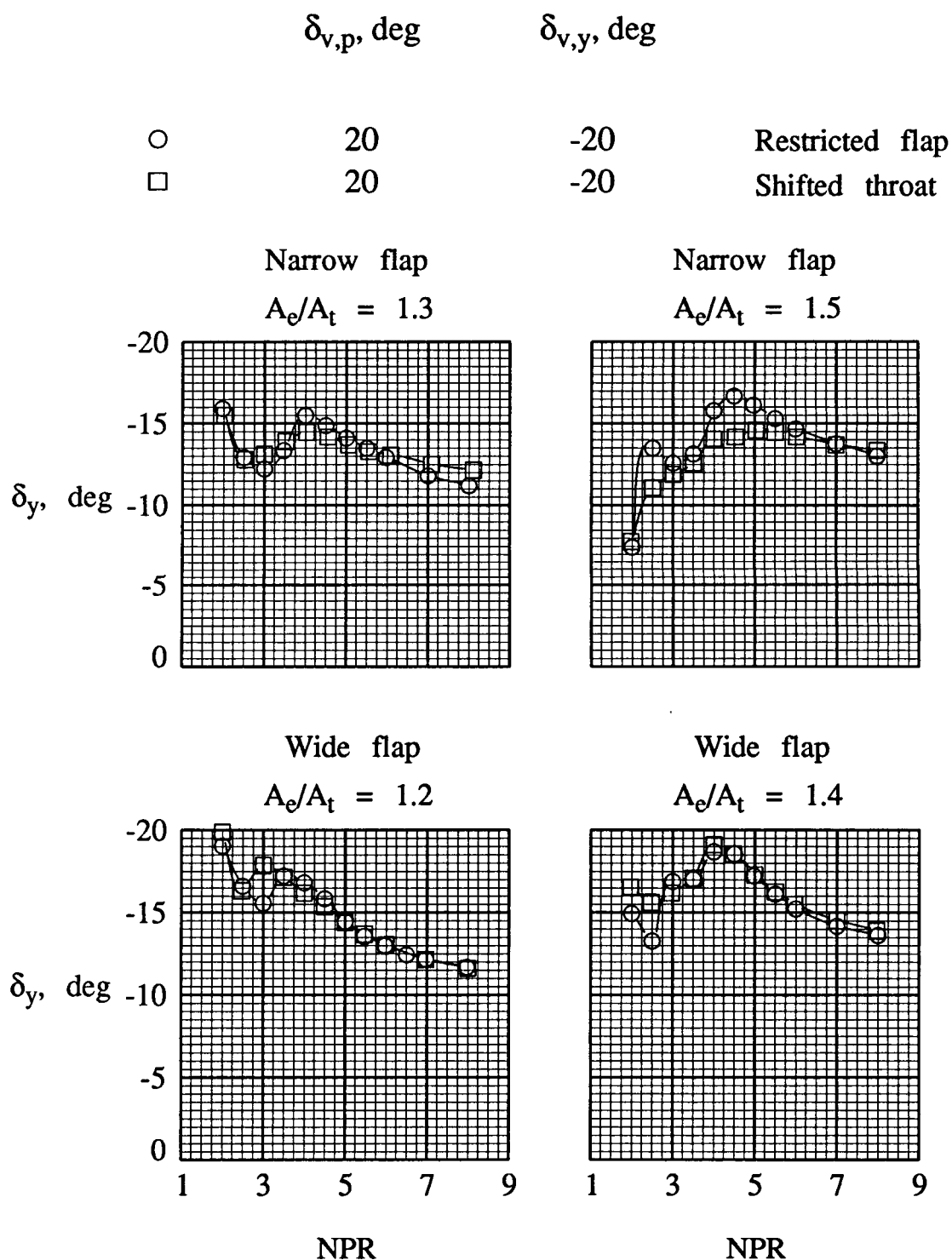
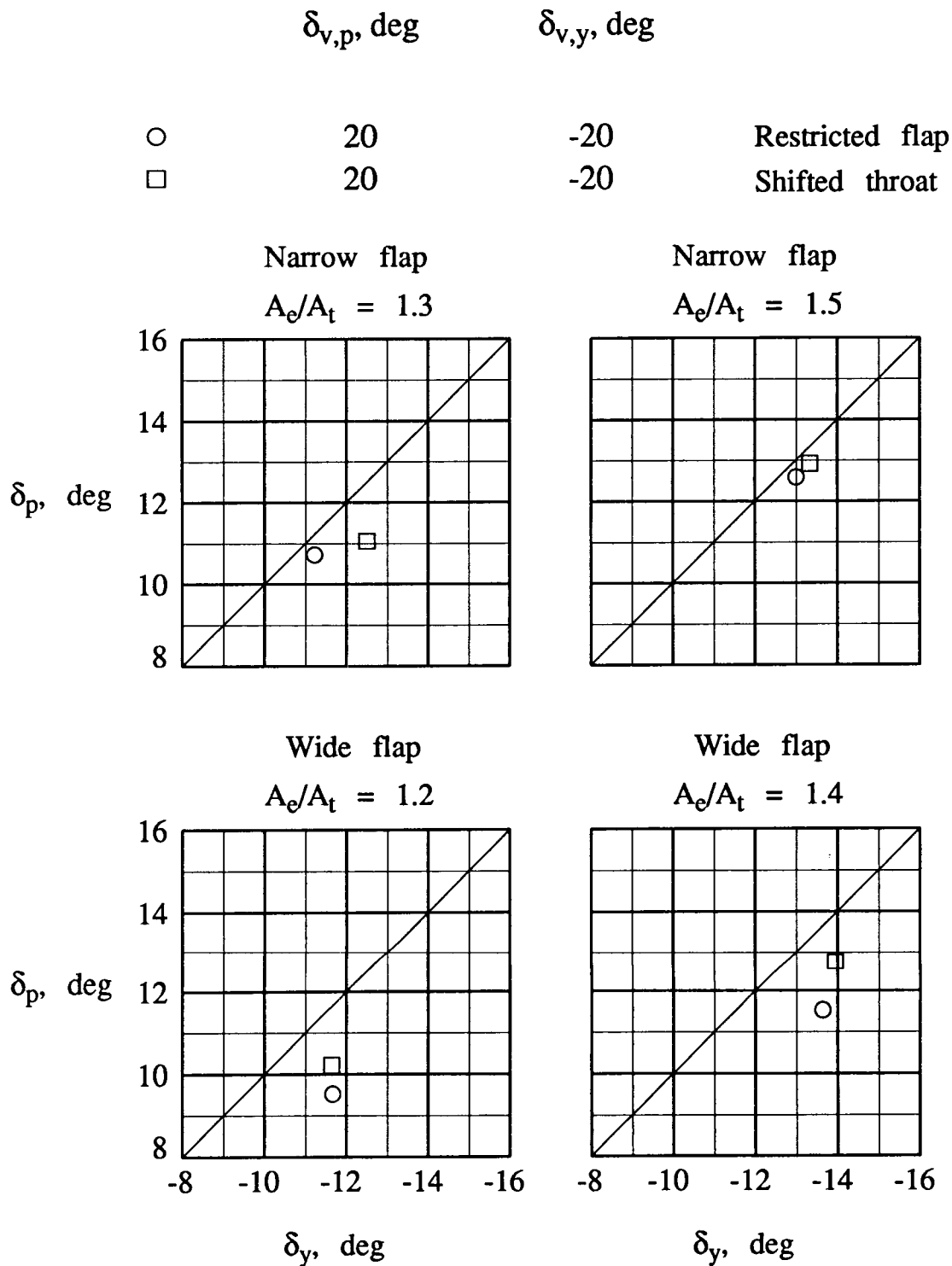


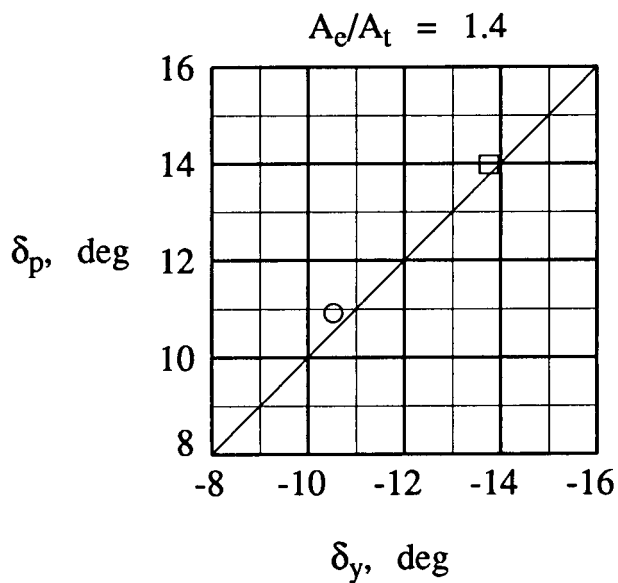
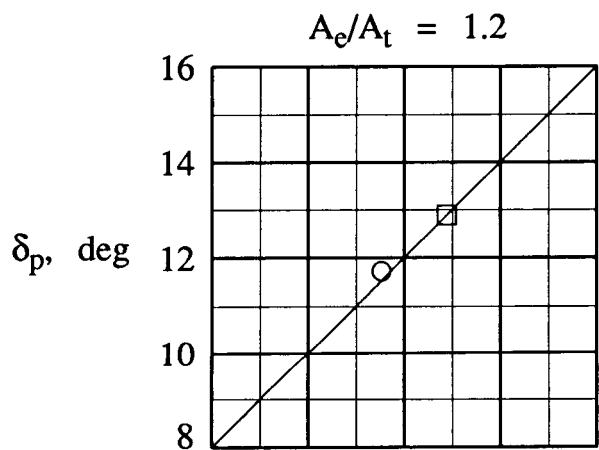
Figure 17. Yaw thrust-vectoring capability of multiaxis-thrust vectoring cruciform nozzle with dry power setting.



(a) Dry power setting.

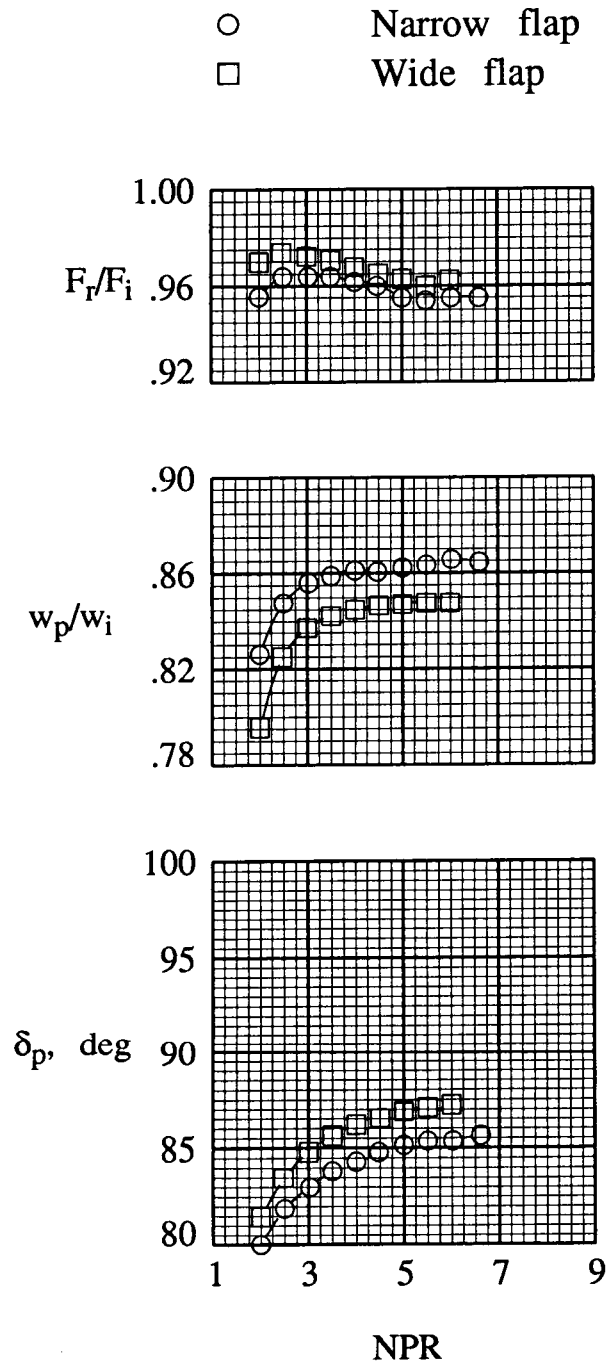
Figure 18. Multiaxis thrust-vector angles at peak resultant thrust ratio. Solid line represents equal pitch and yaw thrust-vector angles.

	$\delta_{v,p}$, deg	$\delta_{v,y}$, deg	
○	20	-20	Narrow flap
□	20	-20	Wide flap



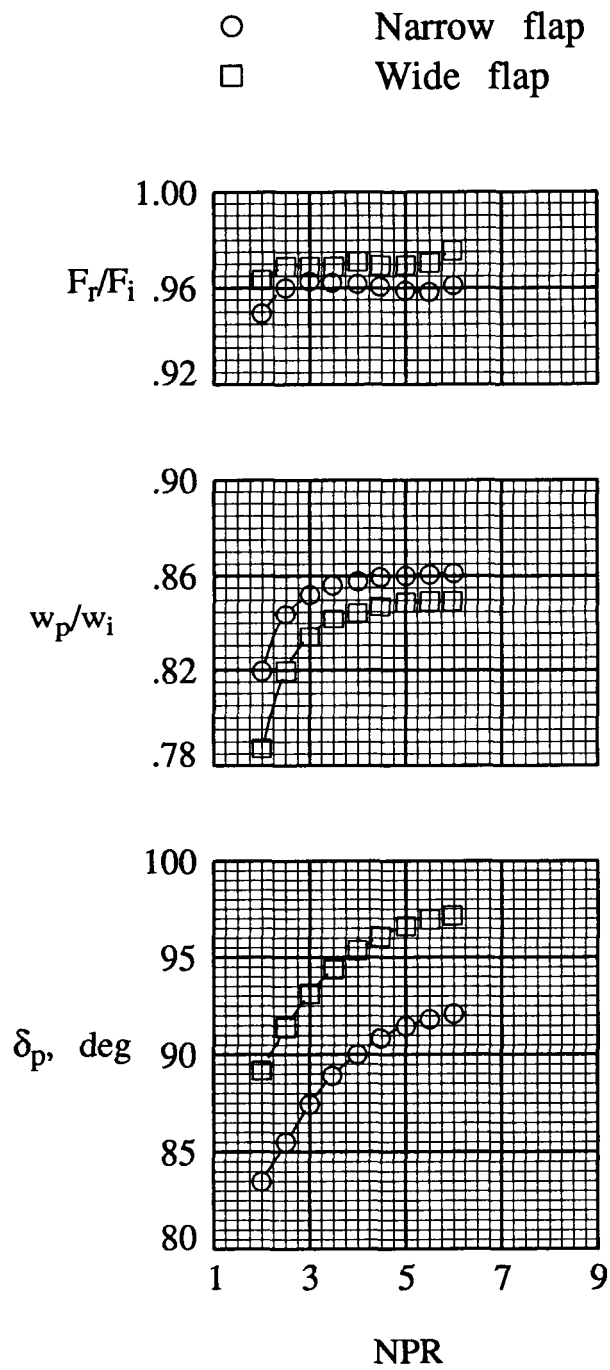
(b) Afterburning power setting.

Figure 18. Concluded.



(a) No port length extension.

Figure 19. Performance of vertical-thrust nozzles with narrow and wide flaps.



(b) Port length extension installed.

Figure 19. Concluded.

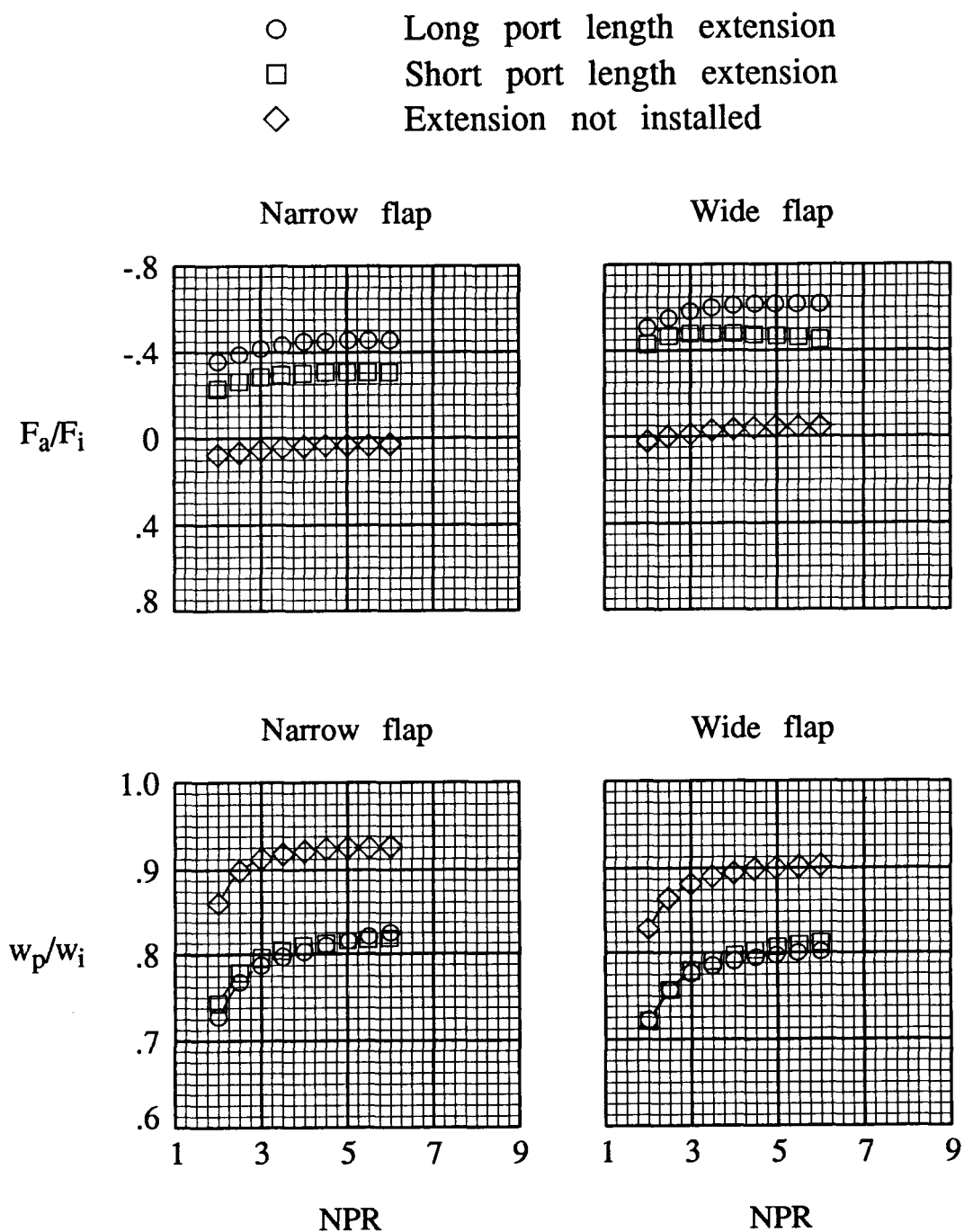


Figure 20. Axial thrust ratios and discharge coefficients of thrust reversers with varying port lengths.

REPORT DOCUMENTATION PAGE			Form Approved OMB No. 0704-0188	
Public reporting burden for this collection of information is estimated to average 1 hour per response, including the time for reviewing instructions, searching existing data sources, gathering and maintaining the data needed, and completing and reviewing the collection of information. Send comments regarding this burden estimate or any other aspect of this collection of information, including suggestions for reducing this burden, to Washington Headquarters Services, Directorate for Information Operations and Reports, 1215 Jefferson Davis Highway, Suite 1204, Arlington, VA 22202-4302, and to the Office of Management and Budget, Paperwork Reduction Project (0704-0188), Washington, DC 20503.				
1. AGENCY USE ONLY (Leave blank)	2. REPORT DATE April 1992	3. REPORT TYPE AND DATES COVERED Technical Paper		
4. TITLE AND SUBTITLE Static Performance of a Cruciform Nozzle With Multiaxis Thrust-Vectoring and Reverse-Thrust Capabilities		5. FUNDING NUMBERS WU 505-62-30-01		
6. AUTHOR(S) David J. Wing and Scott C. Asbury				
7. PERFORMING ORGANIZATION NAME(S) AND ADDRESS(ES) NASA Langley Research Center Hampton, VA 23665-5225		8. PERFORMING ORGANIZATION REPORT NUMBER L-16958		
9. SPONSORING/MONITORING AGENCY NAME(S) AND ADDRESS(ES) National Aeronautics and Space Administration Washington, DC 20546-0001		10. SPONSORING/MONITORING AGENCY REPORT NUMBER NASA TP-3188		
11. SUPPLEMENTARY NOTES				
12a. DISTRIBUTION/AVAILABILITY STATEMENT Unclassified Subject Category 02		12b. DISTRIBUTION CODE		
13. ABSTRACT (Maximum 200 words) A multiaxis thrust-vectoring nozzle designed to have equal flow-turning capability in pitch and yaw was conceived and experimentally tested for internal, static performance. The cruciform-shaped convergent-divergent nozzle turned the flow for thrust vectoring by deflecting the divergent surfaces of the nozzle, called flaps. Methods for eliminating physical interference between pitch and yaw flaps at the larger multiaxis deflection angles were studied. These methods included restricting the pitch flaps from the path of the yaw flaps and shifting the flow path at the throat off the nozzle centerline to permit larger pitch-flap deflections without interfering with the operation of the yaw flaps. Two flap widths were tested at both dry and afterburning power settings. Vertical- and reverse-thrust configurations at dry power were also tested. Comparison with two-dimensional convergent-divergent nozzles showed lower but still competitive thrust performance and thrust-vectoring capability.				
14. SUBJECT TERMS Multiaxis thrust vectoring; Multifunction nozzles; Thrust vectoring; Nozzles; Reverse-thrust capabilities			15. NUMBER OF PAGES 80	
			16. PRICE CODE A05	
17. SECURITY CLASSIFICATION OF REPORT Unclassified	18. SECURITY CLASSIFICATION OF THIS PAGE Unclassified	19. SECURITY CLASSIFICATION OF ABSTRACT	20. LIMITATION OF ABSTRACT	